New Insights into Light Scattering

by

Aaron Stephen Rury

A dissertation submitted in partial fulfillment
of the requirements for the degree of
Doctor of Philosophy
(Applied Physics)
in The University of Michigan
2012

Doctoral Committee:

Professor Roseanne J. Sension, Chair
Professor Paul R. Berman
Professor Roberto D. Merlin
Professor Stephen C. Rand
Professor Duncan G. Steel

To J.C. Maxwell, C.V. Raman and L.M. Duquette-Rury without whose inspiration this work would not have been possible.

Acknowledgements

I would like to thank the many people who have contributed to my reaching this point in my academic career, although in different ways. First, my parents consistently encouraged me to follow a career in physical science. They supported my undergraduate education with no questions asked and provided me both financial and emotional support as I made my complicated transition to graduate school.

Second, I would like to thank the University of Michigan community of scholars generally. Over many decades of intense study they have set a standard of excellence that I have used to challenge myself again and again to think bigger, be smarter and achieve more day in and day out. I know that this environment has helped me immensely to put forth my best work possible.

Third, I would like to think the Applied Physics Program. While I was not directly admitted into the program as I came to Michigan, they welcomed me with open arms and assisted me through each step of my graduate experience. The support of both Cyndi McNabb and Charles Sutton have helped me fulfill my potential as a scholar, a mentor and a communicator in the context of our wonderful graduate program.

Fourth, I would like to Prof. Duncan Steel. Duncan helped me recognize the research avenues I wanted to pursue during my time at Michigan as well as helped with my entry into the Applied Physics. Duncan has also provided me what I needed to fulfill my potential as a researcher whether that was a push to work harder or validation of the directions in which I was pushing. His time and support were, and still are, invaluable to me as both a person and a professional.

Fifth, I would like to thank Dr. Richard Freeling. When others either could not or would not indulge my whacky ideas concerning the possible interactions of light and matter, Rich could and would. Much of the work in this dissertation would not have been possible without his reassurance and insight. Without his support I might not have recognized an entire field of research to which my passions are drawn.

Sixth, I would like to thank my current and former labmates. I would especially like to thank Prof. Ken Spears and Dr. Jian Peng who assisted my learning in many ways from laser operation and theory to practical optics to numerical analysis. I would also like to thank Vasudev Lal who allowed me to learn with him how to work in an optics and laser lab and with whom I had many stimulating conversations on the nature of light-matter interactions. Also, I would like to thank Dr. Andrew Stickrath, Dr. Michael Orozco, Dr. Anna Sharikova, Broc Smith, Brenden Arruda, Edwin Najera, and Chris Anderson for indulging my tastes in so many group meetings.

Seventh, I would like to thank my advisor, Prof. Roseanne Sension. I can only imagine that most Ph.D. advisors do not easily let their students ‘travel’ through the cornucopia of research topics I engage in this work. Roseanne not only allowed me to pursue research questions I developed, she encouraged me to do so. Having been able to do so I now realize what a luxury I have been offered in my graduate career. Few students find the support necessary to both develop theory and try to test it in the lab on topics far afield from what their group has done in the past. I consider myself very lucky to have been able to have the opportunity to do just that.

Finally, I would like to thank my wife, Lauren. When I met my wife my life had little to do with physics, optics or lasers. In fact, I was a professional dog walker. Through our relationship Lauren has helped me recognize my passion for physical inquiry. She has helped me find confidence necessary to believe that I can make significant contributions to our knowledge of the physical world. She supported me through the ups and downs of research endeavors and pushed me harder than anyone else to fulfill my potential both as a person and a professional. She is a constant inspiration without whom none of the work I present below would have been possible. She is the definition of a partner.

There are also many others who have helped me reach this point. They include classmates, instructors, colleagues and family. No one achieves in this world alone and I am happy to recognize the aid of others in my achieving the goals I have set for myself so far. Thank you.

Table of Contents

List of Figures

List of Tables

Chapter 1:
Introduction To New Insights into Light Scattering

Introduction

Light scattering has long played an important role in characterizing and identifying matter ranging from molecular Bose-Einstein condensates[1] to geological samples on other planets.[2, 3] Since light scattering is inherently a two-photon process, it provides the researcher with important information about the structure and dynamics of matter not accessible from single photon interactions such as the absorption of light. Perhaps more interestingly, light scattering from quantum mechanical matter highlights the wave-like character of molecules via the interference between different pathways to final states.[4]

Interest in the interaction of Laguerre-Gauss beams with matter has grown largely due to their possession of a well-defined orbital angular momentum (OAM) within the paraxial approximation.[5, 6] Since the conservation of the angular momentum dominates many light-matter interactions, researchers predict that OAM amends rules governing allowed transitions and behavior within these interactions.[7-9] However, there remain gaps in the literature. Researchers have yet to fully examine the scattering of beams carrying OAM.

The scattering of beams carrying OAM may provide new insights in the structure and dynamics of important materials constructed from atoms and molecules. OAM may also allow researchers new levels of control over the behavior of matter in different limits via light-matter interactions. This dissertation attempts to help fill this gap by examining the scattering of LG beams from both classical and quantum mechanical matter.

Laguerre-Gauss Beams and the Orbital Angular Momentum of Light

In the paraxial approximation, the diffractive effects associated with the propagation of a light beam are ignored. Ignoring these diffractive effects allows one to calculate the transverse electromagnetic (EM) modes of an optical resonator, such as a laser oscillator, as solution to the paraxial Helmholtz equation. For a beam propagating in the z-direction, the paraxial Helmholtz equation becomes,[10]

$$\nabla_t^2 u(\vec{r}) + 2ik\frac{\partial^2}{\partial z^2}u(\vec{r}) = 0. \qquad (1.1)$$

where u is the EM mode amplitude, the subscript t indicates the coordinates transverse to the z-direction and k is the wavevector of the propagating beam. The transverse EM (TEM) modes of a laser depend on the coordinate geometry chosen for the calculation. In the case of cylindrical coordinates (r, φ, z) the solutions to the paraxial Helmholtz equation are,[6]

$$\begin{aligned} u(\vec{r}) = C\frac{z_R}{\sqrt{z_R^2+z^2}}\left[\frac{r\sqrt{2}}{w(z)}\right]^l L_p^l\left[\frac{2r^2}{w^2(z)}\right]\exp\left(\frac{-r^2}{w^2(z)}\right) \\ \times\exp\left(\frac{-ikr^2z}{2\left(z_R^2+z^2\right)}\right) \\ \times\exp(-il\varphi)\exp\left(i(2p+l+1)\tan^{-1}\frac{z}{z_R}\right). \end{aligned} \qquad (1.2)$$

where z_R and w(z) follow the same definition as for other Gaussian beams.[10] It is important to note that a Laguerre polynomial defines the transverse profile of these solutions. Due the presence of this Laguerre polynomial these solutions are called Laguerre-Gauss (LG) beams. Also, the Guoy phase of this beam scales with the radial, p, and azimuthal, l, indices of the Laguerre polynomial. The intensity profile and wavefront of a LG beam are shown in FIG. 1.1.

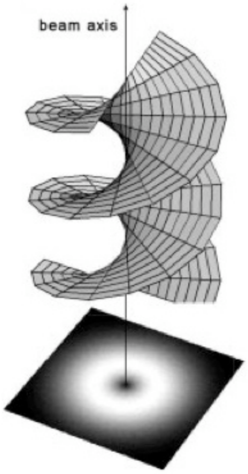

FIG 1.1 Picture of the wavefront and transverse intensity of a p=0, l=1 LG beam. The single radial node at the center of the beam indicates p=0. [11]

Most interestingly, the solutions in eqn. (2) possess an azimuthal dependence. This azimuthal dependence leads to a form of angular momentum associated with the transverse profile of the beam. In comparison to the solutions of the Schrodinger equation for the hydrogen atom, which also contain a similar dependence on the φ-coordinate, this form of angular momentum is given the name 'orbital'. In Chapter 7 the connection between this azimuthal coordinate dependence and the angular momentum density of the beam is shown explicitly using the expansion over the vector spherical harmonics.

The Classical and Quantum Mechanical Scattering of Light Beams Carrying OAM

Broadly, this dissertation is broken into sections that investigate the scattering of light beams carrying OAM in two different limits. The first, larger section of the dissertation treats the quantum mechanical effects associated with vibrational resonance Raman scattering of LG beams from molecules. The second, smaller section treats the classical scattering of beams carrying OAM from sub-micron metallic particles. In each limit I predict OAM will allow researchers new avenues to control matter via its interactions with light.

To calculate the selection rules for resonance Raman scattering of LG beams from molecules, I use the interaction Hamiltonian developed by Alexandrescu et al.[7] Alexandrescu et al. predict changes in the light-matter interactions of the simplest of all molecules, the H_2^+ ion, when this system is placed at the center of the incident LG beam.

I extend their interaction Hamiltonian to the case of a complex molecule placed anywhere within the profile of the LG beam. I show that molecules placed throughout the profile of the beam exhibit the same changes to rules governing allowed vibrational transitions occurring during an electronic dipole transition, otherwise known as vibronic selection rules.[12] These changes occur due to a coupling between the transverse radial variation of the incident field and the quantized vibrations of the molecule. The implications of electromagnetically mediated vibronic coupling are then discussed in the context of the adiabatic approximation and molecular light absorption.[12]

I then use the extended interaction Hamiltonian to calculate an differential LG-scattering cross-section. With this cross-section I predict how an incident LG beam changes the resonance Raman scattering from the totally symmetric vibrations of both simple diatomic and complex polyatomic molecules. I show that there are changes in behavior of both vibrational populations and coherences due to the EM-mediated vibronic coupling between the transverse radial variation of the incident LG and the molecule's quantized vibrations.

For vibrational populations, the incident LG provides easier access to the excitation of overtone states of totally symmetric vibrations for molecules possessing an electronic excited state minimally displayed from the geometry of the ground electronic, as is the case for many complex polyatomic molecules. In the case of small diatomic homonuclear molecules whose excited electronic states are largely displayed relative to the ground state, I show that the intensity distribution over the excited overtone states of the only totally symmetric vibration changes in response to the incident LG beam. However, the exact changes in this distribution are hard to predict in the case of a general diatomic system.

I also show the EM-mediated vibronic coupling introduces additional pathways to the Raman scattering process. These additional quantum mechanical pathways result in interference effects that modulate the intensity of peaks in the resonance Raman spectrum of a molecule. For a molecule possessing a minimally displaced excited electronic state, I show that the sign and magnitude of these interference effects depend on the size of the spot of the LG beam, the detuning of the incident laser frequency from an electronic transition and magnitude of the vibrational frequency of interest. This information allows a researcher to tailor the relative intensity of the peaks of different totally symmetric vibrations observed in a resonance Raman spectrum, as well as excite transitions not normally observed in such spectra.

Before discussing experimental tests of the predictions from the EM-mediated vibronic coupling model using resonance Raman scattering from condensed phase diatomic iodine (I_2) and iron(III) tetraphenylporphyrin chloride [$Fe^{(III)}$TPPCl], I examine the ultrafast dynamics and photochemistry of $Fe^{(III)}$TPPCl. This examination allows one to most appropriately test the predictions of the EM-mediated vibronic coupling model in light scattering. Since $Fe^{(III)}$TPPCl shares a similar structure and optical properties with several protein bound iron-centered porphyrins, researchers have not thoroughly investigated its ultrafast dynamics with the most modern techniques available.[13-16]

Our investigation using ultrafast, broadband transient absorption (TA) spectroscopy shows that while $Fe^{(III)}$TPPCl shares some structural properties with heme proteins, its excited state dynamics contrast starkly. While all protein bound iron porphyrins internally convert to their electronic ground within 1 ps of excitation, non-radiative relaxation through a sequence of the excited electronic states dominates the ultrafast dynamics of $Fe^{(III)}$TPPCl. We reach this conclusion by examining two attributes of TA measurements: 1) the time dynamics of a zero-crossing (isosbestic point) of the measured difference spectra and 2) a 3 order of magnitude elongation of the lifetime of the longest-lived state at sub-100 K temperatures. Neither of these observations is consistent with sub-ps internal conversion to the electronic ground state of the molecule.[13-15]

At sub-100 K temperatures and in the presence of toluene, $Fe^{(III)}$TPPCl also displays photochemistry dependent on the frequency and intensity of incident laser light. Investigation of this photochemistry allows one to more clearly delineate between the behavior induced by an LG beam versus that caused by the solvent environment. Using resonance Raman scattering from $Fe^{(III)}$TPPCl dissolved in a glass formed by a 1:1 mixture of toluene and dichloromethane (CH_2Cl_2) at 77 K we show that this molecule undergoes a chemical reaction when the intensity of 413 nm laser light passes a threshold. This reaction produces states in which at least one toluene molecule is bond to the central iron atom. Also, a product species appears featuring an iron atom in its low-spin state. This state is populated via a spin transition from the initially excited high-spin form of the same molecule. I discuss the use of this photochemical process in opto-magnetic technologies.

This thorough examination of the electronic dynamics and vibrational behavior of condensed phase $Fe^{(III)}$TPPCl allow meaningful tests of the EM-vibronic coupling model with resonance Raman scattering. Upon testing the predictions of the model with the totally symmetric vibrations I_2 and $Fe^{(III)}$TPPCl, we find no systematic difference between the resonance Raman spectra measured with TEM_{00} excitation versus that excited with a LG beam. I discuss the effective ceiling these results provide on the effects predicted from the EM-mediated vibronic coupling model as well as possible errors in the derivation. I also discuss further measurements that may more completely test the predictions of the model specifically including stimulated Raman scattering processes.

Finally, I investigate the use of beams carrying OAM in classical electromagnetic scattering. This investigation starts by calculating the scattering of circularly polarized LG beams from spherical particles in an arbitrary size limit. I show that the angular momentum density of the incident fields is conserved in both the scattered and internal fields. In the limit that particle is much smaller than the incident wavelength, I show that the intensity of the scattered fields is very small. The intensity of the scattered fields in this limit is dramatically reduced relative to plane wave illumination for two reasons.

First, in the limit of a small particle the dipole of the particle dominates EM interactions and higher order multipole contributions to these interactions are strongly attenuated.[17, 18] Given that the angular momentum density of the incident field is conserved by the scattered fields, an incident LG beam whose angular momentum density is more than 1 unit per unit of vacuum field excitation will not excite the dipole of the particle. The conservation of angular momentum necessitates that the LG beam scatter from the higher order multipole moments of the particle, whose contribution to the interaction is very small. Therefore, the scattering of the LG beam from the particle in this size limit is vanishingly small.

Second, both the scattered fields and the fields internal to the illuminated particle are coherently excited in the incident beam.[19] In the case of the LG beam, I show that the conservation of angular momentum necessitates the excitation of higher order volume modes of the spherical particle. These higher order volume modes confine more of the excited field to the interface of the particle and its surrounding material. This confinement may be useful in some molecular characterization techniques.[19-22] The spatial profile of these higher order volume modes also matches that of the transverse radial profile of the incident LG beam. This mode matching between these fields coherent excites the higher order moments of the scattered field. However, the attenuation of these higher order moments in the small particle limit further diminish the intensity of the scattered fields. Both of these processes provide a mechanism to induce transparency in matter through the modulation of the angular momentum density of a light beam. This angular momentum-induced transparency could be useful in the development of metamaterials whose collective EM interactions are dominated by their dipole moments.[23-27]

Small metallic particles also display spectacular optical properties due to the presence of resonant localized surface electromagnetic excitations known as surface plasmon modes.[19, 28] These surface plasmon modes have allowed for the development of sub-wavelength photonic structures, devices and technologies useful in fields ranging from energy science to optical communication to molecular recognition and characterization.[20-23, 26-28] In spherical particles, these modes are resonant at frequencies associated with each of its multipole moments. Therefore, there is a connection between angular momentum and frequency-dependent scattering spectra of these particles. Using the conservation of angular momentum, I propose a model for the coherent control of plasmonic scattering spectra using the OAM of light.

To achieve coherent control, I use fractional vortex beams of light, which possess non-integer values of OAM.[29] In my model, weighted linear combinations of several LG beams possessing different azimuthal indices construct the incident fractional vortex beam. The contribution of each azimuthal index provides a different lowest order angular momentum term in the scattered field. The researcher tunes these lowest order terms with the weighting distribution. While the dipole term of plasmonic metallic particles still dominates the optical response in incoherent scattering processes, coherent scattering involves interference between angular momentum states providing a mechanism to substantially enhance contributions from the higher order multipole moments[19, 26, 30] Control over this interference via the weighting distribution in the fractional vortex beam allows for selective tailoring of several attributes of the scattering spectra. These attributes include the Fano parameter and the baseline across extensive portions of the spectrum. This selective tailoring may prove useful in molecular spectroscopy, optical modulation and interconnects as well as nonlinear optics for solar energy science.

References

1. R. Wynar, R. S. Freeland, D. J. Han, C. Ryu and D. J. Heinzen, Science **287** (5455), 1016-1019 (2000).
2. A. Wang, B. L. Jolliff and L. A. Haskin, J. Geophys. Res.-Planets **100** (E10), 21189-21199 (1995).
3. A. K. Misra, S. K. Sharma, T. E. Acosta and D. E. Bates, in *Next-Generation Spectroscopic Technologies Iv*, edited by M. A. Druy and R. A. Crocombe (2011), Vol. 8032.
4. J. Friedman and R. M. Hochstrasser, Chemical Physics Letters **32** (3), 414-419 (1975).
5. L. Allen, M. W. Beijersbergen, R. J. C. Spreeuw and J. P. Woerdman, Phys. Rev. A **45** (11), 8185-8189 (1992).
6. L. Allen, V. E. Lembessis and M. Babiker, Phys. Rev. A **53** (5), R2937-R2939 (1996).
7. A. Alexandrescu, D. Cojoc and E. Di Fabrizio, Phys. Rev. Lett. **96** (24) (2006).
8. M. Babiker, C. R. Bennett, D. L. Andrews and L. C. D. Romero, Phys. Rev. Lett. **89** (14) (2002).
9. M. van Veenendaal and I. McNulty, Phys. Rev. Lett. **98** (15) (2007).
10. A. E. Siegman, *Lasers*. (University Science Books, Mill Valley, Calif., 1986).
11. E. Santamato, Fortschritte Der Physik-Progress of Physics **52** (11-12), 1141-1153 (2004).
12. G. Fischer, *Vibronic coupling: the interaction between the electronic and nuclear motions*. (Academic Press, London ; Orlando, Fla., 1984).
13. M. Negrerie, S. Cianetti, M. H. Vos, J. L. Martin and S. G. Kruglik, J. Phys. Chem. B **110** (25), 12766-12781 (2006).
14. W. Wang, X. Ye, A. A. Demidov, F. Rosca, T. Sjodin, W. X. Cao, M. Sheeran and P. M. Champion, J. Phys. Chem. B **104** (46), 10789-10801 (2000).
15. A. Yabushita and T. Kobayashi, J. Phys. Chem. B **114** (35), 11654-11658 (2010).
16. J. C. Postlewaite, J. B. Miers and D. D. Dlott, J. Am. Chem. Soc. **111** (4), 1248-1255 (1989).
17. M. Born and E. Wolf, *Principles of optics: electromagnetic theory of*

propagation, interference, and diffraction of light. (Pergamon Press, 1959).
18. J. D. Jackson, *Classical electrodynamics*. (Wiley, New York, 1999).
19. C. F. Bohren and D. R. Huffman, *Absorption and scattering of light by small particles*. (Wiley, New York, 1983).
20. M. E. Stewart, C. R. Anderton, L. B. Thompson, J. Maria, S. K. Gray, J. A. Rogers and R. G. Nuzzo, Chemical Reviews **108** (2), 494-521 (2008).
21. C. Johannessen, P. C. White and S. Abdali, Journal of Physical Chemistry A **111** (32), 7771-7776 (2007).
22. S. Abdali, Journal of Raman Spectroscopy **37** (12), 1341-1345 (2006).
23. J. B. Pendry, D. Schurig and D. R. Smith, Science **312** (5781), 1780-1782 (2006).
24. U. Leonhardt, Science **312** (5781), 1777-1780 (2006).
25. R. Singh, C. Rockstuhl, F. Lederer and W. L. Zhang, Phys. Rev. B **79** (8) (2009).
26. B. Luk'yanchuk, N. I. Zheludev, S. A. Maier, N. J. Halas, P. Nordlander, H. Giessen and C. T. Chong, Nat. Mater. **9** (9), 707-715 (2010).
27. Y. Huang, C. J. Min and G. Veronis, Appl. Phys. Lett. **99** (14) (2011).
28. S. A. Maier, M. L. Brongersma, P. G. Kik, S. Meltzer, A. A. G. Requicha and H. A. Atwater, Advanced Materials **13** (19), 1501-+ (2001).
29. J. B. Gotte, K. O'Holleran, D. Preece, F. Flossmann, S. Franke-Arnold, S. M. Barnett and M. J. Padgett, Opt. Express **16** (2), 993-1006 (2008).
30. B. Gallinet and O. J. F. Martin, ACS Nano **5** (11), 8999-9008 (2011).

Chapter 2:
Spatially Dependent Coupling Between Molecules and Electromagnetic Fields

Introduction

Research into the interaction of Laguerre-Gauss (LG) beams with matter has spanned atomic, molecular and condensed phase systems.[1-6] This chapter will investigate one-electron interactions of a Laguerre-Gauss (LG) beam with a complex molecule using the Power-Zenau-Wooley formalism of the interaction Hamiltonian. I extend the derivation of Ref. [1] to cases in which the molecule of interest does not share a common coordinate system with the incident LG beam. It is shown that the functional form of the interaction Hamiltonian affects the absorption of light by molecules in the same manner independent of the molecule's position within the profile of the LG beam.

The main results of Ref. [1] are then re-derived in the case that the molecule and LG do not share the same coordinate systems. In this case special attention is paid to how a LG beam changes the vibrational behavior of molecules upon an electronic transition. A physical model of direct coupling between the spatial variation of the LG beam and the molecule's quantized nuclear vibration is proposed. This direct coupling works to breakdown the separation of the electronic and vibrational degrees of freedom differently than would be seen in an interaction with a TEM_{00} mode.

Electromagnetically induced breakdown of the strict separation of the electronic and nuclear coordinates leads to changes in which specific vibrational transitions are allowed upon a purely electronic dipole interaction, i.e. changes in the vibronic selection rules.[7-9] As shown below, these changes occur because the radial variation of the transverse electric field embeds quanta of the quantized normal coordinate vibrations directly into the interaction Hamiltonian. It is shown that these changes to vibrational selection rules occur even when the molecule is located off the beam's axis. Other research has shown that the coupling of the radial variation of a LG beam can affect the selection rules in absorbing molecules.[6] Chapter 3 of this dissertation uses the derivations shown below to predict changes in the selection rules governing resonance Raman scattering. Off-axis coupling between the incident LG beam and molecules throughout the illuminated sample allows for detection of changes in vibronic transitions using this traditional spectroscopic technique.

Changes in vibronic transition selections for complex molecules lead to the appearance of new molecular dynamics and behavior. The detection of these new dynamics and behavior can be used as a more thorough test of the basic physics implied in the derivation of the interaction Hamiltonian in Ref. [1]. If new dynamics are detected they may be fruitful in understanding basic molecular physical processes with important implications in fields ranging from the biophysics to energy source science.

Theoretical Derivations

The model interaction Hamiltonian derived in Ref. [1] and extended here utilizes the Power-Zienau-Wooley formalism, or multipolar formalism, of the interaction Hamiltonian. Due to the functional form and physical model of the Power-Zienau-Wooley (PZW) canonical transformation, the field variation of a LG beam (or any other higher order laser mode) enters directly into the interaction Hamiltonian via the derivation provided in Ref. [1]. This makes new and interesting interactions in molecular systems much more transparent to the investigator.

There are several excellent reviews of the PZW transformation and its relation to the typical $\mathbf{A}\cdot\mathbf{p}$ interaction Hamiltonian, also known as the minimal-coupling interaction Hamiltonian. [10-13] It is simply mentioned that there is nothing intrinsically special about the PZW transformed interaction Hamiltonian or the dynamics explored in context of this transformation.[11] The transformation simply allows one to expose augmented quantum molecular dynamics with a greater ease.

The steps of the derivation in Ref. [1] will be highlighted for the reader's reference and more thorough discussion. After the PZW transformation is complete, in the absence of a magnetic field, the interaction Hamiltonian can be written as[12]

$$H_{\text{int}} = -\int \vec{P}(\vec{r}) \bullet \vec{E}(\vec{r}) d^3\vec{r}. \qquad (2.1)$$

where

$$\vec{P}(\vec{r}) = \sum_{\alpha} e_{\alpha}\vec{r}_{\alpha} \int_0^1 du\delta(\vec{r} - u\vec{r}). \qquad (2.2)$$

is the macroscopic polarization treated as a sum over effective electric dipoles.[10] **E** is the incident electric field.[1] This interaction Hamiltonian is valid for any assembly of molecules or ions.

The general p=0, l≠0 LG beam field amplitude has the following functional form,

$$\vec{E}(\vec{r}) = \vec{E}_0 C_l \Re^l_{|l|}(\vec{r}). \qquad (2.3)$$

where $\mathbf{E}_0$ is the vector amplitude of the field and the normalization factor C_l and regular solid spherical harmonics have been defined elsewhere.[1] When this field is entered into the transformed interaction Hamiltonian of Eqn. (2.2), one can take the integral over $d^3\vec{r}$ first, thereby giving the material coordinates the spatial dependence of the incident field due to the Dirac delta function. The interaction Hamiltonian becomes,

$$H_{\text{int}} = -\sum_{\alpha} e_{\alpha} C_l \vec{r}_{\alpha} \bullet \vec{E}_0 \int_0^1 du \Re^l_{|l|}(u\vec{r}_{\alpha}). \qquad (2.4)$$

when the material system is placed on beam's radial axis and, therefore, shares a common coordinate system with the electric field.

The transition matrix elements due to this LG interaction Hamiltonian have been produced elsewhere in the literature for a pure dipole interaction,[1,10] but will be reproduced here in a slightly different form to compare to the situation when the quantum system of interest does not share a common origin with the beam. This formulation will also highlight dynamics specific to quantum systems of several internal degrees of freedom. The usually degrees of the freedom of a molecule include the electronic, vibrational, rotational and center of mass, respectively. The unperturbed wavefunction, after suitable approximations, can be written as,

$$|\Psi\rangle = |e\rangle|v\rangle|\chi\rangle|c.m.\rangle. \qquad (2.5)$$

A molecular, one-electron-LG beam interaction Hamiltonian then becomes,[1]

$$H_{\text{int}} = -\frac{16\pi^2}{3} C_l e r e^{ikR\cos\Theta} \sum_{\sigma=\pm 1} \sum_{l_1}^{|l|} \frac{\varepsilon_\sigma}{\left[(2l_1+1)!\right]^{1/2}} \left(\frac{R}{w_0}\right)^{l_1} Y_{l_1}^{\text{sgn}(l)l_1}\left(\hat{R}\right)$$
$$\times \left\{ S_1 \left(\frac{r_1}{w_0}\right)^{|l|-l_1} Y_{|l|-l_1}^{\text{sgn}(l)(|l|-l_1)}\left(\hat{r}_1\right) Y_1^{\sigma} + S_2 \left(\frac{r_1}{w_0}\right)^{|l|-l_1} Y_1^{\sigma}\left(\hat{r}_1\right) Y_{|l|-l_1-1}^{\text{sgn}(l)(|l|-l_1-1)}\left(\hat{r}_1\right) Y_1^{\text{sgn}(l)}\left(\hat{r}\right) \right\}. \tag{2.6}$$

where, r, r_1 and R are the electronic coordinate relative to a nuclear position, the nuclear position relative to the center of mass and the center of mass coordinates, as defined in Ref. [1]. The transition matrix elements for a quantum system (first order perturbative corrections to the energy) on the beam's axis in the dipole limit are,

$$M_{i\to f} = -\frac{16\pi^2}{3w_0^{|l|}} C_l e \sum_{\rho=\pm 1} \sum_{l_1}^{|l|} \frac{M_{c.m._i}^{(l_1)}}{\left[(2l_1+1)!\right]^{1/2}} \{ S_1 M_{\chi_i}^{(0,\,|l|-l_1)} \left\langle \nu_f \middle| \langle f | \left(\bar{r}_1 + \nu_1 q\right)^{\frac{|l|-l_1}{2}} r Y_1^{\rho}\left(\hat{r}\right) | i \rangle \middle| \nu_i \right\rangle$$
$$+ S_2 M_{\chi_i}^{(\rho,\,|l|-l_1-1)} \left\langle \nu_f \middle| \langle f | \left(\bar{r}_1 + \nu_1 q\right)^{\frac{|l|-l_1}{2}} r Y_1^{\text{sgn}(l)}\left(\hat{r}\right) | i \rangle \middle| \nu_i \right\rangle \}. \tag{2.7}$$

where

$$M_{c.m.i}^{(l_1)} = \left\langle c.m._f \middle| R^{l_1} e^{ikR_z\cos\Theta} Y_{l_1}^{\text{sgn}(l)l_1}\left(\hat{R}\right) \middle| c.m._i \right\rangle. \tag{2.8}$$

and

$$M_{\chi i}^{(a,b)} = \left\langle \chi \right|_i Y_1^{a}\left(\hat{r}_1\right) Y_b^{\text{sgn}(l)b}\left(\hat{r}_1\right) \left| \chi_f \right\rangle. \tag{2.9}$$

are the center of mass and rotational transition matrix elements, respectively, as defined in Ref. [1]. The S_1 and S_2 terms in this equation are unimportant for the current purpose, but have been left present for thoroughness.

The difference in this particular notation from Ref. [1] is the fact that the vibrational and electronic transition matrix elements have been left formally connected. Like many transitions involving large, complex molecules, model in Eqn. (2.7) implies that both the electronic and vibrational states change during the same transition. This is known as a vibronic transition.[7, 8, 11] In the case when there is no coupling between the electronic and vibrational degrees of freedom inherent to the molecule, the allowedness and intensity of specific vibronic transitions is determined by the symmetry of the molecule. That is, specific vibronic transitions will be allowed that include changes in the state of specific vibrations for each given molecular system.

It is instructive to note what is implied physically by the electronic and vibrational transition matrix elements in the derivation of Eqn. (2.7). Deriving the interaction Hamiltonian via the multipolar form in the manner undertaken by Alexandrescu *et al.* explicitly couples the transverse spatial variation of the incident EM field to the vibrational degree of freedom of an illuminated molecule. The transition matrix elements in Eqn. (2.7) show this coupling through the appearance of the quantized normal coordinate of the molecule. The molecule's normal coordinate in the vibronic transition matrix element then changes the selection rules governing which vibrational states of the excited electronic manifold are populated via absorption of the LG beam. The implications of this coupling are discussed more completely below.

For the case of an off-axis interaction, it is important to note what physical condition is set by the Delta function in the transformed macroscopic polarization in Eqn. (2.2). The macroscopic polarization has a non-zero value only when the coordinate matches the distance to each effective dipole from a common origin. This is trivial when the system of interest is located on the beam's axis of the LG beam. The spatial coordinates are the same for the field and quantum system because they share a common origin relative to the lab. The situation becomes more complex, however, when the system does not share a common origin with the field.

FIG. 2.1 shows the case in which the quantum system of interest is not located on the axis of the incident LG beam (at r=0). The Delta function in Eqn. (2.2) now implies that in the case of an off-axis interaction the transverse radial variation of the beam must match the length of the dipole in the molecule. The transverse radial of the LG mode is the same at the center as in its wings (scales as r^l for $p=0$, $l \neq 0$ beams). Therefore, physical intuition would suspect that the coupling between this transverse variation and the molecules quantized normal coordinates would occur everywhere in beam in the same manner it occurs at the beam's center.

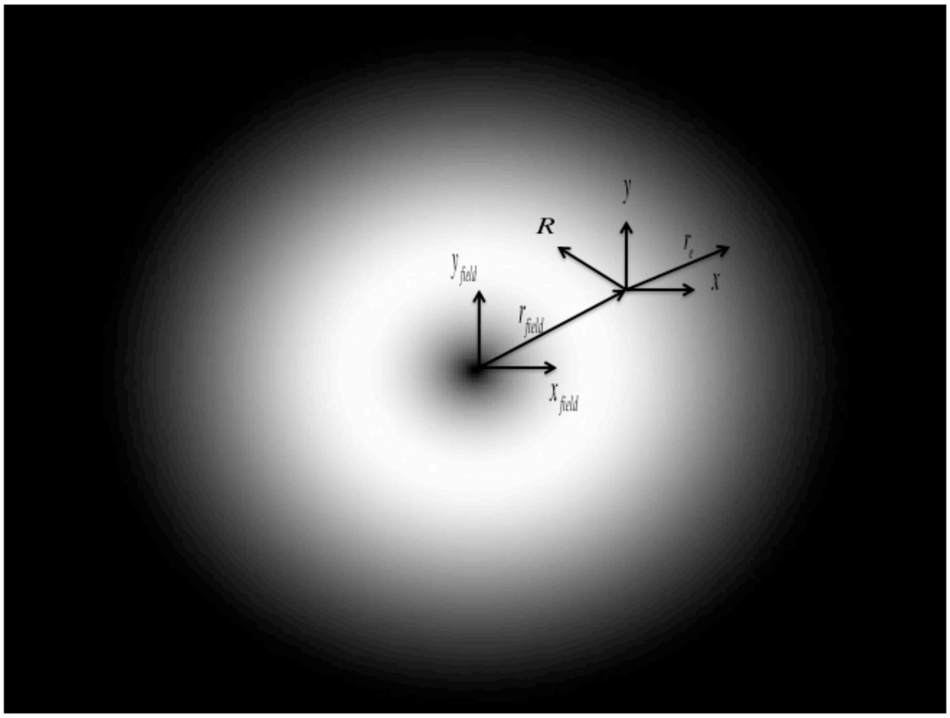

FIG. 2.1. Schematic showing different origins for E-field due to LG beam ($\mathbf{x}_{\text{field}}$ and $\mathbf{y}_{\text{field}}$) and a quantum system (**x** and **y**) some distance $\mathbf{r}_{\text{field}}$ from the field origin. One can imagine the beam propagating out of the plane of the page. (Intensity profile picture taken from Wikimedia commons)

However, a rigorous derivation of the off-axis transition matrix elements must be used to support this physical intuition.

When the field origin is a distance $\mathbf{r}_{\text{field}}$ from the origin of the quantum system, the spatial coordinate in the transformed macroscopic polarization, Eqn. (2.3) must be handled with care. In this case, we are interested in the macroscopic polarization caused by an electron in this system with reference to the system's center of mass (c.m.), i.e. the vector,

$$\vec{r}_e^{\,c.m.} = \vec{R} - \vec{r}_e. \qquad (2.10)$$

The delta function in the polarization then goes to

$$\delta\left(\vec{r} - \vec{R} - u\vec{r}_e\right). \qquad (2.11)$$

since we are interested in the effective dipoles of this system with reference to the quantum system's c.m. By transforming into the field coordinates (which must be done to evaluate the PZW-transformed interaction Hamiltonian), the quantum system's coordinates become,

$$\vec{R}^{field} = \vec{r}_{field} + \vec{R} \qquad (2.12a)$$

$$\vec{r}_e^{\,field} = \vec{r}_{field} + \vec{r}_e \qquad (2.12b)$$

$$u\vec{r}_e^{\,field} = u\vec{r}_{field} + u\vec{r}_e \qquad (2.12c)$$

The superscript in Eqns. (2.12a)-(2.12c) denotes that the coordinate has been evaluated relative to the coordinate system of the incident LG beam's electric field. The subscript 'field' denotes the coordinates of the incident LG beam's electric field. The transformed macroscopic polarization becomes,

$$\begin{aligned}\vec{P}(\vec{r}) &= \sum_{\alpha} e_{\alpha}\vec{r}_e^{\,field}\int_0^1 du\delta\left(\vec{r}-\vec{R}^{field}-u\vec{r}_e^{\,field}\right)\\ &= \sum_{\alpha} e_{\alpha}\left(\vec{r}_e+\vec{r}_{field}\right)\int_0^1 du\delta\left(\vec{r}-\vec{R}-u\vec{r}_e-\vec{r}_{field}\left[1+u\right]\right). \qquad (2.13)\end{aligned}$$

Based on the earlier definition of the transformed interaction Hamiltonian, Eqn. (2.6), we can now write,

$$H_{\text{int}} = -eC_l\vec{r}_e \bullet \vec{E}_0\int_0^1 du\mathfrak{R}_{|l|}^{l}\left(\vec{R}+u\vec{r}_e+\vec{r}_{field}\left[1+u\right]\right). \qquad (2.14)$$

for a system with one interacting electron. This derivation can be easily extended to multi-electron systems since the PZW transformation treats each charge as a single, linear contribution to the overall polarization.[10]

For a one electron atomic system, there is only one internal degree of freedom: the electronic state. Off the axis of a LG beam, it should be reasonable then to equate the radial contribution in this interaction Hamiltonian with those from higher orders of the multipole expansion of the electric field. This is evident from the fact that the spatial variation of the electric field is neglected in the first order term, the dipole term, of the multipole expansion. Any spatial variation of the external electric field eliciting an interaction with a one electron atomic system must therefore do so via higher order contributions to the multipole expansion, as has been concluded elsewhere.[2]

Other one-electron systems, however, have more internal degrees of freedoms. In Ref. [1], the H_2^+ molecular ion (one bound electron with two protons) is highlighted for having both electronic and nuclear internal degrees of freedom. To use the quantum numbers of the molecular quantum system in calculating the changes of physical parameters due to the off-axis LG interaction, we write the electron position relative to the lab in terms of the internal electronic and nuclear coordinates,

$$\vec{r}_e = \vec{r} + \vec{r}_1. \qquad (2.15)$$

where, again, $\mathbf{r}_1$ indicates the position proton 1 relative to the c.m. and $\mathbf{r}$ is the position of the electron relative to proton 1. For a particular value of l, the interaction Hamiltonian then becomes,

$$H_{\text{int}} = -eC_l\left(\vec{r} + \vec{r}_1\right) \bullet \vec{E}_0 \int_0^1 du \Re^l_{|l|}\left(\vec{R} + u\left[\vec{r} + \vec{r}\right] + \vec{r}_{field}\left[1+u\right]\right). \qquad (2.16)$$

The regular solid spherical harmonics obey specific sum rules, which produce sums of products of different powers of each coordinate in the interaction Hamiltonian.[1] That is,

$$\Re^l_{|l|}\left(\vec{R} + u\left[\vec{r} + \vec{r}_1\right] + \vec{r}_{field}\left[1+u\right]\right) \propto \vec{R}^{l-l_1}\left(u\left[\vec{r} + \vec{r}_1\right]\right)^{l_1}\left(\vec{r}_{field}\left[1+u\right]\right)^0 +$$
$$\vec{R}^{l-l_1-1}\left(u\left[\vec{r} + \vec{r}_1\right]\right)^{l_1}\left(\vec{r}_{field}\left[1+u\right]\right)^1 + \ldots \qquad (2.17)$$

Smaller values of l (l=1 and l=2) lead to non-zero powers of the c.m. and internal coordinates of the molecule that contribute to the interaction. These non-zero powers of the quantum system's variables in the interaction Hamiltonian are present at the detriment of the field coordinate, as seen in the first term on the right hand side of Eqn. (2.17). For this reason, coupled with the fact that we are implicitly assuming the semi-classical approximation (the field is treated classically), we will ignore the contribution of the field coordinate to the interaction Hamiltonian from this point on.

Alexandrescu *et al.*[1] have simplified this interaction Hamiltonian in the instance that the field and molecule share a common origin. This allows for a full appreciation of the way in which a LG beam's radial and azimuthal variation affect the interaction with the molecule, as we have already seen via the vibronic transition matrix elements in Eqn. (2.8).

In our situation, however, we are effectively evaluating the functional form of the LG beam at one position of azimuthal phase. It seems reasonable to think that integrating the phase variation over the extent of the molecule (as would be done in a transition matrix element) could lead to other interesting effects in optical transitions. These effects are also likely strongly related to the quantized orbital angular momentum that a LG beam carries. For the current treatment, however, we are going to neglect these azimuthal variation effects so as to focus our attention on how the radial variation couples to our system of interest.

The simplified interaction Hamiltonian becomes (ignoring longitudinal effects of the field),

$$H_{\text{int}} = -\frac{16\pi^2}{3} C_l e r e^{ikR\cos\Theta} \sum_{\sigma=\pm 1} \sum_{l_1}^{|l|} \frac{\varepsilon_\sigma}{\left[(2l_1+1)!\right]^{1/2}} \left(\frac{R}{w_0}\right)^{l_1} Y_{l_1}^{\operatorname{sgn}(l) l_1}\left(\hat{R}^0\right) \{ S_1 \left(\frac{r_1}{w_0}\right)^{|l|-l_1} Y_{|l|-l_1}^{\operatorname{sgn}(l)(|l|-l_1)}\left(\hat{r}_1^0\right) Y_1^{\sigma}\left(\hat{r}^0\right)$$
$$+ S_2 \left(\frac{r_1}{w_0}\right)^{|l|-l_1} Y_1^{\sigma}\left(\hat{r}_1^0\right) Y_{|l|-l_1-1}^{\operatorname{sgn}(l)(|l|-l_1-1)}\left(\hat{r}_1^0\right) Y_1^{\operatorname{sgn}(l)}\left(\hat{r}^0\right) \}. \tag{2.18}$$

where we are denoting the fact that the phase dependent part of the electric field has been evaluated at one particular point of φ in the beam with the superscript 0. The S_1 and S_2 terms in this equation are unimportant for our current purpose, but have again been left present for thoroughness.

The affect of the azimuthal phase of the incident field is contained completely within the spherical harmonic functions in the interaction Hamiltonian. Since we have evaluated the electric field's azimuthal dependence at one phase point (but we can still vary the radial position), these spherical harmonics can now be taken out of the interaction Hamiltonian because they will no longer couple to the quantized degrees of the freedom of the molecule. They are constants.

To understand the ways in which the one electron, off-axis interaction with a LG beam changes vibronic transition of a molecule, we now must calculate the transition matrix elements. Again, we will use the standard unperturbed molecular wavefunction, found in Eqn. (2.6) to calculate the transition matrix elements. The transition matrix elements for a one electron interaction with a LG beam off the beam’s axis become,

$$M_{i\to f} = -\frac{16\pi^2}{3w_0^{|l|}} C_l e \sum_{\rho=\pm1} \sum_{l_1}^{|l|} \frac{M_{c.m._i}^{(l_1)}}{\left[(2l_1+1)!\right]^{1/2}} \{S_1 M_{\chi_i}^{(0,\,|l|-l_1)} \left\langle v_f \middle| \langle f | (\overline{r}_1 + v_1 q)^{\frac{|l|-l_1}{2}} r Y_1^{\rho}(\hat{r}) | i \rangle \middle| v_i \right\rangle +$$

$$S_2 M_{\chi_i}^{(\rho,\,|l|-l_1-1)} \left\langle v_f \middle| \langle f | (\overline{r}_1 + v_1 q)^{\frac{|l|-l_1}{2}} r Y_1^{\mathrm{sgn}(l)}(\hat{r}) | i \rangle \middle| v_i \right\rangle \}. \qquad (2.19)$$

where we have simultaneously substituted the quantized nuclear vibration of the molecule into the interaction term with the equation,

$$\vec{r}_1 = r_1 + \vec{v}_1 q_1. \qquad (2.20)$$

where r_1 is the equilibrium position of proton 1. We will neglect changes in the rotational and the c.m. transition matrix elements since there is no longer an azimuthal dependence in the interaction Hamiltonian. Without the azimuthal dependence transitions of the states of these degrees of freedom are not changed in an interesting way.

The transition matrix elements in Eqn. (2.19) have been written in this form to explicitly display an interesting result. Despite the molecule being off-axis this interaction Hamiltonian still a provides an electromagnetic coupling between the electronic and nuclear degrees of freedom. This coupling is due to the radial dependence of the field. Most important is that the amended vibronic transition matrix elements found in Eqn. (2.8) are the same in Eqn. (2.19). Therefore, the derivation used in Ref. [1] predicts that if one were to interact a LG beam with a molecule capable of vibronic transition using the appropriate spectroscopic technique, one would be able to measure the changes in the behavior and dynamics associated with specific vibronic transitions. These changes in the vibronic selection rules would occur irrespective of the location of the molecule in the profile of the incident laser beam.

In the usual treatment of quantum molecular dynamics, one makes several approximations that can be characterized under the standard heading of adiabatic approximations (AA).[7-9, 12] Which particular AA one chooses to use formally depends explicitly which specific terms in the unperturbed molecular Hamiltonian are neglected and which are kept. From these terms one can solve for the unperturbed electronic structure of the molecule. Going through each different AA and discussing their differences is not in our interests. In order to write a wavefunction like that found in Eqn. (2.6), one must make some kind of adiabatic approximation to separate the dynamics of the electronic and nuclear degrees of freedom.

When the electronic and nuclear degrees of freedom of a molecular can no longer be rigorously separated the optical behavior comes from vibronic coupling, generally. Therefore, vibronic coupling describes a great deal of physically distinct processes. These physically distinct processes depend on the specific AA that was originally chosen in order to write out an unperturbed, molecular wavefunction. When vibronic coupling occurs during an electromagnetic interaction the Condon approximation is also relaxed. This approximation does not hold in this case since both the electronic and nuclear degrees of freedom are reacting to the perturbing EM field.[7, 8]

While vibronic coupling plays a small role in smaller molecules, this coupling plays a very important role in larger molecules. This is especially true where certain electronic transitions are forbidden due to symmetry considerations. Benzene, C_6H_6, is the most notable example of this phenomenon.[7] The transition between the ground and first excited electronic manifold of benzene is forbidden due to symmetry of the electronic states. On the other hand, such a transition of sizable intensity is predicted and observed in the electronic absorption spectrum of benzene. This transition becomes allowed when coupling between the electronic transition and specific vibrations shared by both electronic states is considered.

In case the of benzene, the vibronically allowed lowest energy transition is understood in the context of symmetry. As already pointed out, the transition between the electronic ground state and the lowest electronic excited state is forbidden due to the character of those states and that of the transition dipole moment. The symmetry of these parameters of benzene's structure come from the operations of its point group, D_{6h}. Physically the coupling between the electronic and vibrational degrees of freedom lowers the effective symmetry of the whole molecule. The transition of interest is no longer as strictly forbidden because the symmetry of the molecule is longer described by the D_{6h} point group. In this view, one can physically understand vibronic coupling in a highly symmetric molecule like benzene as an effective lowering of the symmetry of the entire molecule. Specific ‘motions’ of the nuclei are excited during a electronic transition reducing the symmetry of the molecule resulting in measurable intensity in ‘forbidden’ transitions.

This symmetry-lowering process is not, however, dependent on any properties of the incident electromagnetic field. It is solely dependent on the structure of the molecule of interest. A transition can be observed at a ‘forbidden’ frequency when a vibration of the necessary symmetry interacts with the symmetries of the electronic states and electric dipole involved. The symmetry of these molecular parameters is all that is necessary to understand this process.

When a large, complex molecule interacts via one electron with a LG beam, the extension of the derivation from Ref. [1] predicts what functionally corresponds to a breakdown of an AA. Since the model predicts an AA break down due to the direct coupling of the LG electric field to the vibrational degrees of freedom of the molecule, we can formally call this electromagnetically-mediated vibronic coupling in the traditional sense. We must also relax the Condon approximation since the nuclei of this molecule are reacting to the incident field at the same time as the electronic degrees of freedom.

The physical interpretation of the PZW proposed above in the context of LG beam-molecule interactions then has important implications in understanding the derived EM-mediated vibronic coupling in eqns. (2.9) and (2.19). In the frame of the discussion of the symmetry-lowering in molecular behavior, the transverse variation of the LG beam acts as a symmetry element in the transition matrix elements. This added symmetry element to the transition matrix element comes in the form of a quantum of the molecule’s normal coordinates due to direct coupling with the incident EM field. Adding a symmetry element to the optical transition matrix element changes the rules for allowed transitions resulting in new vibrational behavior in molecules upon an interaction with an LG beam. These changes due to a new form of coupling to a LG beam should then be considered vibronic coupling in the exact same sense understood in the case of molecular symmetry-lowering.

While in traditional treatments one depends on the molecular system to behave in a way in which the AA cannot account for all the dynamics, here the model of Ref. [1] clearly predicts the breakdown of the AA due a EM interaction. This is shown explicitly for a one-electron interaction of a molecule with a LG beam in the above derivation. Since the functional form of the PZW interaction Hamiltonian sums over the involved dipole moments, this treatment extends to larger molecules interacting with the LG field. One simply sums over each of the pertinent electrons populating the highest occupied molecular orbital and represents the position of a nucleus as a sum over the molecule's quantized vibrations. The one electron molecular interaction with a LG beam is fully extendable to a larger molecule where vibronic coupling will play a more significant role.

Most importantly, for highly symmetric molecules this model predicts a LG interaction can couple to specific nuclear vibrations that will change the absorption of specific frequencies of light. Since highly symmetric molecules have the strictest rules for transitions between electronic states, introducing a field that can couple to specific nuclear vibrations will have the effect of lowering the symmetry of the entire molecule and, therefore, augment the molecule's absorption spectra. The specific changes depends on the symmetry of the specific molecule since such considerations will determine which transition are allowed or forbidden. It is reasonable to think that some kind of effect will present in all highly symmetric, large molecules. Using a LG beam to determine if specific vibronic transitions are reduced or increased in intensity can serve as a meaningful test of the model first presented in Ref. [1] and then extended here.

The above treatment also shows that since the radial variation of a LG beam is not relegated to the center of the beam's profile, this effect of affecting symmetry of the transition matrix elements should exist off the beam's center. This is important since at the beam's center the electric field amplitude drops to zero, thus driving the dipole interaction to zero as well. Since this effect of symmetry-lowering is no longer dependent on molecule 'sensing' the full azimuthal variation of the beam, this model predicts a discernable effect in traditional spectroscopic measurements that could utilize LG beams.

Complex molecules also raise concerns over the results derived in this chapter. The number of normal coordinates increase more rapidly than the number of atoms in the molecule (3N-6 vs. N). Therefore, as the number of atoms in a molecule increases, the number of vibrational degrees of freedom of the molecule will increase more dramatically. With many quantized vibrations, it is difficult to say to which normal coordinates the radial variation of a LG beam couple based on the derivations above. Since only a small number of vibrations are excited in an electronically allowed transition, it could be that one of these such modes must be aligned in a specific manner with respect to the incident direction of the LG beam.

As will be more fully discussed in Chapter 3 and elsewhere, the position of any nuclei in a polyatomic molecule can be written as a linear combination of the molecule's quantized normal coordinates.[1] Therefore, it seems reasonable to begin a physical understanding of these amended EM interactions with the assumption that all of a molecule's normal coordinates can couple to the radial variation of the LG beam. From that point, specific spectroscopic tests can allow for the distinction in the changes in the behavior in specific types, combinations or numbers of vibrations.

While thus far in the literature optical absorption has been used to understand how the derived changes could manifest themselves, it is not a spectroscopic technique sensitive to changes in the vibrational behavior of molecules. For this reason, Chapter 3 will use the interaction Hamiltonian and transition matrix elements derived above to calculate an effective Raman scattering cross-section and predict changes in the resonance Raman spectra of molecules. As a sensitive vibrational spectroscopic technique that necessitates an electronic transition, resonance Raman scattering spectroscopy offers itself as an ideal tool to test the predicts for on and off-axis amending vibrational behavior of molecules.

Conclusions

Despite the fact that the radial dependence of the electric field of higher order laser beams, most notably the Laguerre-Gauss (LG) beams, has been neglected in past treatments of material interactions, we show here that this dependence mediates new and interesting phenomena in the field of molecular physics, even off the beam's axis. These new phenomena are inherently due to the presence of quantized internal degrees of freedom beyond the electronic states found in molecular systems. Because of this fact, we expect that other systems that display similar internal degrees of freedom will be modulated in a similar fashion when interacting with higher order, radially dependent laser fields.

Specific to the molecular discussion, a radially dependent electric field of a LG beam will contribute a vibronic-like coupling in large, complex molecule. EM-mediated vibronic coupling is similar to its molecular-structure counterpart in name and process. Through its transverse radial variation, the LG beam adds a symmetry element to the overall interaction. This addition leads to the activation and de-activation of specific electronic transitions in the optical region of the EM spectrum depending on the specific molecule of interest. These predictions may lead to deeper understanding of molecular inter- and intra-actions useful in fields ranging from spectroscopy and molecular electronics to biophysics and pharmaceutical sciences.

References:

1. A. Alexandrescu, D. Cojoc and E. Di Fabrizio, Phys. Rev. Lett. **96** (24) (2006).
2. M. Babiker, C. R. Bennett, D. L. Andrews and L. C. D. Romero, Phys. Rev. Lett. **89** (14) (2002).
3. W. K. Lai, M. Babiker and L. Allen, Optics Communications **133** (1-6), 487-494 (1997).
4. D. McGloin, N. B. Simpson and M. J. Padgett, Applied Optics **37** (3), 469-472 (1998).
5. W. L. Power, L. Allen, M. Babiker and V. E. Lembessis, Physical Review A **52** (1), 479-488 (1995).
6. M. van Veenendaal and I. McNulty, Phys. Rev. Lett. **98** (15) (2007).
7. D. C. Harris and M. D. Bertolucci, *Symmetry and spectroscopy: an introduction to vibrational and electronic spectroscopy*. (Oxford University Press, New York, 1977).
8. J. L. McHale, *Molecular spectroscopy*. (Prentice Hall, 1999).
9. G. Fischer, *Vibronic coupling: the interaction between the electronic and nuclear motions*. (Academic Press, London ; Orlando, Fla., 1984).
10. C. Cohen-Tannoudji, J. Dupont-Roc and G. Grynberg, *Photons and atoms: introduction to quantum electrodynamics*. (Wiley, New York, 1989).
11. D. P. Craig and T. Thirunamachandran, *Molecular quantum electrodynamics: an introduction to radiation-molecule interactions*. (Academic Press, London ; Orlando, 1984).
12. S. Mukamel, *Principles of nonlinear optical spectroscopy*. (Oxford University Press, New York, 1995).

13. E. A. Power, *Introductory quantum electrodynamics*. (American Elsevier Pub. Co., New York, 1965).

Chapter 3:
Inelastic Scattering of Laguerre-Gauss Beams From Molecules

Introduction

As shown in Chapter 2, the introduction of Laguerre-Gauss (LG) beams affects molecular behavior. Using the interaction Hamiltonian developed by Alexandrescu et al. for on-axis interactions and the extension of that interaction Hamiltonian for off-axis interactions, the functionally, radially varying electric field of a LG beam affects the coupling between the electronic and vibrational degrees of freedom of a polyatomic molecular system during the absorption of a LG beam, otherwise known as vibronic coupling.[1] This prediction of radial coupling is similar to those made in the case of x-ray spectroscopy of molecules.[2]

However, changes in vibronic structure and processes due are difficult to resolve via molecular absorption measurements. In contrast to absorption, light scattering processes access changes in the vibrational dynamics and behavior of a molecule.[3] The intensity of inelastic light scattering is enhanced when the scattering process occurs on resonance with an electronic transition. Based on these considerations, resonance Raman scattering from model molecular systems will be used to test the predictions of the interaction Hamiltonian discussed in Chapter 2.

The theoretical developments of Chapter 2, therefore, must be extended to inelastic light scattering. This chapter will follow as a thorough introduction to Raman scattering, the resonance condition in Raman scattering and development of the effective scattering transition probability induced by an incident LG beam. From there, the physical implications of the inelastic LG beam scattering are discussed as well as the prediction of changes to specific observables measured in the inelastic light scattering from the molecule's totally symmetric vibrations.

To predict how an LG beam will change the resonantly enhanced Raman scattering spectrum of a molecule, changes in both the populations and coherences of totally symmetric vibrations are examined. First, it is shown that the spectra of overtones for molecules highly displaced excited electronic states will show the largest changes due to LG excitation. Also, these effects are largest for vibrations with lower frequencies. Second, interference effects are examined and predictions for changes in 'baseline' spectra are proposed. It is shown that the interferometric modulation of the intensity of peaks present in scattering spectra using plane wave excitation can be controlled by changes to the weighting of different quantum pathways introduced by the LG excitation.

By amending selection rules for vibronic transitions, LG beams allow researchers to access information not typically allowed via light scattering. Given the highly controllable and large parameter space that higher order laser modes offer, the coupling between the radial variation of an electric field and a molecule's vibrations also provides other possible mechanisms for controlling the behavior of a molecule. Such control could allow researchers to better understand biomolecules, more fully characterize and identify unknown molecular samples and provide insight into molecular materials important to fields ranging from energy science to information technology.

Resonance Raman Scattering

The quantity of interest in scattering processes is the differential cross-section, determined using the Kramers-Heisenberg-Dirac equation.[3, 4] Generally for a interaction between an incident EM field and a single particle populating in a distinct final state, the one uses differential scattering cross-section to calculate the probability of scattering light in a frequency range of dω′ along the wavevector k′ direction through a solid angle $d\Omega$. In the case of the minimally coupling interaction Hamiltonian, this scattering transition probability becomes[4],

$$\frac{d^2\sigma}{d\Omega d\left(\hbar\omega_k^{'}\right)}=\left(\frac{e}{mc}\right)^2\left|\sum_N \frac{\langle F|\vec{A}\bullet\vec{p}|N\rangle\langle N|\vec{A}\bullet\vec{p}|I\rangle}{E_N-E_I-\hbar\omega_k-i\hbar\Gamma_0}+\frac{\langle F|\vec{A}\bullet\vec{p}|N\rangle\langle N|\vec{A}\bullet\vec{p}|I\rangle}{E_N-E_I+\hbar\omega_k^{'}-i\hbar\Gamma_0}\right|^2$$

$$\times\delta\left(E_F-E_I+\hbar\omega_k-\hbar\omega_k^{'}\right). \qquad (3.1)$$

where I, N, F indicate the initial, intermediate, and final states of the particle, respectively, and E_I, E_F, and E_N indicate the energy of the initial, final, and intermediate states of the molecule, respectively. ω_k is the frequency of the incident light along the wavevector k direction and the phenomenological decay rate, Γ_0, has been added due to the finite lifetime of the immediate state. In the case of inelastic, or Raman, scattering, the delta function maintains the conservation of the incident energy between the scattered light and the excited final state.

The two factors of the **A·p** interaction appear in eqn. (3.1) for a straightforward reason. Light scattering necessitates both the annihilation and creation of seperate excitations of the vacuum field states. This occurs directly from a single higher order **A·A** term appearing in the minimal coupling interaction Hamiltonian, leading to Thomson scattering. Contributions from Thomson scattering to the cross-section have been ignored in eqn. (3.1) since this chapter treats incident light frequencies close to an electronic resonance frequency. Products of the vector potential, **A**, lead to terms containing both annihilation and creation operators when the fields are quantized. Therefore, two factors of the **A·p** preserve the number of photons correctly for a light scattering processes.[4]

In the case of molecules interacting with EM fields, the quantity within the squared brackets of eqn. (3.1) is known as the molecular polarizability, α. To see how Raman scattering occurs in molecules, the eigenstates of the molecule are decomposed into their vibrational and electronic contributions. For plane wave illumination, the functional form of α is caste into a new light by writing it as,

$$\alpha_{\sigma\rho} \propto \sum_{e,v_n} \Big[\frac{\langle v_f|\langle g|\vec{\mu}\bullet\vec{\varepsilon}_\sigma^*|e\rangle|v_n\rangle\langle v_n|\langle e|\vec{\mu}\bullet\vec{\varepsilon}_\rho|g\rangle|v_i\rangle}{E_e+E_{v_n}-E_{v_i}-E_L-i\hbar\Gamma_0}+ \frac{\langle v_f|\langle g|\vec{\mu}\bullet\vec{\varepsilon}_\rho^*|e\rangle|v_n\rangle\langle v_n|\langle e|\vec{\mu}\bullet\vec{\varepsilon}_\sigma|g\rangle|v_i\rangle}{E_e+E_{v_n}-E_{v_f}+E_L-i\hbar\Gamma_0}\Big]. \qquad (3.2)$$

where the energy of the incident light is now denoted by E_L. The vibrational states are denoted by v and electronic states by lower case letters. The other degrees of freedom of the molecule are ignored for the moment.

The resonance condition is met when,

$$E_e+E_{v_n}-E_{v_i}=E_L. \qquad (3.3)$$

On resonance, the denominator of the first term of eqns. (3.1) and (3.2) becomes significantly smaller causing the scattering from this term to dominate the intensity scattered by the molecule. Physically, since a distinct electronic excited state is participating in the scattering process as an intermediate state, the Feynman diagram in which the intermediate state is produced via an emission process makes no contribution in the resonant case.[4] While this treatment is instructive, using the general formalism coming out of eqn. (3.1) allows understanding how changes in the transverse mode of the excitation field can affect an effective scattering probability, as is discussed below.

As seen in Chapter 2, in order to write a unperturbed wavefunction, one must invoke the adiabatic approximation.[5] Once this approximation is made, eqn (3.1) is transformed into the multipolar interaction Hamiltonian to determine an effective scattering transition probability in the case of LG beam excitation. Exmination of the effective transition probability allows prediction of the selection rules governing this scattering process as well as the the consequences of those changes.

In resonance Raman scattering there are two equivalent models that predict changes in spectra due to vibronic breakdown of the adiabatic approximation.[3] An expansion of the the electronic transition dipoles in the nuclear normal coordinates gives analytical solutions to abiabatic breakdown as,

$$M^{i}_{ge} = M^{i}_{ge}(0) + \sum_{j} \left(\frac{\partial M^{i}_{ge}(Q)}{\partial Q_j} \right)_0 Q_j + \ldots \,, \qquad (3.4)$$

where,

$$M^{i}_{ge} = \langle g | \vec{\mu} \bullet \vec{\varepsilon}_{\sigma} | e \rangle . \qquad (3.5)$$

is the electronic transition matrix element coupled to the field along the ith linear polarization direction. This formalism of corrections to the adiabatic approximation can be physically understand via coupling between the nuclear and electronic degrees of freedom of a molecule. As the coupling between these degrees of freedom becomes stronger (the larger the value of the derivative in eqn. (3.4)), the higher order terms in the above expansion provide a larger contribution to the resonance Raman scattering process. When these expanded matrix elements are entered back into eqn. (3.2), the molecular polarizability in the resonance condition becomes,

$$\alpha_{\sigma\rho} \propto \sum_{E,n} \{ \frac{M_{ge}^{\sigma}(0) M_{ge}^{\rho}(0) \langle \nu_f | \nu_n \rangle \langle \nu_n | \nu_i \rangle}{E_e + E_{\nu_n} - E_{\nu_i} - E_L - i\hbar\Gamma_0} + \sum_j [\frac{\left(\frac{\partial M_{ge}^{\sigma}}{\partial Q_j} \right)_0 M_{ge}^{\rho}(0) \langle \nu_f | Q_j | \nu_n \rangle \langle \nu_n | \nu_i \rangle}{E_e + E_{\nu_n} - E_{\nu_i} - E_L - i\hbar\Gamma_0} + \frac{\left(\frac{\partial M_{ge}^{\rho}}{\partial Q_j} \right)_0 M_{ge}^{\sigma}(0) \langle \nu_f | \nu_n \rangle \langle \nu_n | Q_j | \nu_i \rangle}{E_e + E_{\nu_n} - E_{\nu_i} - E_L - i\hbar\Gamma_0}] \}. \tag{3.6}$$

to first order in the jth normal coordinate of the molecule's vibrations.

We use a molecular system that does not change symmetry upon the electronic excitation to give an example of where the different terms in eqn. (3.6) enhance the scattering from specific vibrational modes. This is the case when only the equilibirum bond lengths of a polyatomic molecule increase on the excited state. For a typical system that does not change symmetry upon resonant excitation, only the totally symmetric vibrational modes of the molecule possess an asymmetrically displaced excited state potential energy surface with respect to that of the ground state. Asymmetric displacement of the excited electronic state means that the ground and excited electronic states do not share a common basis set of vibrational states. Different vibrational basis sets mean that the vibrational overlap integrals are not subject to strict orthogonality relationships. This relaxation of selection rules allows transitions between different states of these totally symmetric vibrations.

The intensity of these transitions depends on the overlap of the vibrational states involved. The vibrational overlap is related to the Franck-Condon factor for the associated states. For this reason, transitions allowed via this physical mechanism are called Franck-Condon active vibrations. While the nontotally symmetric modes of the molecule are not Franck-Condon active normally, physical mechanisms such as specific Jahn-Teller distorsions can activate non-totally symmetric vibrations via similar terms in the molecular polarizability.

When the resonance condition is met, the first term in this polarizability is known as the Franck-Condon, or Albrecht 'A', term[3]. In the type of molecular system of interest here, the 'A' term in the molecular polarizability in eqn. (3.6) enhances inelastic scattering from totally symmetric vibrations. Given the above discussion, this makes sense physically. When the ‘A’ term is inspected, we see that it is functionally dependent on the overlaps between the initial and intermediate and intermediate and final vibrational states, respectively. Since only the totally symmetric vibrations of our example system are possess non-zero Franck-Condon overlaps between states of differing quantum numbers, we expect that the scattering process excites the totally symmetric vibrations of the molecule. So called Franck-Condon progressions are easily visible in resonance Raman spectra in such situations[3].

The lack of an asymmetric displacement of the potential surfaces of the non-totally symmetric modes means that the ground and excited electronic states share the same basis of vibrational states. However, excited electronic states possess two symmetric potential energy surfaces about the equilibrium geometry of some non-totally symmetric vibrations. These symmetric, doubled-welled potential energy surfaces allow for excitation of overtones and even multiples of overtones of these vibrations via a Franck-Condon mechanism. In the case of the fundamental of these vibrations however, the is no Franck-Condon mechanism allowing resoannce Raman activity.

The second and third terms of eqn. (3.6) (collectively known as the Herzberg-Teller or Albrecht ‘B’ term[3]), however, contain a contribtution from breakdown of the adiabatic approximation. This is seen through the functional dependence of these terms the jth normal coordinate of the molecule. While this form looks functionally different from the discussion concerning benzene in Chapter 2, the essential physics are the same. Coupling of the normal coordinates to the electronic dipole transition itself are allowing transitions otherwise forbidden due to symmetry of the molecule.

The ‘B’ term denotes the second and third terms on the right hand side of eqn. (3.6). In first of these two terms, the excitation transition (along the σ-direction) is dependent on the Franck-Condon overlap, while the emission transition (along the ρ-direction) has one unit of the normal coordinate embedded in the vibronic transition matrix element. This means that upon the electronic excitation to a state possessing a single, non-displaced potential energy well, only the transition between the vibrational ground states of each respective electronic state is allowed. However, the vibrational population can transition to the first excited state of a nontotally symmetric mode on the electric ground potential surface when the scattered photon is emitted. The difference in the selection rules is due to the presence of the normal coordinate, Q, in the vibronic transition matrix element.

Conversely, for the same type of molecule the third term of eqn. (3.6) contains one unit of a normal coordinate in the excitation transition while the emission transition depends on the Franck-Condon overlap. The normal coordinate now allows for the excitation of a nontotally symmetric mode during the electronic transition. When the photon is scattered only the first excited vibrational state on the ground manifold can be populated because the vibrational quantum number cannot change without a unit of the normal coordinate for the electronic states treated here. Again, the selection rules for this transition are restricted by the fact that the ground and excited electronic states share the same basis sets of vibrational states.

One can also construct the resonant molecular polarizability from the combinations of first order perturbative corrections to the molecular electronic wavefunction[3].

$$|g\rangle' = |g\rangle + \sum_{j} \sum_{r \neq e} \frac{H_{gr}^{j} Q_{j}}{E_g - E_r} |r\rangle, \qquad (3.7)$$

becomes the correction to the unperturbed wavefunction, $|g\rangle$,where,

$$H_{gr}^{j} = \langle g| \left(\frac{\partial \hat{H}}{\partial Q_j} \right)_0 |r\rangle. \qquad (3.8)$$

is known as the vibronic coupling matrix element and Q_j is the j^th normal coordinate of the molecule. To first order in the j^th normal coordinate, the resonant molecular polarizability becomes,

$$\alpha_{\sigma\rho} \propto \sum_{E,v} \frac{M_{ge}^{\sigma}(0) M_{ge}^{\rho}(0) \langle v_f | v_n \rangle \langle v_n | v_i \rangle}{E_e + E_{v_n} - E_{v_i} - E_L - i\hbar\Gamma_0} + \sum_{j} \frac{H_{er}^{j}}{E_e - E_r} [\frac{M_{ge}^{\sigma}(0) M_{ge}^{\rho}(0) \langle v_f | v_n \rangle \langle v_n | Q_j | v_i \rangle}{E_e + E_{v_n} - E_{v_i} - E_L - i\hbar\Gamma_0}$$
$$+ \frac{M_{ge}^{\sigma}(0) M_{gr}^{\rho}(0) \langle v_f | Q_j | v_n \rangle \langle v_n | v_i \rangle}{E_e + E_{v_n} - E_{v_i} - E_L - i\hbar\Gamma_0}]. \qquad (3.9)$$

The Herzberg-Teller formalism produces an interesting picture. When a state r is close in energy to state e, they can be mixed by a nontotally symmetric vibration to give higher order terms in the molecular polarizability. The r state effectively takes away some intensity from the transition between the ground state and state e. At the same time, this embends a unit of the normal coordinate of that vibration in the vibronic transition matrix element to amend the vibrational selection rules during the electronic transition. Physically, this the same phenomenon seen for the model in which the electronic transition dipole is expanded in the normal coordinates of the molecule, as discussed earlier.

Understanding the baseline Raman scattering behavior of a molecular system allows for a full appreciation for the ways that the model proposed by Alexandrescu et al. and extended in Chapter 2 affects resonance Raman scattering from molecules. In order for this appreciation to begin, the calculation of effective scattering transition probability caused by the LG interaction must be completed. From there, any ‘new’ physics should be more transparent.

Light Scattering Due to LG Beams

As seen in chapter 2, Alexandrescu et al. have proposed that when a LG beam interacts via one electron with a diatomic molecular, the interaction Hamiltonian can be written as[1],

$$H_{\text{int}} = -\frac{16\pi^2}{3} C_l e r e^{ikR\cos\Theta} \sum_{\sigma=\pm1} \sum_{l_1}^{|l|} \frac{\varepsilon_\sigma}{\left[(2l_1+1)!\right]^{1/2}} \left(\frac{R}{w_0}\right)^{l_1} Y_{l_1}^{\text{sgn}(l)l_1}\left(\hat{R}\right) \{ S_1 \left(\frac{r_1}{w_0}\right)^{|l|-l_1} Y_{|l|-l_1}^{\text{sgn}(l)(|l|-l_1)}\left(\hat{r}_1\right) Y_1^{\sigma}\left(\hat{r}\right)$$

$$+ S_2 \left(\frac{r_1}{w_0}\right)^{|l|-l_1} Y_1^{\sigma}\left(\hat{r}_1\right) Y_{|l|-l_1-1}^{\text{sgn}(l)(|l|-l_1-1)}\left(\hat{r}_1\right) Y_1^{\text{sgn}(l)}\left(\hat{r}\right) \}. \qquad (3.10)$$

when the molecule is located on the radial axis of the beam. In eqn. (3.10), R, r_1 and r correspond to the center of mass, first nuclear and electronic (relative to the first nuclei) positions, respectively. The azimuthal variation of the LG wave front is captured in the spherical harmonic functions in this interaction Hamiltonian. S_1 and S_2 do not depend on the variables of the molecule, but are kept for completeness in this instance.

Eqn. (3.10) is derived using a canonical transformation of the typical **A˙p** interaction Hamiltonian used throughout the spectroscopy literature[6-9]. As shown in Chapter 2, when the canonical transformation is completed, the interaction Hamiltonian will contain the molecular coordinates, degrees of freedom, as variables in its functional form. This can be understood physically as the dipole electronic transitions mediating a coupling between the transverse field variation and the internal degrees of freedom of the molecule.

It was also shown in Chapter 2 that in the off-axis geometry, when the molecule is not located exactly on the radial axis of the LG beam, the electronic dipole transition still mediates a coupling between the radial variation of the transverse electric field and the vibrational degrees of freedom. Since this coupling occurs off-axis it should be much easier to detect than changes to the other degrees of freedom, which necessitates being on the beam's axis. Also, given that Raman spectroscopy excited in the resonance condition produces information on the vibrational activity of the molecule of interest, this treatment focuses on the ways in which the LG beam amends the expected structure and dynamics of vibrational Raman processes.

In order to understand how this interaction Hamiltonian affects resonance Raman scattering, the one must calculate the probability that a molecule scatters a photon and populates a final state distinct from the initial state. Explicitly, after making the canonical transformation from eqn. (3.1) the scattering probability becomes,

$$\frac{d^2\sigma^{LG}}{d\Omega d\left(\hbar\omega_k^{'}\right)} = \left| \sum_N \frac{\langle F|H_{\text{int}}^{LG}|N\rangle\langle N|H_{\text{int}}^{LG}|I\rangle}{E_N - E_I - \hbar\omega_k - i\hbar\Gamma_0} + \frac{\langle F|H_{\text{int}}^{LG}|N\rangle\langle N|H_{\text{int}}^{LG}|I\rangle}{E_N - E_I + \hbar\omega_k^{'} - i\hbar\Gamma_0} \right|^2 \times \delta\left(E_F - E_I + \hbar\omega_k - \hbar\omega_k^{'}\right). \qquad (3.11)$$

Again, when one invokes the resonance condition the left hand term in the brackets of eqn. (3.11) dominates the scattering process. For interactions with the LG beam in which the angular momentum of the beam's polarization couples to the electronic degree of freedom to preserve the selection rules for a purely electronic dipole transition, only the first term in the brackets of eqn. (3.10) contributes. To concentrate on the vibrational and electronic degrees of freedom of the system, eqn. (3.10) is re-written as,

$$H_{\text{int}}^{LG} = \sum_{\rho \equiv \pm 1} \varepsilon_\rho \sum_{l_1}^{|l|} C_{l_1} \left\{ \sum_{s=0}^{|l|-l_1} \begin{pmatrix} |l|-l_1 \\ s \end{pmatrix} \left(\sum_j Q_j \right)^s \right\} erY_1^\rho(\hat{r}). \qquad (3.12)$$

where the nuclear coordinate relative to the center of mass, r_1, has been replaced by a sum over the normal coordinates as in Ref. [1]. That is,

$$\vec{r}_1 \propto \sum_j \vec{Q}_j. \qquad (3.13)$$

This replacement allows for the extension of the interaction Hamiltonian to N-atom, polyatomic molecules with 3N-6 normal coordinates. Highlighting this formulation of the PZW transformed scattering probability for a molecule-LG beam interaction allows for a more transparent appreciation for the way in which the coupling between electronic and vibrational degrees of freedom is affected by the nature of the incident light field. To understand the changes in the vibrational dynamics of the molecule with respect to changes in the incident laser mode,

$$|I\rangle = |g\rangle |v_i\rangle \qquad (3.14a)$$

$$|N\rangle = |r\rangle |v_n\rangle \qquad (3.14b)$$

$$|F\rangle = |g\rangle |v_f\rangle. \qquad (3.14c)$$

as initial, intermediate and final unperturbed states, respectively, for electronic and vibrational degrees of freedom. The reader should note that these forms for the unperturbed wavefunctions assume a strict separation of the different molecular degrees due to an adiabatic approximation.

Using eqn. (3.11) and eqns. (3.14a)-(3.14c), the transition matrix elements are,

$$\langle N|H_{\mathrm{int}}^{LG}|I\rangle = \sum_{\rho=\pm1} \sum_{l_1=0}^{|l|} C_{l_1} \langle v_n|\langle e| \left\{ \sum_{s=0}^{|l|-l_1} \begin{pmatrix} |l|-l_1 \\ s \end{pmatrix} \left(\sum_j Q_j \right)^s \right\} erY_1^{\rho}(\hat{r})|g\rangle|v_i\rangle, \qquad (3.15)$$

and,

$$\langle F|H_{\mathrm{int}}^{LG}|N\rangle = \sum_{\sigma=\pm1} \sum_{l_1=0}^{|l|} C_{l_1} \langle v_f|\langle g| \left\{ \sum_{s=0}^{|l|-l_1} \begin{pmatrix} |l|-l_1 \\ s \end{pmatrix} \left(\sum_j Q_j \right)^s \right\} erY_1^{\sigma}(\hat{r})|e\rangle|v_n\rangle. \qquad (3.16)$$

using the interaction Hamiltonian in eqn. (3.12). To simplify matters, we only examine the numerator of the left hand term in the brackets of eqn. (3.11). This numerator corresponds to the state tensor, $S_{\sigma\rho}$, for σ and ρ excitation and scattering polarizations states, respectively. Taking the product of these transition matrix elements to find the effective state tensor[10],

$$S_{\sigma\rho} = \langle F|H_{\text{int}}^{LG}|N\rangle_{\sigma}\langle N|H_{\text{int}}^{LG}|I\rangle_{\rho} =$$

$$\sum_{\sigma,\rho=\pm1}\langle v_f|\langle g|\varepsilon_{\sigma}\sum_{l_1=0}^{|l|} C_{l_1}\left\{\sum_{s=0}^{|l|-l_1}\begin{pmatrix} |l|-l_1 \\ s \end{pmatrix}\left(\sum_j Q_j\right)^s\right\} erY_1^{\sigma}(\hat{r})|e\rangle|v_n\rangle$$

$$\times\langle v_n|\langle e|\varepsilon_{\rho}\sum_{l_1=0}^{|l|} C_{l_1}\left\{\sum_{s=0}^{|l|-l_1}\begin{pmatrix} |l|-l_1 \\ s \end{pmatrix}\left(\sum_j Q_j\right)^s\right\} erY_1^{\rho}(\hat{r})|g\rangle|v_i\rangle. \qquad (3.17)$$

for a LG beam of arbitrary l-value. The state tensor can be further simplified defined with respect to linear polarizations. For linear polarization, the indices σ and ρ in eqn. (3.17) both equal zero, since linear polarization indicates the case in which there are zero quanta of angular momentum due to the beam's polarization. Therefore,

$$S_{\sigma\rho} = \langle F|H_{\text{int}}^{LG}|N\rangle_{\sigma}\langle N|H_{\text{int}}^{LG}|I\rangle_{\rho} =$$

$$\langle v_f|\langle g|\sum_{l_1=0}^{|l|} C_{l_1}\left\{\sum_{s=0}^{|l|-l_1}\begin{pmatrix} |l|-l_1 \\ s \end{pmatrix}\left(\sum_j Q_j\right)^s\right\} erE_0^{\sigma}|e\rangle|v_n\rangle$$

$$\times\langle v_n|\langle e|\sum_{l_1=0}^{|l|} C_{l_1}\left\{\sum_{s=0}^{|l|-l_1}\begin{pmatrix} |l|-l_1 \\ s \end{pmatrix}\left(\sum_j Q_j\right)^s\right\} erE_0^{\rho}|g\rangle|v_i\rangle. \qquad (3.18)$$

where σ and ρ now indicate the different linear polarizations of the incident and scattered photons and E_0 is the electric field amplitude in each case. This form of the state tensor makes use of a purely electronic dipole interaction with both the incident and scattered fields. This point is highlighted by writing eqn. (3.18) as

$$S_{\sigma\rho} = \langle F|H_{\text{int}}^{LG}|N\rangle_{\sigma}\langle N|H_{\text{int}}^{LG}|I\rangle_{\rho} = \langle g|erE_0^{\sigma}|e\rangle\langle e|erE_0^{\rho}|g\rangle$$

$$\times\langle v_f|\sum_{l_1=0}^{|l|} C_{l_1}\left\{\sum_{s=0}^{|l|-l_1}\begin{pmatrix} |l|-l_1 \\ s \end{pmatrix}\left(\sum_j Q_j\right)^s\right\}|v_n\rangle\langle v_n|\sum_{l_1=0}^{|l|} C_{l_1}\left\{\sum_{s=0}^{|l|-l_1}\begin{pmatrix} |l|-l_1 \\ s \end{pmatrix}\left(\sum_j Q_j\right)^s\right\}|v_i\rangle. \qquad (3.19)$$

The definition for the electronic transition dipole moment defined in eqn. (3.5) is used for the remainder of this discussion.

While much of this chapter will focus on how LG beams change the behavior of totally symmetric vibrations, excitation of non-totally vibrations is necessary in characterizing many biologically relevant molecules. Therefore, it is instructive to cast the effective state tensor in a form that allows for elucidation of changes to non-totally symmetric vibrations at a later time if experiments confirm the predicted changes in totally symmetric vibrations. To see how this interaction begins to look similar to the vibronic formalism introduced earlier, the electronic transition matrix elements in eqns. (3.18) and (3.19) are expanded to first order in the pertinent normal coordinates of the molecule. The state tensor becomes,

$$
\begin{aligned}
S_{\sigma\rho} = \sum_{j'} & \left\langle v_f \right| \sum_{l_1=0}^{|l|} C_{l_1} \sum_{s=0}^{|l|-l_1} \begin{pmatrix} |l|-l_1 \\ s \end{pmatrix} \left(\sum_j Q_j \right)^s \left| v_n \right\rangle \left\langle v_n \right| \sum_{l_1=0}^{|l|} C_{l_1} \sum_{s=0}^{|l|-l_1} \begin{pmatrix} |l|-l_1 \\ s \end{pmatrix} \left(\sum_j Q_j \right)^s \left| v_i \right\rangle M_{ge}^{\sigma}(0) M_{ge}^{\rho}(0) \\
& + \left\langle v_f \right| \sum_{l_1=0}^{|l|} C_{l_1} \sum_{s=0}^{|l|-l_1} \begin{pmatrix} |l|-l_1 \\ s \end{pmatrix} \left(\sum_j Q_j \right)^s \left| v_n \right\rangle \left\langle v_n \right| \sum_{l_1=0}^{|l|} C_{l_1} \sum_{s=0}^{|l|-l_1} \begin{pmatrix} |l|-l_1 \\ s \end{pmatrix} \left(\sum_j Q_j \right)^s Q_{j'} \left| v_i \right\rangle \left(\frac{\partial M_{ge}^{\sigma}}{\partial Q_{j'}} \right)_0 M_{ge}^{\rho}(0) \\
& + \left\langle v_f \right| \sum_{l_1=0}^{|l|} C_{l_1} \sum_{s=0}^{|l|-l_1} \begin{pmatrix} |l|-l_1 \\ s \end{pmatrix} \left(\sum_j Q_j \right)^s Q_{j'} \left| v_n \right\rangle \left\langle v_n \right| \sum_{l_1=0}^{|l|} C_{l_1} \sum_{s=0}^{|l|-l_1} \begin{pmatrix} |l|-l_1 \\ s \end{pmatrix} \left(\sum_j Q_j \right)^s \left| v_i \right\rangle \left(\frac{\partial M_{ge}^{\rho}}{\partial Q_{j'}} \right)_0 M_{ge}^{\sigma}(0). \qquad (3.20)
\end{aligned}
$$

The way the Franck-Condon and Herzberg-Teller terms change is more visible when eqn. (3.20) is explicitly evaluated for a p=0, l=1 LG beam. The state tensor becomes,

$$
\begin{aligned}
S_{\sigma\rho} = \sum_{j'} & \{ M_{GE}^{\sigma}(0) M_{GE}^{\rho}(0) [\left\langle v_f \middle| v_n \right\rangle \left\langle v_n \middle| v_i \right\rangle (C_1 + C_0)^2 + C_1 C_0 \left\langle v_f \right| \sum_j Q_j \left| v_n \right\rangle \left\langle v_n \middle| v_i \right\rangle + C_1 C_0 \left\langle v_f \middle| v_n \right\rangle \left\langle v_n \right| \sum_j Q_j \left| v_i \right\rangle + \\
& C_0^2 \left\langle v_f \right| \left(\sum_j Q_j \right) \left| v_n \right\rangle \left\langle v_n \right| \sum_j Q_{jj} \left| v_i \right\rangle] + \left(\frac{\partial M_{GE}^{\sigma}}{\partial Q_{j'}} \right)_0 M_{GE}^{\rho}(0) [(C_1 + C_0)^2 \left\langle v_f \middle| v_n \right\rangle \left\langle v_n \right| Q_{j'} \left| v_i \right\rangle + \\
& C_1 C_0 \left\langle v_f \right| \sum_j Q_j \left| v_n \right\rangle \left\langle v_n \right| Q_{j'} \left| v_i \right\rangle + C_1 C_0 \left\langle v_f \middle| v_n \right\rangle \left\langle v_n \right| \left(\sum_j Q_j \right) Q_{j'} \left| v_i \right\rangle + C_0^2 \left\langle v_f \right| \sum_j Q_j \left| v_n \right\rangle \left\langle v_n \right| \left(\sum_j Q_j \right) Q_{j'} \left| v_i \right\rangle] + \\
& \left(\frac{\partial M_{GE}^{\rho}}{\partial Q_{j'}} \right)_0 M_{GE}^{\sigma}(0) [(C_1 + C_0)^2 \left\langle v_f \right| Q_{j'} \left| v_n \right\rangle \left\langle v_n \middle| v_i \right\rangle + C_1 C_0 \left\langle v_f \right| \left(\sum_j Q_j \right) Q_{j'} \left| v_n \right\rangle \left\langle v_n \middle| v_i \right\rangle + \\
& C_1 C_0 \left\langle v_f \right| Q_{j'} \left| v_n \right\rangle \left\langle v_n \right| \sum_j Q_j \left| v_i \right\rangle + C_0^2 \left\langle v_f \right| \left(\sum_j Q_j \right) Q_{j'} \left| v_n \right\rangle \left\langle v_n \right| \sum_j Q_{jj} \left| v_i \right\rangle] \}. \qquad (3.21)
\end{aligned}
$$

The state tensor in eqn. (3.21) for a p=0, l=1 LG beam helps determine the selection rules allowing transitions between specific vibrational states. Selection rules are completely determined by the state tensor and the conservation of energy, both present in scattering transition probability. Therefore, to understand the spontaneous, resonantly enhanced scattering from a molecule, 'A' terms from eqn. (3.21) are inserted into eqn. (3.11) to produce,

$$
\frac{d^2 \sigma^{LG}}{d\Omega d\left(\hbar \omega_k^{'}\right)} = \left| \sum_{v_n} \frac{ M_{GE}^{\sigma}(0) M_{GE}^{\rho}(0) \left[\left\langle v_f \middle| v_n \right\rangle \left\langle v_n \middle| v_i \right\rangle (C_1 + C_0)^2 + C_1 C_0 \left\langle v_f \middle| v_n \right\rangle \left\langle v_n \right| \sum_j Q_j \left| v_i \right\rangle \right] }{ E_e + E_{v_n} - E_{v_i} - E_L - i\hbar \Gamma_0 } \right|^2
$$

$$
\times \delta\left(E_{v_f} - E_{v_i} + E_L - \hbar \omega_k^{'} \right) \qquad (3.22)
$$

The effective scattering probability in eqn. (3.22) for a p=0, l=1 LG beam is the main result of this chapter. It represents the inelastic scattering interaction of a LG beam with a molecule with a complex set of quantized vibrations. The ways in which the effective state tensor and the transition probability affect vibrational populations and coherences in resonance Raman scattering are discussed below.

Discussion

The form of eqn. (3.22) is important since it highlights a change in the effective scattering probability of the molecule due to the LG interaction Hamiltonian. Eqn. (3.22) should be compared with the Franck-Condon or Albrecht ‘A’ term of the scattering process of a plane wave. This term is similar to the ‘A’ term discussed above in that it does not depend on a derivative of the electronic transition dipole moment with respect to the normal coordinates of the molecule. As pointed out from eqns. (3.6) and (3.9), the ‘A’ term does not have contributions from the normal coordinates in the standard treatment of the interaction with the electric field of a plane wave. However, when a LG beam is used for scattering, the ‘A’ term of eqns. (3.21) and (3.22) do contain units of the normal coordinates of the molecule in the vibronic transition matrix elements. Embedded quanta of the molecule’s vibrations change how vibrational transitions are allowed and forbidden during the scattering process relative to the selection rules for a plane wave excitation.

The functional form of the effective scattering transition probability can be understood in a straightforward manner. The electronic dipole transition mediates a coupling between the transverse, radial variation of the LG electric field and the vibrational degrees of freedom of the molecule. This coupling results in a vibronic-like coupling between the electronic and nuclear degrees of freedom due explicitly to the radial variation of the electric field of the LG beam. This is evident in the formulation outlined above since the canonically transformed interaction Hamiltonian embeds the internal coordinates of the molecule in the field–molecule interaction itself when the incident field possesses a radially varying transverse profile.

When a plane wave excites the resonantly enhanced Raman scattering process, the ‘A’ term is dependent of the Franck-Condon vibrational overlaps in the excitation and emission processes. For this reason, only the totally symmetric vibrations of the molecules are the resonantly enhanced by the ‘A’ term of the molecular polarizability. When a LG beam is used to excite the electronic transition, however, the term that lacks a derivative with respect to the molecule’s vibrations is not only dependent the Franck-Condon overlaps. Therefore, using a LG beam to excite such an electronic dipole transition opens the door to new possibilities in vibronic selection rules governing Raman scattering.

There are two physical manifestations through which one measures the effects of an incident LG beam on Raman scattering process based upon the effective scattering transition probability in eqn. (3.22). Both physical manifestations produce changes in scattering spectra via changes in selection rules governed by parameters of the molecules. (i.e. displacement of the excited electronic state, symmetry of the molecule, Jahn-Teller distortions, etc.). First, by embedding units of vibrational quanta into the vibronic transition matrix elements, the LG beams changes the vibrational states that participate and their weight of participation in the scattering process. Highly lying intermediate states possess larger overlaps with vibrational overtones on the ground electronic state. Therefore, this mechanism modulates the vibrational populations that participate in the scattering process.

Second, as seen in eqns. (3.1), (3.11) and (3.22), scattering experiments necessitate the square of the molecular polarizability for prediction of measurable quantities. As seen in eqn. (3.22) scattering a LG beam off a molecule changes the weight of different terms in the effective scattering transition probability relative to the case of plane wave excitation. The LG beam modulates quantum mechanical pathways to specific vibrational final states that participate in the scattering process. More than one quantum pathway to the same final state leads to interference phenomena in the scattering process. Therefore, the LG modulates the interference present in the scattering process due to the additional terms introduced in the effective scattering transition probability, as seen in eqn. (3.22).

Interference phenomena have been observed in Raman scattering from molecules for several decades.[10-16] In the case of the incident LG beam, this interference phenomenon comes from amended vibronic transition matrix elements via a coupling between the transverse radial variation of the beam and the molecule’s vibrational degrees of freedom.

This mechanism modulates the vibrational coherences that participate in the scattering process.

To predict how an LG beam will change the resonantly enhanced Raman scattering spectrum of a molecule, changes in both the vibrational populations and coherences of totally symmetric are examined. First, the changes in the populations of different states and overtones of totally symmetric vibrations are examined. It is shown that the spectra of overtones for molecules highly displaced excited electronic states will show the largest changes due to LG excitation. Also, these effects are largest for vibrations with lower frequencies. Second, interference effects are examined and predictions for changes in 'baseline' spectra are proposed. It is shown that LG beams can control the 'natural' interference present in scattering process using plane wave excitation. This control comes from changes in the participating quantum pathways introduced by the LG excitation.

A simple model will help clarify predictions for changes in the vibrational populations and coherences in the resonance Raman scattering due to excitation by a LG beam. We use a molecule with one totally symmetric vibration and one non-totally symmetric vibration to elucidate these predictions. The sum over normal coordinates in eqn. (3.13) then becomes,

$$\sum_j Q_j = Q_1 + Q_2. \qquad (3.23)$$

where Q_1 is a totally symmetric vibration and Q_2 is a non-totally symmetric vibration. For 'A' term enhanced scattering, one simply focuses on Q_1 vibration since the Franck-Condon overlap is responsible for vibronic transitions involving this totally symmetric vibration.

In a spontaneous scattering experiment, the molecule can interact with a LG beam only via the excitation pathway. Such an experiment depends on the inherent coupling of the excited molecule to the vacuum field to cause the spontaneous emission of a photon. Since the LG basis set does not describe the vacuum field, there is no expectation that the transverse, radial variation of the electric field couples to the vibrational degrees of freedom during the electronic dipole emission transition. In order to get contributions from the other pathways in eqn. (3.20), a stimulated or coherent Raman scattering experimental setup with two LG beams must be used.

To identify changes in the molecular polarizability and, therefore, scattering transition probability that will lead to observable differences in a measured resonance Raman spectrum, we make comparisons between the state tensor in the case of a l=0 excitation beam to that of a l=1 excitation beam. This comparison also takes into consideration the fact that a vibrational quantum is only embedded into the excitation transition matrix element. Eqn. (3.21) then becomes

$$S_{\sigma\rho}^{A} = M_{GE}^{\sigma}(0) M_{GE}^{\rho}(0) \langle v_f^1 | v_n^1 \rangle \langle v_n^1 | v_i^1 \rangle \langle v_f^2 | v_n^2 \rangle \langle v_n^2 | v_i^2 \rangle \qquad l = 0, \tag{3.24a}$$

$$\begin{aligned} S_{\sigma\rho}^{A} &= M_{GE}^{\sigma}(0) M_{GE}^{\rho}(0) \\ &\times \Big[\langle v_f^1 | v_n^1 \rangle \langle v_n^1 | v_i^1 \rangle \langle v_f^2 | v_n^2 \rangle \langle v_n^2 | v_i^2 \rangle + D \langle v_f^1 | v_n^1 \rangle \langle v_n^1 | Q_1 | v_i^1 \rangle \langle v_f^2 | v_n^2 \rangle \langle v_n^2 | v_i^2 \rangle \Big] \quad l = 1. \end{aligned} \tag{3.24b}$$

for plane wave (l=0) and LG beam (l=1) excitation. The subscripts i, n, and f denote the initial, intermediate and final vibrational states participating in the scattering process and the superscripts denote the symmetry of the normal coordinate tied to that transition matrix element as defined in eqn. (3.23). That is, the superscript 1 is the totally symmetric coordinate Q_2 and the superscript 2 is the non-totally symmetric coordinate Q_2. The coefficients for each term in the state tensor have been normalized to the coefficient of the first term in eqn. (3.24b) for the sake of simplicity. The coefficient D is related to the l-dependent pre-factor in the interaction Hamiltonian shown in eqn. (3.10). It is weighted by the inverse of the waist of the incident beam. The role of D in determining the physics predicted here is discussed below.

It is clear that whereas there is only one term that contributes to the state tensor for the case of a l=0 excitation beam, a l=1 LG beam introduces a new term into the state tensor that now contributes to the scattering process. In the case of a l=0 LG incident beam, there is a finite set of intermediate states that contribute to the scattering process. The size of this set of states is determined by the amount of displacement between the ground and excited electronic states. For smaller displacements, only a small set of intermediate states will contribute non-zero Franck-Condon overlaps. A larger displacement increases the number of intermediate states whose Franck-Condon overlaps is large enough in magnitude to make sizable contribution to the scattering process.

However, at any level of displacement the l=1 LG beams embeds a quantum of the totally symmetric normal coordinate in the vibrational transition matrix elements in eqn. (3.24b). This embedded vibrational quantum results in a new, second term in the state tensor that changes how states participate in the scattering process. Instead of the molecule being entirely dependent on the value of the Franck-Condon overlap to determine which intermediates contribute, the excitation beam itself can set the value of the vibrational overlaps and change the nature of the scattering process fundamentally.

Using the simple two vibrational model for comparison of the scattering in the cases of l=0 and l=1 excitation beams, we make predictions for changes in the vibrational populations and coherences participating in the scattering process. First, by introducing a vibrational quantum of the totally symmetric coordinate Q_1 into the transition matrix element, the second term of eqn. (3.24b) changes the selection rules for the excitation of intermediate states. Thus, this term in eqn. (3.24b) means that different states are excited on the excited electronic manifold of vibrational states when a LG beam is used. By exciting states that are not typically participating in the scattering process with plane wave excitation, the LG beam changes which final states will be populated at the end of the process.

This conclusion is seen more clearly using concrete vibrational states. Assume that only the ground and first excited vibrational states of the excited electronic manifold play a role in the inelastic scattering process excited by a plane wave. This means that the final state of the scattering process is either the first or second vibrationally excited state on the ground electronic state, or

$$|F_1\rangle = |g\rangle|1\rangle, \qquad (3.25a)$$

$$|F_2\rangle = |g\rangle|2\rangle. \qquad (3.25b)$$

For some molecules, the excited electronic is displaced from the equilibrium geometry of the ground state by a very small amount. While small displacements results in non-zero overlaps and allow ‘A’ term enhancement in resonance Raman scattering, the overlap between the vibrational ground states on each respective electronic manifold dominate the selection rules for allowed vibrational transitions. In that case given l=0 excitation, the sum over the state tensor becomes,

$$\sum_n S^A_{\sigma\rho} = M^{\sigma}_{ge}(0)M^{\rho}_{ge}(0)\left[\langle 1|0\rangle\langle 0|0\rangle + \langle 1|1\rangle\langle 1|0\rangle + \langle 2|1\rangle\langle 1|0\rangle\right] \qquad l=0. \qquad (3.26)$$

Only two intermediate states on the excited electronic manifold, the ground and first excited vibrational states, contribute to determining the population of the final state. It is also clear that the amount of population reaching this final state depends only on the Franck-Condon overlaps between the participating vibrational states. The spectrum produced by this excitation beam (l=0) will be known as the ‘baseline’ spectrum.

As described above, for the case of a minimally displaced excited electronic state, the first and second terms in the brackets of eqn. (3.26) dominate the selection rules. The vibrational overlaps participating in each pathway to the final state are comparable in magnitude, a fact that leads to interesting effects in the discussion below. For small displacements, the third term is often neglected since it rare to see this overtone due to small value of both of its Franck-Condon overlaps.

In the case of l=1 excitation, the roles of the intermediate states are reversed. The sum over the state tensor becomes,

$$\begin{aligned}\sum_n S^A_{\sigma\rho} = M^{\sigma}_{ge}(0)M^{\rho}_{ge}(0)[&\langle 1|0\rangle\langle 0|0\rangle + \langle 1|1\rangle\langle 1|0\rangle + \langle 2|1\rangle\langle 1|0\rangle \\ &+ D\langle 1|0\rangle\langle 0|Q_1|0\rangle + D\langle 1|1\rangle\langle 1|Q_1|0\rangle + D\langle 2|1\rangle\langle 1|Q_1|0\rangle] \qquad l=1. \qquad (3.27)\end{aligned}$$

Now the dominant vibrational overlap is between the ground and first excited vibrational states of the ground and excited electronic states, respectively. This change is due to the presence of the vibrational quantum embedded in the transition matrix by the l=1 LG beam. Since the first excited vibrational state now plays a larger role as an intermediate state due to this increased vibrational overlap, a significantly larger population reaches the second final state, denoted in eqn. (3.25b). The difference in final states is seen in FIG. 3.1.

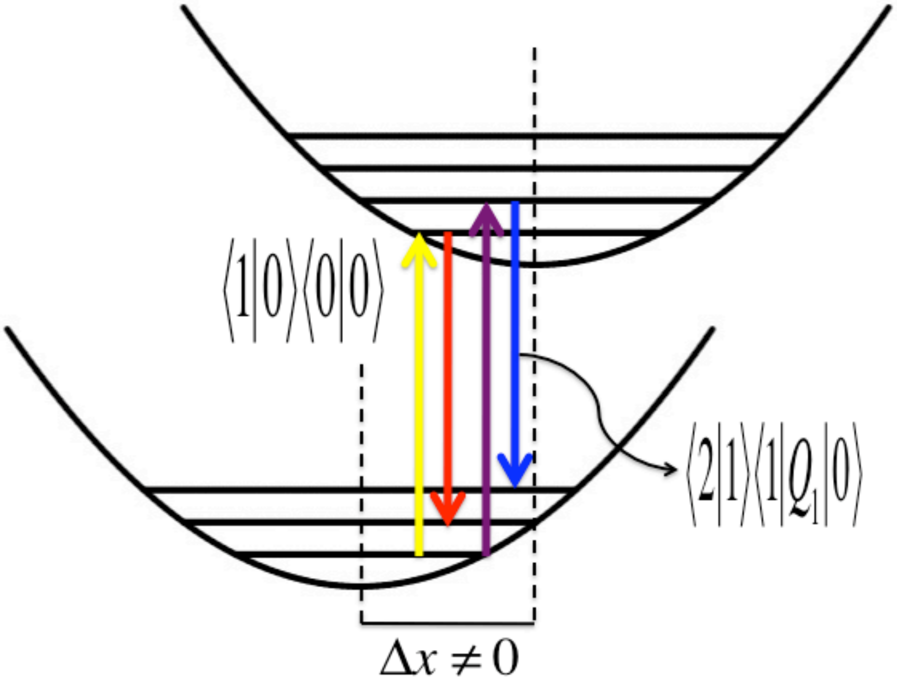

FIG. 3.1. Two physical processes implied by the first and sixth terms of eqn. (3.27). While the scattering process on the left is determined by the Franck-Condon overlap, the selection rules for the scattering process on the right are changed by the LG excitation beam via an embedded quantum the molecule's normal coordinate in the transition matrix element.

For a molecule possessing an excited minimally displaced from the ground state, enough population could reach this alternative final state that a new peak appears in the resonance Raman scattering spectrum. If this overtone appears, it would represent a new peak in the 'baseline' spectrum described above. Depending of the frequency of the vibration of interest, this mechanism will necessitate tuning the frequency of the excitation laser. This happens because the resonance of the two vibronic transitions will differ due to the difference in the vibrational intermediate state. Larger vibrational frequencies will need larger laser detuning, while smaller frequencies need smaller detunings from the 0-0 transition resonant frequency.

In contrast, many small, diatomic molecules show very large displacements of their excited electronic states with respect to the ground state equilibrium structure. This large displacement leads to large Franck-Condon factors between the ground vibrational state of the ground electronic state and highly excited vibrational states of the excited electronic state. Since the potential energy surfaces of molecules are inherently anharmonic, highly excited vibrational states are also more closely spaced together. Therefore, many overtones of the single, totally symmetric vibration of diatomic molecules are observed in their resonance Raman spectra.

In analogy to the case of a small displacement, LG beam excitation affects the 'baseline' spectrum of molecules characterized by highly displacement excited electronic states. In most similarity with the above discussion, a LG beam will introduce a new, higher order overtone to the resonance Raman spectrum of a diatomic molecule not present in the 'baseline' spectrum. Since the LG beam also affects the vibrational overlaps by embedding quanta of the normal coordinate, the relative intensities of the overtone peaks in the 'baseline' spectrum should also be modulated. This modulation could appear as a shifting of the intensity to lower or higher order overtones depending on the excitation frequency, the displacement of the excited electronic state and the spacings of the vibrational states in both the ground and excited electronic states.

As described above, the Raman scattering of a LG beam from a molecule also leads to changes in the ways that vibrational coherences participate in the scattering process. In order to appreciate these changes, the fundamental excitations of the resonantly enhanced scattering from a totally symmetric vibration of a molecule with a small excited electronic state displacement is investigated. Excitation with a l=0 laser mode is compared to that of a l=1 LG beam.

One on the one hand, the interaction with a fundamental, l=0 laser beam, excites a specific set of quantum pathways that lead to the final state in eqn. (3.25a). These pathways are completely dependent on the Franck-Condon overlaps in the left hand set of vibrational transition matrix elements in eqn. (3.22). On the other hand, the right hand set of vibrational transition matrix elements from eqn. (3.22) show that a l=1 LG beam amends the weight with which these intermediate states contribute to the scattering process. Changing the set of intermediate states leads to changes to the quantum mechanical pathways in the scattering process. These changes modulate interference effects taking place.

For the case of a molecule with a minimally displaced excited electronic state, the molecular polarizability for each type of excitation beams becomes,

$$\alpha_{\sigma\rho}^{A} \propto M_{ge}^{\sigma}(0) M_{ge}^{\rho}(0) \frac{C_0^2}{\hbar} \left[\frac{\langle 1|0\rangle\langle 0|0\rangle}{\Delta + i\Gamma_0} + \frac{\langle 1|1\rangle\langle 1|0\rangle}{(\nu - \Delta) + i\Gamma_0} \right] \quad l = 0, \tag{3.28a}$$

$$\alpha_{\sigma\rho}^{A} \propto M_{ge}^{\sigma}(0) M_{ge}^{\rho}(0) \frac{(C_0 + C_1)^2}{\hbar} \left[\frac{\langle 1|0\rangle\langle 0|0\rangle}{\Delta + i\Gamma_0} + \frac{D\langle 1|0\rangle\langle 0|Q_1|0\rangle}{\Delta + i\Gamma_0} + \frac{\langle 1|1\rangle\langle 1|0\rangle}{(\nu - \Delta) + i\Gamma_0} + \frac{D\langle 1|1\rangle\langle 1|Q_1|0\rangle}{(\nu - \Delta) + i\Gamma_0} \right] \quad l = 1. \tag{3.28b}$$

where energy of the Q_1 is denoted by ν in the denominator, Δ is the detuning from the electronic transition and Γ_0 is the linewidth of the electronic transition, respectively.[3] The states of the non-totally symmetric vibration Q_2 make no contribution to this process due to strict selection rules governing its transitions.

Taking into consideration the explicit value of the vibrational overlaps for a small displacement and the complex denominators in eqn. (3.28a), the two terms make quantitatively similar contributions to the scattering process. This was also the case in considering population behavior and leads to interference that affects the scattering transition probability, the 'natural' interference. However, when a l=1 LG beam is scattered off this molecule, the fourth term has a large value for the vibrational overlap due to the embedded vibrational quantum of Q_1. The embedded quantum of the vibration now changes the weights of the connections between different states relative to plane wave excitation. These changes allow for modulation of the 'natural' interference present in the plane wave case. The difference in the two pathways in eqn. (3.28b) is shown in FIG. 3.2.

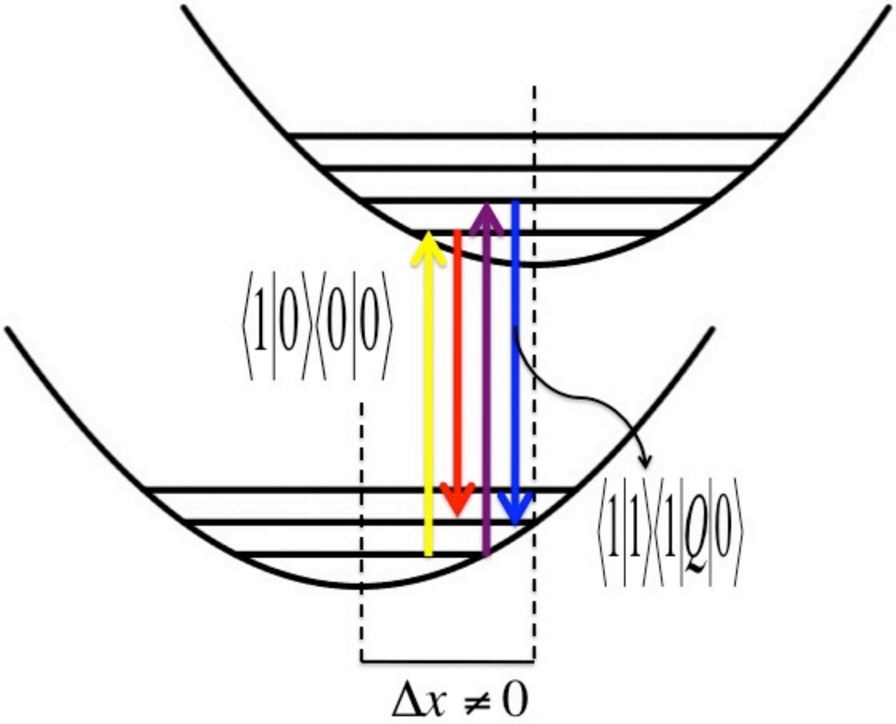

FIG. 3.2. Schematic showing different quantum pathways and state tensors for vibrational population in LG pumped spontaneous resonance Raman scattering due to A-term enhancement for a model totally symmetric vibration.

The excitation of the electronic dipole transition with a LG beam now changes the weighting of different quantum pathways for the population of the first excited vibrational state on the ground electronic potential of this totally symmetric vibration. Interference between these pathways plays a role in modulating the intensity of the peaks measured in a spontaneous resonance Raman experiment using a LG beam relative to the 'baseline' spectrum.

The necessary phase relationships between the quantum pathways to observe interference are set by the complex energy denominators of the contributing terms in eqn. (3.28b). If the terms share the same sign, there will be constructive interference and the intensity of the peak corresponding to Q_1 increases in the measured Raman spectrum. When the two terms have opposite signs, the quantum pathways deconstructively interfere and the intensity of the Q_1 peak decreases.

Specific terms in the complex energy denominators of eqns. (3.28a) and eqn. (3.28b) play a role in determining the sign of the interference caused by the incident LG beam. The molecule fixes the energies of the electronic and intermediate states as well as the lifetime of the intermediate states. However, the researcher controls both the energy of the laser and the frequency of the vibration of interest. Specific laser detunings and vibrational frequencies change the sign and magnitude of this interference effect. FIGs. 3.3 and 3.4 show the detuning dependence of this interference effect for vibrational frequencies of 1500 cm^{-1} and 500 cm^{-1}, respectively. Changing the laser detuning and vibrational frequency of interest modulates the scattering transition probability as well as the differential scattering cross-section.

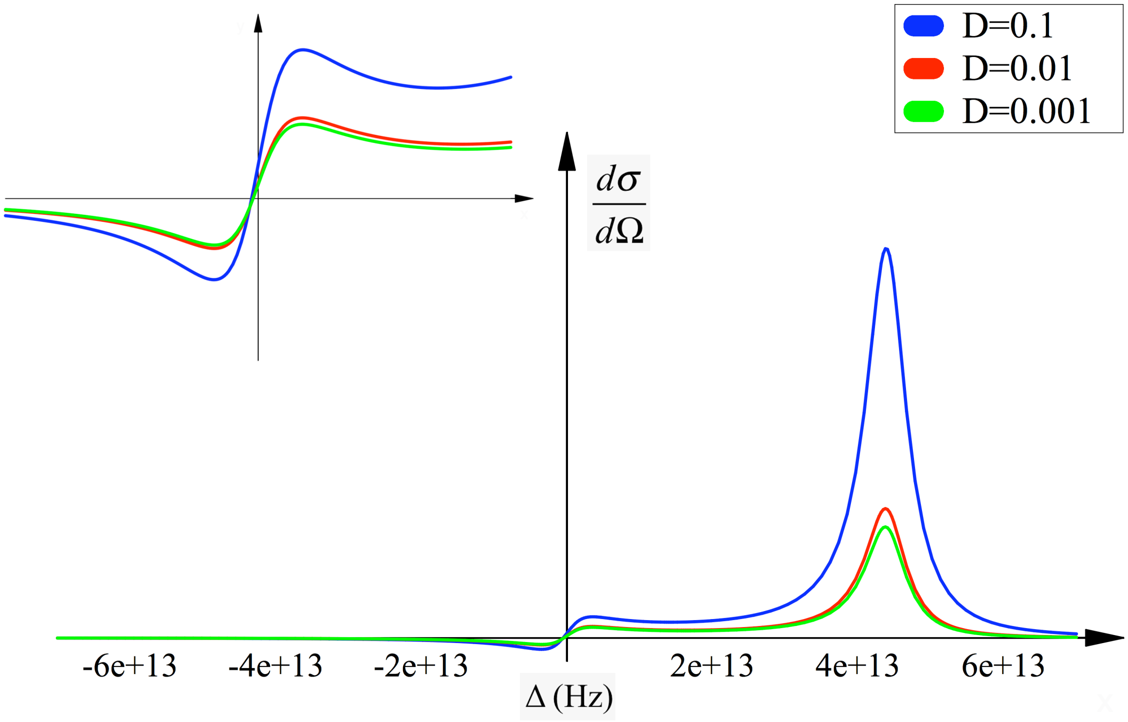

FIG.3.4 Magnitude of contribution of second and fourth terms in eqn. (3.28b) to the differential scattering cross-section as a function of laser detuning (Δ) for a 1500 cm^{-1} vibration and a linewidth (Γ_0) of 3.4 THz for three values of the coefficient D: D=0.1 (blue), D=0.01 (red), and D=0.001 (green). The inset shows an enlarged view of the region of negative laser detuning where the magnitude of the interference contribution becomes negative.

That is, FIG.s 3.3 and 3.4 show a plot of the equation,

$$\frac{d\sigma^{\text{interference}}}{d\Omega} \propto \frac{\left|\langle 1|1\rangle\right|\left|\langle 1|0\rangle + D\langle 1|Q_1|0\rangle\right|^2}{(\nu-\Delta)^2+\Gamma_0^2}$$

$$+2\langle 1|0\rangle\langle 0|0\rangle\langle 1|1\rangle\left\{\langle 1|0\rangle + D\langle 1|Q_1|0\rangle\right\}\frac{\left[\Gamma_0^2+(\nu-\Delta)\Delta\right]}{\left[\Gamma_0^2-(\nu-\Delta)\Delta\right]^2+(\nu-2\Delta)^2\Gamma_0^2}. \qquad (3.29)$$

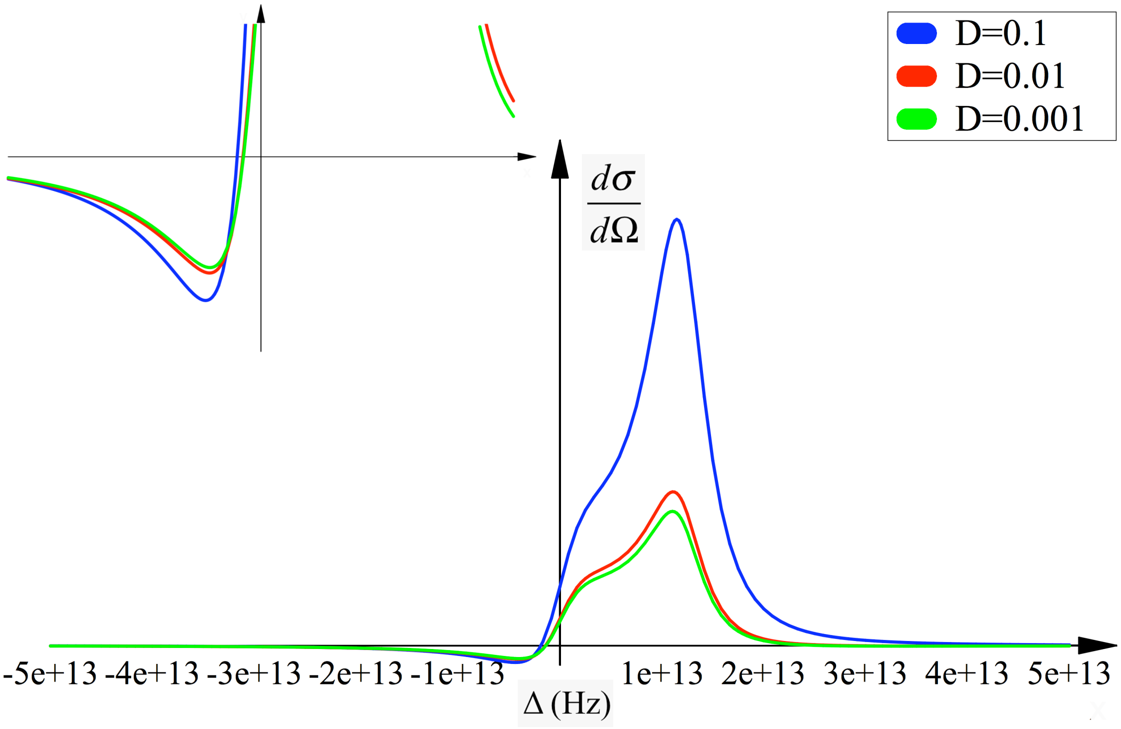

FIG. 3.4. Magnitude of the contribution of second and fourth terms in eqn. (3.28b) to the differential scattering cross-section as a function of laser detuning (Δ) for a 500 cm^{-1} vibration and a linewidth (Γ_0) of 3.4 THz for three values of the coefficient D: D=0.1 (blue), D=0.01 (red), and D=0.001 (green). The inset shows an enlarged view of the region of negative laser detuning where the magnitude of the interference contribution becomes negative.

FIG.s 3.4 and 3.4 highlight several important aspects of this interference effect. First, the overall magnitude of this effect is sensitive to the frequency of the vibration of interest. While not shown explicitly on the scale in either figure, inspection of eqn. (3.29) shows that the peak of this effect near the vibronic resonance laser detuning is not dependent on the frequency of the vibration of interest. However, the second term of eqn. (3.29) is functionally dependent on the frequency of the vibration of interest. As this frequency becomes smaller, so does the denominator of the second term resulting in a larger contribution to the scattering process.

This physically corresponds to the quantum mechanical pathway through the first excited vibrational intermediate state taking intensity from the pathway through the vibrational ground intermediate state. This intensity sharing is dependent on the linewidth of the electronic resonance. Γ_0 must be comparable with the vibrational frequency such that the two different resonant quantum pathways occur within the same absorption feature. This becomes more likely for lower frequency vibrations. When both vibronic resonances occur within the linewidth of the electronic absorption, these transitions should show larger susceptibility to control via the inelastic scattering of LG beams.

Second, the laser detuning at which the interference effect becomes most negative is dependent on the frequency of the vibration of interest. This behavior comes from the change in the frequency of the resonant vibronic transition. For different vibrational frequencies, the vibronic resonance shifts, causing the interference between different vibronic resonances to shift in the spectrum as well. Shifts in the interference due to changes in the vibronic resonance frequency then shift the minimum of the detuning profile of this effect.

Third, the position and magnitude of the minimum of the detuning profiles can depend on both the frequency of the vibration of interest and the value of D. In the case of the 1500 cm^{-1} vibration, this minimum shows a small shift to less negative laser detuning as the value of D is reduced. However, this shift is more pronounced in the case of the 500 cm^{-1} vibration. This minimum also decreases in magnitude as the value of D is reduced, likely reaching its 'natural' value when D=0.001.

Finally, FIGs. 3.3 and 3.4 both show a dramatic dependence on the value of D. Therefore the modulation of the interference effect by the LG beam is highly sensitive to the value of D. As D becomes smaller, eqn. (3.29) is dominated by the interference terms due to the 'natural' contribution of the first excited vibrational intermediate state. That is, the contribution from this intermediate state that is present with plane excitation. The dominance of this 'natural' contribution is visible in the lack of significant difference between the red and green detuning profiles for both vibrational frequencies.

Physically, the value of D is a dominated by the ratio of the characteristic length scale of the molecule (~0.01 nm to 1 nm) to the waist of the incident LG beam, w_0. Based on the above calculations, optimal values of D allowing detection of the predicted effects in the resonance Raman scattering from a single molecule range from 0.01 to 0.1. However, two parameters of experimental considerations limit D to much smaller values.

First, resonantly enhanced Raman scattering from molecules necessitates an electronic transition. The vast majority of molecules show electronic transitions in region between 260 nm and 1000 nm. Therefore, diffraction limit does not allow beams that excited electronic transitions in molecules to be focused to spots smaller than 100 nm to 500 nm. For an extremely large molecular absorption cross-section characterized by a radius of 1 nm, the value of D would not be larger than 0.01. Second, the radial variation of the transverse profile of the LG beam comes out of the paraxial approximation in which diffractive effects are neglected. The paraxial approximation limits the use of high numerical aperture optics in focusing LG beams to small spot sizes while preserving the functional radial variation of the electric field used in developing the predicts made in this chapter.

While these considerations may seem to dominate the physics predicted here, Chapter 2 showed that since the transverse radial variation of the incident LG beam is the same throughout the beam. With that understanding, many orders of magnitude of the molecules will show the behavior derived here. Therefore, even for small values of D the resonance Raman spectra measured in the lab will show effects associated with the coupling of the radial variation of the electric field of a LG beam to the quantized, totally symmetric vibrations of the molecule irradiated by the beam.

Non-totally symmetric vibrations are usually enhanced in a resonance Raman measurement due to the breakdown of the molecule’s symmetry. This occurs in response to electronic and nuclear degrees of freedom of the molecule no longer being rigorously separated, as in an adiabatic approximation. The ‘B’ term accounts for these dynamics, as discussed earlier. While non-totally symmetric vibrations were not rigorously investigated in this chapter, given the treatment of totally symmetric vibrations it seems that similar effects will be seen in non-totally symmetric vibrations.

The full derivation of the effects of an incident LG beam on the behavior of non-totally symmetric vibrations is left for a later time. If experiments confirm the effects predicted above for totally symmetric vibrations, a full treatment of non-totally symmetric vibrations is necessary. Such a treatment would be very useful in understanding how a LG is used to control different invariants of the molecular polarizability, especially the anti-symmetric invariant. This type of control is useful in more fully elucidating the behavior and dynamics of several biologically relevant molecules.

Conclusions

This chapter developed the resonance Raman scattering of a LG beam from the totally symmetric vibrations of molecules. The coupling between the transverse radial variation of the LG beam and vibrations of the molecule embeds unit of vibrational quanta in the vibronic transition matrix elements used to calculate the scattering transition probability. For totally symmetric vibrations, embedded units of vibrational quanta affect the behavior of both vibrational populations and coherences contributing to the scattering process.

For the case of a molecule characterized by an electronic excited state minimally displaced from the ground state equilibrium geometry, the embedded unit of vibrational quanta from a p=0, l=1 LG beam allows more sizable amounts of populations to reach overtones states of the vibration of interest. This occurs because the vibrational quantum amends the value of the vibrational overlaps between different states on the two relevant electronic states. Sizable population reaching higher excited vibrational intermediate states results in the appearance of new peaks in the ‘baseline’ spectra of molecules characterized by this type of electronic structure.

For diatomic molecules with large electronic excited state displacements, the embedded vibrational quantum not only produces new peaks in ‘baseline’ spectra, but also redistributes populations into the already excited overtone peaks. This population redistribution affects the relative intensity of the overtone peaks. Changes in the relative intensities of these peaks will depend on specific parameters of the molecule of interest including the magnitude of the excited state displacement, the anharmonicity of the excited state potential energy surface and vibrational frequency of the single, totally symmetric vibration.

For the case of a molecule characterized by an electronic excited state minimally displaced from the ground state equilibrium geometry, the incident LG beams changes the weighting of different vibrational coherences participating in the scattering process. Changes in the weighting of different quantum pathways modulate the interference effects affecting the behavior of the differential Raman scattering cross-section of the 'baseline' spectra. This modulation is dependent on the laser detuning from the resonant electronic transition, the frequency of the vibration of interest and magnitude of the coefficient D.

As a function of laser detuning this interference effect shows both positive and negative peaks. The position and magnitude of these peaks depend on the vibrational frequency and magnitude of D. For higher vibrational frequencies, the maximum of the detuning profile appears farther from zero detuning, due to larger energy vibronic resonance. However, the peak of the interference effect scales inversely with the magnitude of the vibrational frequency due to intensity stealing in the case of comparable vibrational frequencies and electronic transition linewidths. The position of the negative peak of the interference peak shows the same dependence. For higher frequency vibrations the peak appears farther from zero detuning than lower frequency vibrations. This behavior is due to the difference in the vibronic resonance for different vibrational frequencies.

As D decreases, the overall magnitude of this interference modulation effect diminishes dramatically. Since D is related to the ratio of the characteristic length scale of the molecule to the waist of the LG beam, large values of D are hard to produce in the visible regime where many molecular electronic resonances occur. Coupled with the nature of the paraxial approximation, detection of the predicted effects will be difficult. Detection of these effects depends on the ability of molecules to couple to the transverse profile of the incident electric field throughout the entire profile of the LG beam. Detection of the effects predicted in this chapter is undertaken in Chapter 6 of this work.

References

1. A. Alexandrescu, D. Cojoc and E. Di Fabrizio, Phys. Rev. Lett. **96** (24) (2006).
2. M. van Veenendaal and I. McNulty, Phys. Rev. Lett. **98** (15) (2007).
3. J. L. McHale, *Molecular spectroscopy*. (Prentice Hall, 1999).
4. J. J. Sakurai, *Advanced Quantum Mechanics*. (Pearson Education, Inc., 2006).
5. G. Fischer, *Vibronic coupling: the interaction between the electronic and nuclear motions*. (Academic Press, London ; Orlando, Fla., 1984).
6. C. Cohen-Tannoudji, J. Dupont-Roc and G. Grynberg, *Photons and atoms: introduction to quantum electrodynamics*. (Wiley, New York, 1989).
7. D. P. Craig and T. Thirunamachandran, *Molecular quantum electrodynamics: an introduction to radiation-molecule interactions*. (Academic Press, London ; Orlando, 1984).
8. S. Mukamel, *Principles of nonlinear optical spectroscopy*. (Oxford University Press, New York, 1995).
9. E. A. Power, *Introductory quantum electrodynamics*. (American Elsevier Pub. Co., New York, 1965).
10. S. Hassing and O. Sonnich-Mortensen, Chemical Physics Letters **47** (1), 115-118 (1977).
11. J. Friedman and R. M. Hochstrasser, Chemical Physics Letters **32** (3), 414-419 (1975).
12. P. Hildebrandt, M. Tsuboi and T. G. Spiro, Journal of Physical Chemistry **94** (6), 2274-2279 (1990).
13. R. E. Holt and T. M. Cotton, Journal of the American Chemical Society **109** (6), 1841-1845 (1987).
14. P. P. Kircheva and S. D. Simonov, Journal of Raman Spectroscopy **17** (4), 363-367 (1986).
15. T. G. Spiro and P. Stein, Annu. Rev. Phys. Chem. **28**, 501-521 (1977).
16. M. R. Wedlock, E. Jensen, L. J. Butler and K. F. Freed, Journal of Physical Chemistry **95** (21), 8096-8103 (1991).

Chapter 4:
Condensed Phase Ultrafast Transient Dynamics of Fe$^{(III)}$TPPCl

Introduction

The optical properties of synthetic and natural metalloporphyrins have been extensively studied for over 50 years. Their optical and electronic properties have found use in applications ranging from light harvesting and energy conversion to medical therapeutics to molecular electronics. As a model example of a high-spin, five-coordinate Fe$^{(III)}$ species, iron (III) tetraphenylporphyrin chloride has been studied using a variety of spectroscopic techniques. However, time-domain optical spectroscopy measurements of this system's excited state dynamics in condensed phase have been few and far between.

Early time-domain measurements of the excited state dynamics of Fe$^{(III)}$TPPCl in condensed phase provided researchers with enough information to propose a simple, two-level model.[1, 2] The first state was given a ~100 fs lifetime based on considering the structure of the excited state absorption (ESA), but could not be spectrally resolved with >1 ps pulses. The second state was labeled triplet of the porphyrin ring and assigned a lifetime on the order of 10's of ps.

A more recent study of the gas phase time dynamics of several different MTPPs and metallo-octaethylporphyrins (MOEPs) provides an order of magnitude higher time resolution. [3] From gas phase photoelectron and ion mapping, another two-state, transient decay model of Fe$^{(III)}$OEPCl is proposed. The states in this model, however, are associated with charge transfer (CT) processes occurring between the central metal atom and porphyrin ring rather than only on the porphyrin. The faster time scale (50 fs) being associated with a ring-to-metal excited CT state and retrodonation from the metal to the ring leading to a (d,d*) excited state localized on the metal center that decays in less than 5 ps. This CT model is based on the fact that distinctly different dynamics are observed in ZnTPP. The authors claim that this difference comes from the fact that Zn has completely filled *d*-orbitals, which cannot participate in similar CT processes. The authors of this study note that peripheral substitution (phenyl vs. ethyl in this case) had little effect on the magnitude of the measured lifetimes in gas phase, differentiating the gas phase Fe-centered systems from condensed phase Zn-centered systems dissolved in toluene.[4]

The models proposed in previous studies of $Fe^{(III)}$TPPCl are based upon the four-orbital scheme of the porphyrin electronic states first developed by Goutermann.[5] In this scheme two nearly degenerate highest occupied molecular orbitals (HOMO's) of a_{1u} and a_{2u} symmetry, respectively, and a degenerate pair of lowest unoccupied molecular orbitals (LUMO's) of e_{1u} symmetry give rise to four electronic transitions. The strongly allowed electronic transitions are associated with near ultraviolet (UV) to high-energy visible absorption denoted as the Soret or B resonance. The weak or forbidden transitions are designated as the Q transitions.

A recent study using modern calculations, UV-vis and magnetic circular dichroism (MCD) spectroscopies proposes that the electronic structure of $Fe^{(III)}$TPPCl is significantly more complex than the more simple four-state Goutermann model. FIG 4.1 shows the absorption spectrum of this molecule along with assignment of different transitions based on this more recent study.

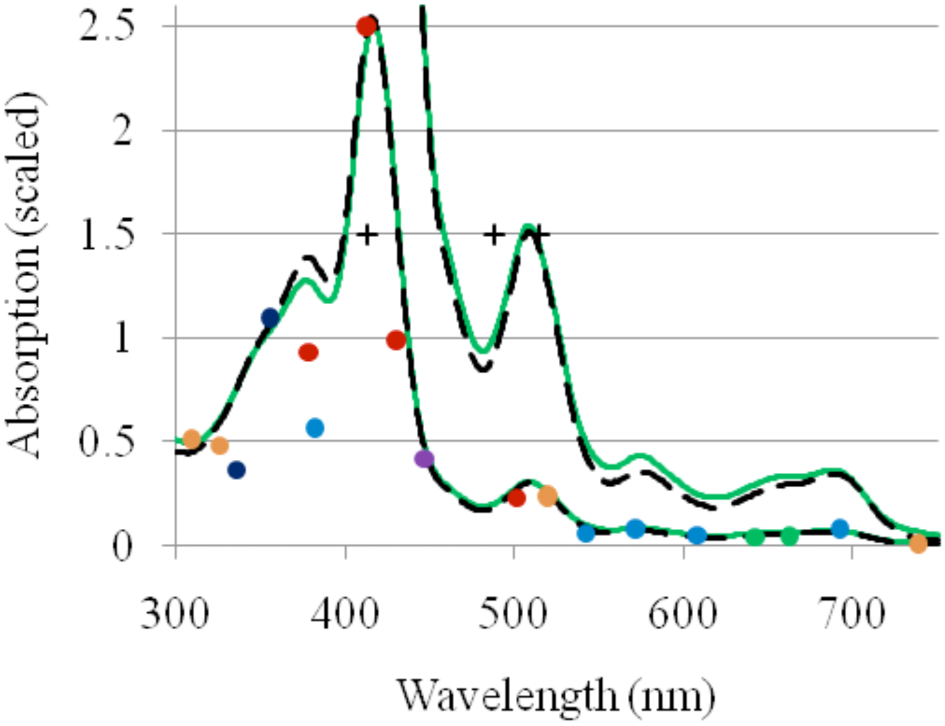

FIG. 4.1. The room temperature absorption spectrum of $Fe^{(III)}TPPCl$ in CH_2Cl_2 (black dashed line) and a mixture of toluene and CH_2Cl_2 (green solid line). The three crosses represent the three excitation wavelengths used in resonance Raman measurements reported here (413 nm, 488.0 nm, 514.5 nm). The color-coded circles represent the assignments from Paulat and Lehnert. The peaks indicated by blue circles are predominantly out-of-plane polarized charge transfer transitions. The very weak transitions indicated by green circles are in-plane transitions involving charge transfer and ππ* character. The peak indicated with purple is an in-plane and out-of-plane polarized mixture of charge transfer and ππ* character. The bands indicated in red are in-plane polarized ππ* states arising primarily from the HOMO-LUMO transitions of Goutermann's four state model. The peaks indicated by dark blue circles are higher in-plane polarized ππ* transitions. The peaks indicated in orange are not well assigned.

This complexity also reflects itself in the enhancement of specific vibrations in rR spectrum. The resonance Raman spectroscopy of $Fe^{(III)}TPPCl$ is consistent with the above assignments. Excitation at 514.5 nm in resonance with the Q_v transition results in a spectrum characterized by enhancement of the anomalously polarized non-totally symmetric vibrations of a_{2g} symmetry, and other non-totally symmetric modes of b_{1g} and b_{2g} symmetry.[6, 7] The observed bands provide insight into the nature of the vibronic coupling/Jahn-Teller distortions necessary to produce intensity in the electronic transition. Excitation on the red-edge of the Soret band at 454.5 nm gives rise to a Raman spectrum dominated by intensity in totally symmetric vibrations characteristic of A-term excitation in resonance with an allowed electronic transition.[7]

The results of this study have yet to be applied to transient dynamics of the excited states of $Fe^{(III)}$TPPCl. An especially important possibility from this recent study is the role of out-of-plane ligand-to-metal charge transfer (LMCT) states from the axially-ligated Cl atom in the ultrafast excited state dynamics.

The excited state electronic and vibrational properties physiologically important heme-proteins have been extensively studied using a variety of ultrafast, spectroscopic techniques as well. As molecules closely related to the $Fe^{(III)}$TPPCl, the time decay dynamics of iron heme centers in hemoglobin (Hb), myoglobin (Mb) and Cytochrome c (Cyt c) have been characterized by several research groups down to resolution below 50 fs.[8-19] While there are obvious structural similarities between these systems, it has yet to be determined if these natural heme systems can serve as pertinent dynamical models for synthetic iron-centered porphyrins.

The studies of excited state dynamics of iron-centered heme proteins share similar observations. First, hemes centered with both the $Fe^{(II)}$ and $Fe^{(III)}$ show sub-ps internal conversion to the ground electronic state when excited on both the Soret and Q resonances. This conversion is slightly faster in the $Fe^{(II)}$-centered Mb and Cyt c systems then in $Fe^{(III)}$-centered Cyt c. Second, longer-lived transients (τ>1ps) of these systems correspond to vibrational relaxation processes on the ground electronic state. Narrowing and shifting of transient difference spectra measured on these time scales has been used to reach this conclusion. Third, many biologically relevant heme proteins display excitation frequency and chemical-dependent photolysis of axial ligands. This bond breaking process depends on both the type of ligand in the axial position and the wavelength of the incident laser pulse.

With a more complete understanding of the electronic structure of this system and modern technology, we have undertaken the measurement of the transient excited state dynamics of $Fe^{(III)}TPPCl$ in three solvent environments at room temperature (toluene, dichloromethane (DCM) and a 1:1 mixture of toluene and DCM) as well as the mixture environment at low temperature. The results reported here for the temperature, solvent and frequency-dependent excited state dynamics of $Fe^{(III)}TPPCl$ are contrast with those of heme proteins. This five-coordinate iron porphyrin halide shows a sequential electronic relaxation. The longest-lived excited electronic state relaxes on time scales longer than 10 ps at room temperature and longer than 500 ps at low temperature. Vibrational relaxation largely occurs on the excited electronic states participating in the sequential relaxation process. There are no indications of vibrational relaxation after the electronic relaxation displaying the longest lifetime. Also, there is no evidence from our measurements that axial photolysis plays a role in the excited state dynamics.

As a model system for both high-spin, five-coordinate metalloporphyrins and physiologically relevant heme centers, the ultrafast dynamics of $Fe^{(III)}TPPCl$ provide essential insights into the use of porphyrins in a range of important applications.

Experimental Methods

Temperature dependent transient absorption (TA) experiments were taken on two different laser systems. Low temperature broadband TA was taken using 790 nm output of a home-built Ti:Saph ultrafast oscillator kit (Kapteyn-Murnane Labs Inc.). The high repetition rate output of the oscillator was amplified with the standard 1 kHz Chirped Pulse Amplification technique using a homemade multipass Ti:Saph amplifier, compressed in time, and split into pump and probe arms. The pump arm was frequency-doubled to ~400 nm to excite the sample on the Soret resonance. The probe arm path was lengthened by specific amounts with a precision mechanical delay stage to set specific time delays between the arrivals of the pump and probe, respectively. Before reaching the sample, the probe focused into a 5 mm thick piece of CaF_2 creating a broadband white light source. This allowed for broadband spectral measurement of probe transmission changes of the sample in response to the excitation of the pump.

Pump-probe concentrations of the samples were designed to produce an optical density of between 0.5 and 1 at the pump wavelength and were placed in a capped static spectrophotometric cell. They were cooled using a custom-built Teflon reservoir filled with liquid N_2. Cooling occurred via conduction due to contact with the reservoir. The sample was routinely cooled to -185° C, or 88 K measured using a thermocouple. In order to reduce condensation of water vapor on the sample cell and optics, the sample and reservoir were enclosed in a Plexiglas box purged with Dri-rite filtered N_2 gas. Room temperature measurements were also taken to test the reproducibility of this setup.

Due difficulties in the low temperature TA measurements, difference spectra were measured at specific pump-probe time delays. As the measurement went on, evidence appeared of the build up of photoproduct in the measured difference spectrum. The amount of averaging necessary to produce large enough signal to noise ratio (SNR) precluded our ability to measure a typical trace of the full transient dynamics of the system over the time delays made available by the length of our delay stage. Between collected difference spectra, the sample cell was moved vertically to ensure that the pump and probe were overlapped in a fresh part of the sample. This worked to help prevent the depletion of the molecule's ground state in any specific portion of the sample while the measurement was taken. Also, the difference spectrum measured for time delays before the arrival of the pump was subtracted from every other difference spectrum to correct for the formation of long-lived photoproduct in the sample.

Room temperature TA measurements exciting the vibronic overtone of the Q resonance were also taken with this same ultrafast system. The compressed output of the multipass amplifier was split into two arms with a 70/30 beamsplitter and the more powerful arm was used to pump a noncolinear optical parametric amplifier (NOPA). The weaker arm was used to pump the CaF_2 crystal to produce a broadband continuum probe in same fashion as the low temperature measurements. The NOPA was optimized to output pulses centered near 520 nm with an autocorrelation of ~200 fs. The autocorrelation was measured using phase-matched two-beam, Type-II second harmonic generation in a 100 um think crystal of BBO and OceanOptics USB2000 silicon diodearray spectrometer. The sample was flowed through a 1 mm path-length cell at a high enough rate to ensure that each pulse interrogated a fresh portion of the sample and reduced photo-damage. These measurements were done in a wider range of solvents, not being restricted by the constraint of glass formation. Sample concentrations were made to match those used in the low temperature Soret excited measurements.

Room temperature TA experiments exciting on the Soret transition near 400 nm were also undertaken using the combination 1 kHz regenerative and multipass amplified 790 nm output of a similar, but distinct Ti:Saph oscillator. Probe and pump arms were created in the same fashion as described above. A broadband white light probe was also made in CaF_2 and used for determining changes in probe transmission in response to the pump excitation of the sample.

Experimental Results

Ultrafast time resolved spectroscopy has been used to investigate the photochemical pathways in metal porphyrins for over thirty years.[1-4, 10-16, 18-39] Very little work however, has been reported for $Fe^{(III)}$TPPCl. A very early study following excitation at 353 nm indicated ultrafast ground state recovery coupled with the formation of a triplet state population with ca. 3% efficiency. [1] This study, however, does not address the wavelength, solvent, or temperature dependence reported here. We therefore set out to measure the transient absorption spectrum of $Fe^{(III)}$TPPCl as a function of solvent, temperature, and excitation wavelength.

A. Low temperature difference spectra

The polycrystalline nature of the sample in neat DCM introduced scatter and precluded the measurement of the transient absorption spectrum in neat CH_2Cl_2 at 88K. In contrast, a nice glass formed with the 1:1 mixture of toluene and DCM and allowed measurement of both the steady state and transient absorption spectra of this sample in a transmission geometry. Transient absorption spectra were obtained for $Fe^{(III)}$TPPCl in a 1:1 mixture of toluene and DCM at 88K and room temperature. As stated above, set time delays were used, with the probe coming before the pump and with the probe coming 0.7 to 0.75 fs, 50 ps, or 500 ps after the pump. The steady state absorption and transient difference spectra obtained in are summarized in FIG. 4.2. The low temperature difference spectra have been smoothed using a 5 nm FWHM Gaussian to reduce pixel-to-pixel noise in the spectra.

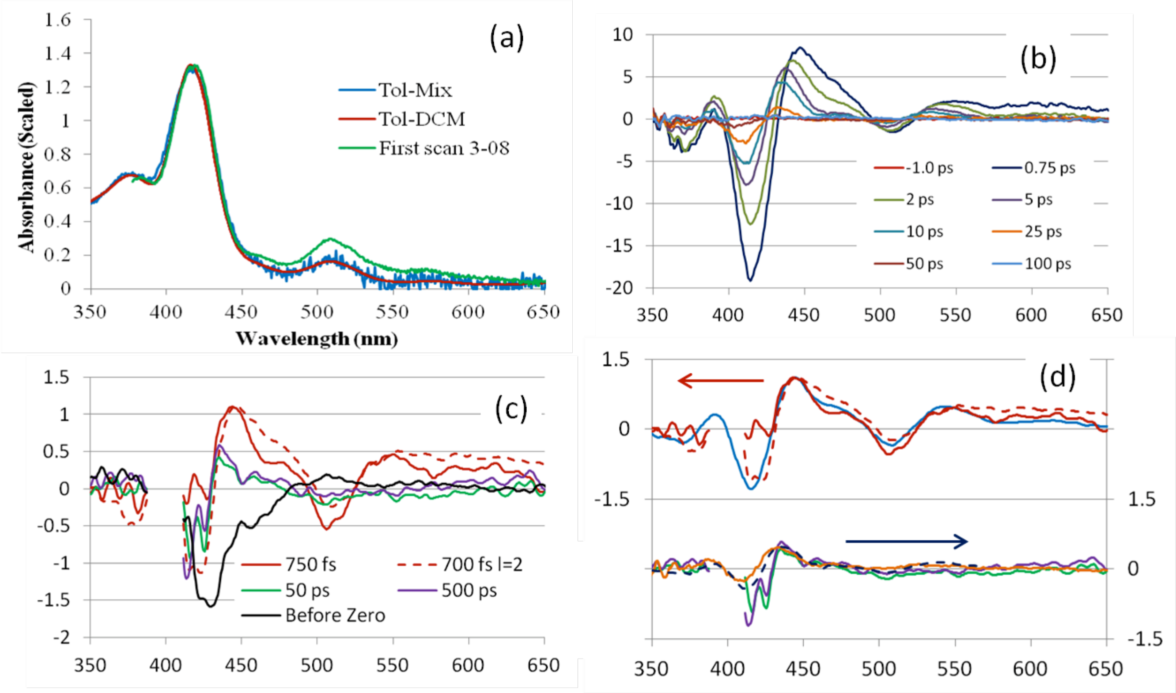

FIG. 4.2. (a) Absorption spectra of Fe$^{(III)}$TPPCl obtained for room temperature solution using a standard UV-vis spectrophotometer (red) and a femtosecond white-light continuum (blue) compared with the spectrum obtained at 88K using a femtosecond white-light continuum. (b) Room Temperature difference spectra obtained following excitation of Fe$^{(III)}$TPPCl in 1:1 mixture of toluene and DCM with a 400 nm pump pulse. (c) Difference spectra of Fe$^{(III)}$TPPCl in 1:1 mixture of toluene and DCM at 88K following excitation with a 400 nm pulse. The trace labeled "Before Zero" (black) represents the difference spectrum for formation of a photoproduct with a lifetime ≥ 1 ms. The traces plotted at positive time delay have been corrected for the long-time residual difference observed before zero and represent the difference spectrum caused by the excitation pulse immediately prior to the probe. (d) Comparison of the difference spectrum obtained at room temperature and at 88K. The low temperature difference spectra in two measurements at 750 fs and 700 fs (red) are compared to room temperature solution (light blue) in the upper traces. The room temperature spectrum was obtained using the same apparatus as used for the low temperature measurements and has been scaled to match the intensity of the 88K trace. There is a chirp to the continuum, which distorts the precise time delay at each wavelength, but the chirp is the same for all three spectra plotted. The lower traces show a comparison of the difference spectra obtained at 50 ps and 500 ps in the low temperature glass with the 25 ps spectrum obtained in room temperature solution. Again the room temperature spectrum has been scaled to match the

intensity of the low temperature spectrum. The black dashed line is the species associated difference spectrum of the longest lived species in solution (vide infra).

The room temperature spectra are consistent with the previously reported data. The excited state decays back to ground state with no perceptible signal after 50 ps. The behavior of the transient difference spectrum at 88K is similar to the behavior in room temperature solution. The spectra obtained at 750 fs are essentially identical at 88K and at room temperature. The species responsible for this spectrum decays on a ps time scale forming a longer-lived excited state. This longer-lived state decays on a time scale of ca. 16 ps in room temperature solution (see below) but persists for more than 500 ps at 88K.

Of more immediate significance to the resonance Raman measurements reported above, the transient difference spectra obtained for $Fe^{(III)}$TPPCl at 88K when the probe pulse is nominally before the excitation pulse, demonstrates the accumulation of a photoproduct with a lifetime > 1 ms. It is likely that this difference spectrum corresponds to the photoproduct observed in the Raman spectra (vide infra). There is a small increase in intensity in the region of the Q_v band at 507 nm and a significant bleaching in the region to the red of the Soret band.

B. Transient dynamics in room temperature solution.

In order to better understand the excited state dynamics in $Fe^{(III)}$TPPCl a transient absorption study of the excited state dynamics in the room temperature solution was performed. Transient absorption spectra were obtained for $Fe^{(III)}$TPPCl in dichloromethane, toluene, and a 1:1 mixture of dichloromethane and toluene. Pump wavelengths of 400 nm and 520 nm were used to excite the sample. Typical traces obtained with magic angle polarization are shown in FIG. 4.3 for the data obtained in a 1:1 mixture of dichloromethane and toluene. The data for the neat solvents is similar. For high pulse energies, above 1.5 uJ/pulse, a long-lived absorption persists across the visible region of the spectrum. When the pump intensity is decreased this long-lived signal disappears and the difference spectrum decays to baseline within a few 10's of picoseconds. Under linear excitation of the one-photon allowed states of $Fe^{(III)}$TPPCl no long-lived photoproduct is observed.

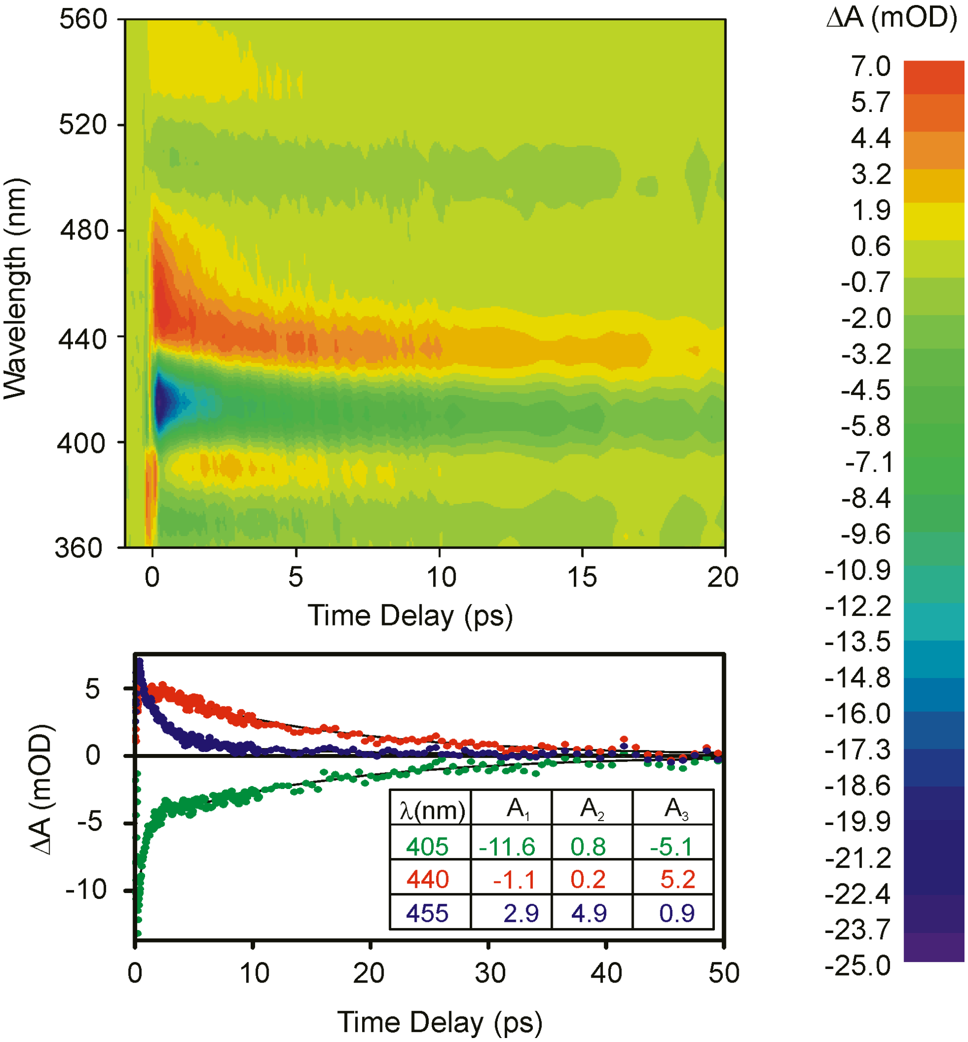

λ(nm)	A_1	A_2	A_3
405	-11.6	0.8	-5.1
440	-1.1	0.2	5.2
455	2.9	4.9	0.9

FIG. 4.3. Transient absorption spectrum obtained for $Fe^{(III)}TPPCl$ in a 1:1 mixture of dichloromethane and toluene following excitation at 400 nm. The line-outs at three specific wavelengths in the lower panel are compared with fits to a model consisting of three exponential decay components, τ_1 = 0.5 ps, τ_2 = 2.1 ps, and τ_3 = 15.6 ps. The amplitudes for these three components are given in the FIG..

The transient absorption data was analyzed by using a 5 nm Gaussian smoothing function to reduce the pixel to pixel noise in the spectra and selecting line-outs every 5 nm from 365 nm to 600 nm. These traces were fitted to a model consisting of three exponential decay components using a global analysis program described elsewhere. Removing one component from the analysis resulted in a clearly inferior fit while adding a fourth decay component did not result in a well defined time constant or a significant improvement in the fit. We cannot, however, rule out the presence of an additional decay component <0.25 ps. It is possible that the 0.5 ps component identified here does not reflect the initial internal conversion of the state excited at 400 nm. The minimum of three required decay components is illustrated clearly in the traces plotted in FIG. 4.3. The decay associated difference spectra (DADS) corresponding to these three components are shown in the left hand column of FIG. 4.4.

The influence of solvent on the decay of Fe$^{(III)}$TPPCl at room temperature is minor, reflected primarily in the time constant for the long component. The decay is fastest in toluene at 13.2 ps and slowest in DCM at 18.5 ps, with the decay in the 1:1 mixture falling between these two extremes. The spectrum, however, is unaffected by the solvent. Similar difference spectra are observed for the longer two components following excitation at 520 nm in the Q_v band (see FIG. 4.5).

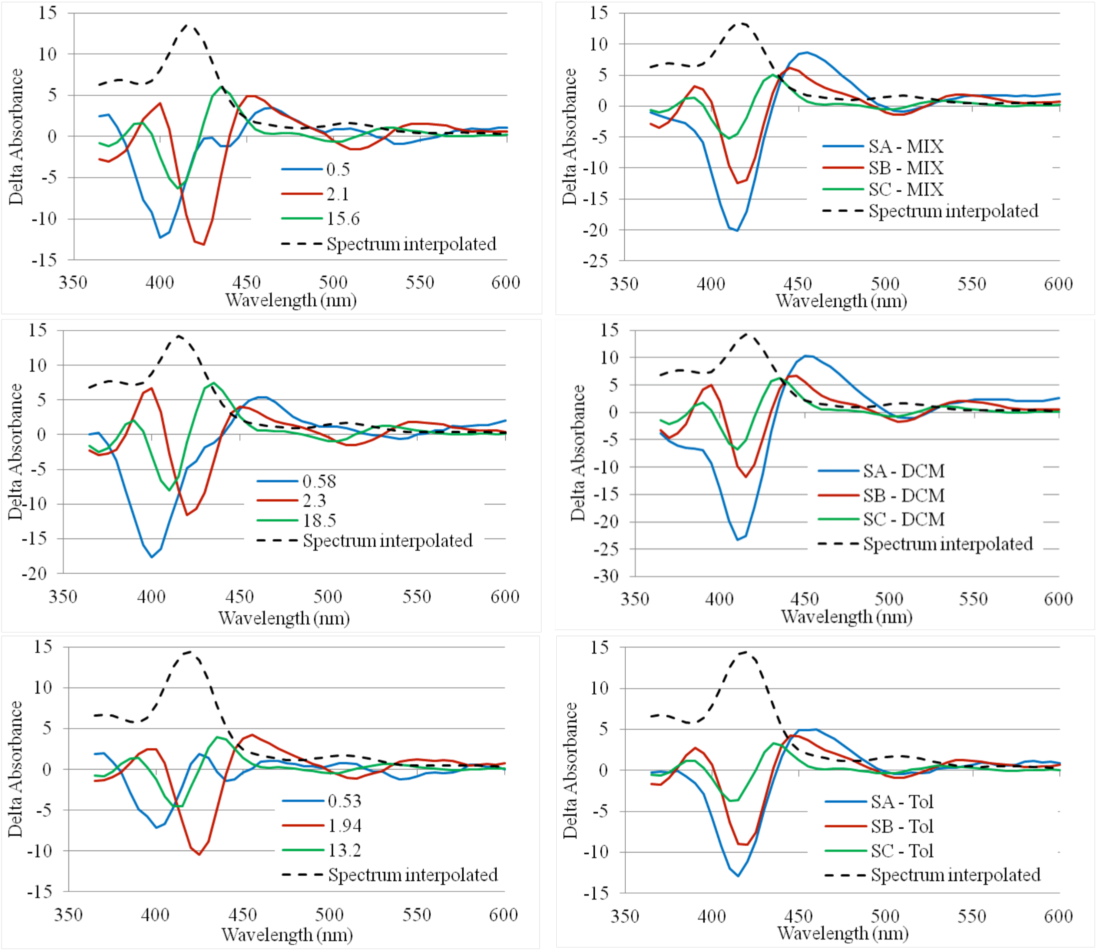

FIG. 4.4. Decay associated difference spectra (DADS, left) and species associated difference spectra (SADS, right) for Fe$^{(III)}$TPPCl in a 1:1 mixture of toluene and DCM (top), DCM (middle) and toluene (bottom) observed with 400 nm pump excitation.

Table 4.I. Decay constants (ps) obtained from the global analysis of transient absorption signal following photoexcitation of Fe$^{(III)}$TPPCl in room temperature solution.

	400 nm excitation			520 nm excitation		
	τ_1 (ps)	τ_2 (ps)	τ_3 (ps)	τ_1 (ps)	τ_2 (ps)	τ_3 (ps)
Toluene	0.53	1.94	13.2	0.42	1.7	13.4
1:1 mixture	0.5	2.1	15.6	0.5	2.2	14.3
DCM	0.58	2.3	18.5	0.4	1.8	17.4

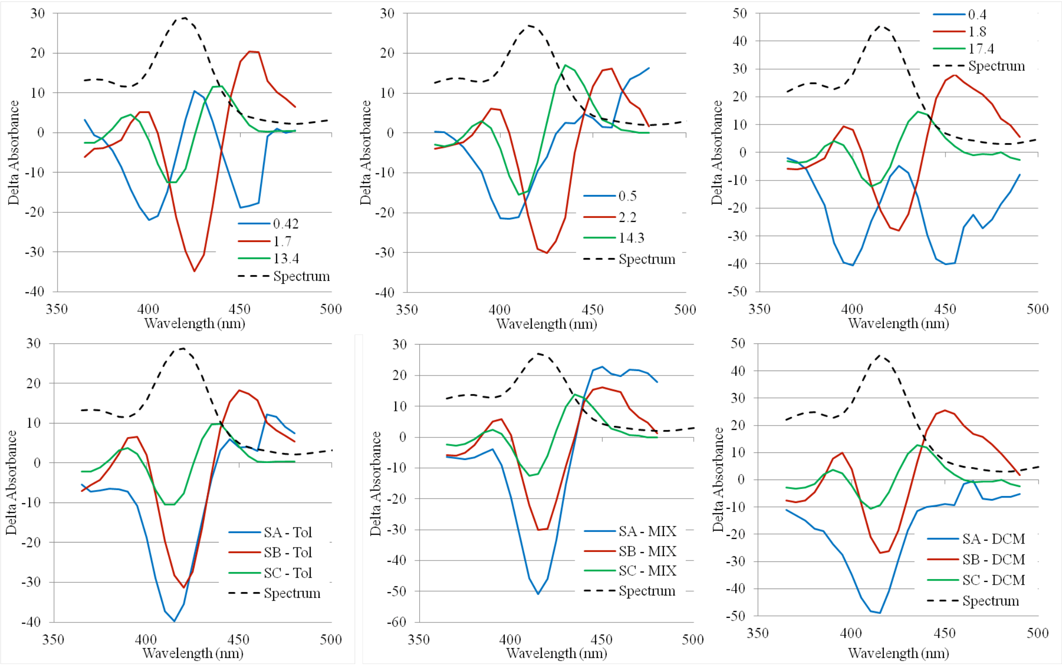

FIG. 4.5. Decay associated difference spectra (DADS, top) and species associated difference spectra (SADS, bottom) following excitation of Fe$^{(III)}$TPPCl at 520 nm in toluene (left), a 1:1 mixture of toluene and dichloromethane (middle) and dichloromethane (right).

Given a model accounting for the three decay components, the decay associated spectra plotted in FIGs. 4.4 and 4.5 can be used to estimate species associated difference spectra. The simplest model capable of accounting for the transient absorption data obtained following excitation of Fe$^{(III)}$TPPCl is a simple sequential decay A→B→C→ground state. The initial species, A, decays on a time scale of ca. 0.4-0.6 ps to form B, which decays on a 1.7-2.3 ps time scale to form C. The final excited state C decays back to the ground state.

$$\mathrm{S_A}(\lambda) = \mathrm{I_1}(\lambda) + \mathrm{I_2}(\lambda) + \mathrm{I_3}(\lambda), \qquad (4.1a)$$

$$S_B(\lambda) = I_2(\lambda)\frac{k_1 - k_2}{k_1} + I_3(\lambda)\frac{k_1 - k_3}{k_1}, \qquad (4.1b)$$

$$S_C(\lambda) = I_3(\lambda)\frac{(k_1 - k_3)(k_2 - k_3)}{k_1 k_2}. \qquad (4.1c)$$

The SADS corresponding state C is independent of solvent and excitation wavelength. The SADS corresponding to state B has at most a slight dependence on solvent or excitation wavelength. $S_B(\lambda)$ may exhibit a slight difference in the relative magnitudes of the positive peaks at 390 nm and 450 nm and the bleach at 415 nm. The general features are identical for all three solvents and both excitation wavelengths. SADS corresponding to state A show the largest dependence on excitation wavelength. This is not unexpected, and may reflect the initial population of different excited states at 400 nm and 520 nm. In addition, it is possible that there is another fast internal conversion component <0.25 ps following excitation at 400 nm. The state designated A here, is then the state populated by this internal conversion.

Discussion

The excited state electronic and vibrational properties of porphyrins, metalloporphyrins and physiologically important heme-proteins have been extensively studied using a variety of ultrafast, spectroscopic techniques.[1-4, 9-12, 14-16, 18, 21-24, 26-67] As molecules closely related to the $\mathrm{Fe^{(III)}TPPCl}$, the time decay dynamics of iron heme centers in hemoglobin, myoglobin and cytochrome c have been characterized by several research groups down to resolution below 50 fs.[8-19] While there are obvious structural similarities between these systems, it has yet to be seen if these natural heme systems can serve as pertinent dynamical models for synthetic iron-centered porphyrins. One of the dominant process driving biological heme dynamics is ligand dissociation and recombination, the role of which is not clearly understood in the case of the dynamics of $Fe^{(III)}$TPPCl.

Ultrafast TA has been measured for free-base tetraphenylporphyrin (H_2TPP) and a number of metallotetraphenylporphyrins (MTPP) in condensed phase.[3, 4, 9, 13, 24, 25, 33, 43, 51, 54, 60, 62] Without the central metal present, free-base tetraphenylporphyrin (H_2TPP) shows ground state recovery on ms time scales.[54] This long time scale as compared to $Fe^{(III)}$TPPCl is assigned to the efficiency of intersystem-crossing (ISC) from the lowest excited singlet state, assigned S_1 in the literature, to the lowest triplet state of the porphyrin macro cycle and the inability of this state to internally convert to the ground state. Dynamics initiated in H_2TPP by Soret excitation (397 nm) first occur in the sub-ps domain, however. The initially excited state is given an upper limit of 10 fs using the Strickler-Berg equation and estimated fluorescence quantum yield from steady-state fluorescence measurements, as has been done elsewhere.[68] Zewail and co-workers also use time-dependent fluorescence measurements to give the state populated by Soret excitation an upper bound of ~50 fs. In addition, the authors use the fact that they observe the same qualitative changes in absorption of single-color probes for both Soret and Q excitation to deduce that the same states must be populated within the resolution of their measurement, relegating the lifetime of the initially populated below their pulse length (~96 fs).[54]

Zewail and co-workers also investigated the Soret-excited ultrafast transient dynamics of the four-coordinate ZnTPP.[33] In contrast to other transition metalloporphyrins, Zn has a completely filled *d*-shell atomic orbital's. The fluorescence from the state initially excited on the Soret resonance has been reported for almost 40 years in this model metalloporphyrin. While H_2TPP shows more complex ultrafast TA dynamics upon Soret excitation at 397 nm, the four-coordinate ZnTPP only shows two decay components whose lifetime is shorter than 1 ns. The faster of these two is nearly two orders of magnitude larger than that observed in H_2TPP (~1.5 ps in benzene). Clearly the presence of the d^{10} configured central metal atom stabilizes the initially excited state.

This is also seen in the fact that the fluorescence yield from the S_2 is much more easily measured than in H_2TPP.[33, 54]

These authors' reports of >1 ps lifetime of the initially excited state using the second harmonic of Ti:Saph output have been confirmed by other researchers.[4] Further studies showed that the impulsive excitation of the S_n state with sub-50 fs pulses results in the formation of a coherent vibrational wavepacket. Based on the lifetime of the initially excited state, a stimulated Raman process creating vibrational coherences on the ground state was proposed. Resonance Raman measurements confirm that this wavepacket exists on the ground state and persist with lifetimes varying from a few to several hundred fs and is dependent on the chirp of the pump pulse. The explicit chirp-dependence is also an indication of a ground state wavepacket.

From these studies two major conclusions are drawn. First, the ultrafast decay dynamics of the TPP itself are complex and range in time scales from 10's of fs to 10's of ps. Second, the presence of a centrally coordinated metal atom can stabilize the TPP excited state initially populated on the Soret transition as well as other excited electronic states. These two pieces of information are useful in understanding the dynamics of higher-coordinated MTPP featuring metal atoms with unfilled *d*-orbitals.

Early time-domain measurements of the excited state dynamics of $Fe^{(III)}$TPPCl in condensed phase provided researchers with enough information to propose a simple, two-level model.[1, 2] The first state was given a ~100 fs lifetime based on considering the structure of the excited state absorption (ESA), but could not be spectrally resolved with >1 ps pulses. The second state was labeled triplet of the porphyrin ring and assigned a lifetime on the order of 10's of ps.

A more recent study of the gas phase time dynamics of several different MTPPs and metallo-octaethylporphyrins (MOEPs) provides an order of magnitude higher time resolution. [3] From gas phase photoelectron and ion mapping, another two-state model transient decay model of $Fe^{(III)}$OEPCl is proposed. The states in this model, however, are associated with charge transfer (CT) processes occurring between the central metal atom and porphyrin ring rather than only on the porphyrin. The faster time scale (50 fs) being associated with a ring-to-metal excited CT state and retrodonation from the metal to the ring leading a (d,d*) excited state localized on the metal center that decays in less than 5 ps in $Fe^{(III)}$OEPCl. This conclusion is based on the fact that distinctly different dynamics are observed in ZnTPP. The authors claim that this difference comes from the fact that Zn has a completely filled *d*-orbital, which cannot participate in similar CT processes. The authors of this study note that peripheral substitution (phenyl vs. ethyl in this case) had little effect on the magnitude of the measured lifetimes in gas phase, differentiating the gas phase Fe-centered systems from condensed phase Zn-centered systems dissolved in toluene.[4]

The model proposed in each of these studies is based upon the four-orbital scheme of the porphyrin electronic states first developed by Goutermann, as described in the Introduction of this chapter. The more recent study providing insight into a more complex electronic structure of $Fe^{(III)}$TPPCl than the simpler four-state Goutermann model has yet to be applied to transient dynamics of the excited states of $Fe^{(III)}$TPPCl. An especially important possibility from this more recent study is the role of out-of-plane ligand-to-metal charge transfer (LMCT) states from the axially-ligated Cl atom in the ultrafast excited state dynamics. As we shall see, the complexity of this molecule's electronic structure will be paramount in photochemistry and excited states probed via rR spectroscopy.

Holten and co-workers were the first to systematically investigate the TA dynamics of several different transition metalloporphyrins.[21, 23, 26-28, 36, 38, 65, 66, 69, 70] Through several studies, broadband difference spectrum of porphyrins containing transition metals of differing coordination, oxidation state and spin state were measured and examined. Unfortunately, the most modern technology for such measurements only allowed time resolution on the level of 10's of ps.

Important information was nevertheless uncovered. Many of the excited states investigated exhibit difference spectra similar to the DADS displayed in FIGs. 14 and 15 above. There is a strong bleach of the ground state Q and Q_v transitions in the region between 500 and 600 nm for many systems. A strong increase in absorption is also seen in the region between 420 and 480 nm. The flashes used for ps TA measurements in these studies, however, could not usually reach the bleach of the Soret band near 400 nm. This is a dominant feature in DADS and SADS excited at both the 400 nm and 520 nm pumping frequencies in FIGs. 4.4 and 4.5.

Many of Holten's studies observed transients that were assigned to states not initially excited by the pump flash. The lifetimes of these initial states were then given an upper limit of the flash width, usually between 10 and 40 ps. Longer-lived species corresponding in most cases to different coordination and oxidation states of the central metal atom were easily identified and assigned based on static UV-vis spectra and the reconstruction of the excited absorption spectra (ESA).

Since the pioneering studies of Holten and co-workers, several studies have examined the ultrafast (sub-ps) decay of natural iron-centered heme proteins.[8, 10-13, 15-18, 20, 29, 32, 71] In a study similarly investigating broadband ultrafast TA, Hochstrasser and co-workers attributed all of the electronic dynamics in deoxy myoglobin (Mb) containing a reduced central $Fe^{(II)}$ atom to a sub-100 fs lifetime when excited at 405 nm.[8] The observed difference spectra start out red-shifted, but narrow and blue-shift as the probe delay increases, causing the zero-crossing to the red of the Soret bleach to blue-shift in time as well. It was proposed that these dynamics are the signature of a 'hot' electronic ground state. Two longer-lived states were assigned to initial dephasing and then subsequent cooling of 'hot' ground state vibrations. After dephasing, energy is transferred to vibrations of the porphyrin ring that were not excited during the Soret transition as well as to the protein environment of Mb. This conclusion was partly based upon the lack of any change in the anisotropy of the probe transmission in the spectral region of the Q resonance of this system.

Champion and co-workers reproduced these results with excitation at both 400 and 580 nm and a broadband probe spectrum that extended into bluer wavelengths.[32] Their study provided insight into two aspects of Mb dynamics. They showed that the identity of the axial ligand to the central Fe atom determines whether or not photolysis occurs. NO^- readily photolyzes, while water does not. They also show that a wider range of Mb systems show dynamics on time scales longer than 0.2 ps that are consistent with relaxation of a vibrationally excited ground electronic state. For the photolyzed MbNO system they use disparate temporal behavior of absorption and bleach features in the transient difference spectra to show that in order for a sequential, intermediate excited electronic state model to account for the observed dynamics, several excited states would need to contribute. They claimed that this necessity for several contributing excited states made the model of the 'hot' vibrational ground electronic state more reasonable.

More importantly, they show that the isosbestic point (zero-crossing of the difference spectrum) of the non-photolyzing metMB and deoxyMB evolve in a similar fashion to the results of Hochstrasser and co-workers. In the vicinity of the absorption feature to red wavelegnths of the Soret resonance of the ground state the zero-crossing difference spectrum of each species shifts to bluer wavelengths by circa 10 nm very rapidly (<10 ps). This shift is a characteristic of vibrational relaxation in a given electronic state. Since the isosbestic point continues to shift until the ground electronic state is fully recovered, Champion and co-workers conclude that the ground state vibrational cooling accounts dynamics on time scales longer than 0.3 ps and 0.4 ps for deoxy-Mb and metMb, respectively.

Measurements probing broadband TA of six-coordinate, $Fe^{(II)}$ porphyrin centers in Cytochrome c (Cyt c) showed similar dynamics.[11] After an ultrafast ligation of the methionine (≤ 40 fs) with a calculated quantum yield of 80%, broad peaks appear that are characteristic of a five-coordinate species. The features of measured difference spectra, however, do not shift in frequency as a function of probe delay. The authors use this stability and the similarity of the reconstructed absorption spectrum of the product state to that of the five-coordinate model heme microperoxidase-8 (MP-8) to further propose that a five-coordinate ground photoproduct state is formed through photolysis and subsequent vibrational cooling.

In this study, there are none of the proposed signatures of a vibrationally 'hot' six-coordinate ground state. This lack of a signatures coupled with the non-unity quantum yield of methionine photolysis seem to imply that there are sub-1.5 ps (quoted temporal resolution of the study) nonradiative relaxation pathways between the state initially excited at ~400 nm and the fully vibrationally relaxed ground electronic state of the six-coordinate, $Fe^{(II)}$ species. This very fast electronic relaxation is also confirmed via a very small, but measurable fluorescence (quantum yield $5x10^{-7}$) from the S_1 (Q) state upon Soret excitation. The quantum yield of Q fluorescence upon direct excitation is, however, $3x10^{-6}$. These disparate fluorescence quantum yields mean that nonradiative relaxation pathways from the initially excited state other than the S_2-S_1 internal conversion are approximately 7 times as efficient. These pathways include both direct relaxation to the S_0 ground state and photolysis of the methionine ligand to the five-coordinate species.

In contrast to the $Fe^{(II)}$ Cyt c, later measurements investigated the $Fe^{(III)}$ oxidation state of Cyt c upon 266 nm and 405 nm excitation.[19] This studied confirmed the existence of a 0.3 ps internal conversion lifetime from the initially excited state as well as a 4 ps lifetime associated with vibrational cooling of the ground electronic state, but did not discuss any photolysis of the axial ligands. The longer decay time of the internal conversion may be tied to the lack of competing photolysis pathways in this system. Furthermore, this studied showed the vibrationally excited state possessed enough excess thermal energy to overcome an energy barrier to the reduced $Fe^{(II)}$. The reduction of the iron atom did not occur via an excited electronic state.

The ultrafast dynamics of oxygen-bound hemoglobin (HbO_2) have also been investigated using ultrafast, visible TA spectroscopy.[12] Kobayashi showed the photolysis of the O_2 ligand occurs very rapidly with a measured lifetime of 45 fs. Broadband excitation of this dissociation also excites vibrational coherences of the excited HbO_2 that persist for up 100 fs. These coherences correspond to the O=O stretching vibration and the time delays to which that are observable in the difference spectra help to confirm the lifetime of the O_2 bound state. The lifetime of the photolyzed Hb species was established as 680 fs, though the authors do not explicitly designate this as the lifetime of the electronically excited Hb state. In that time scale water ligates to the Hb species to produce metHb, whose signatures in the difference spectra appear in less than 1 ps. Longer lifetimes are assigned to two stages of vibrational cooling of the product state.

Studies examining the ultrafast dynamics of biological iron-centered hemes share two major characteristics. First, the models propose a <0.1-0.3 ps lifetime of the initially excited state. The internal conversion of this state to the next highest excited singlet state competes with at least two nonradiative pathways: photolysis of an axial ligand and direct conversion to the ground state via CT states between the heme ring and Fe atom. Sequential internal conversion has been estimated via fluorescence quantum yields for some of these systems. Second, the models propose a sequence of 0.5-10 ps lifetimes assigned to different stages of vibrational dephasing and cooling. This cooling is characterized by spectral red-shifting and narrowing of and the disparate temporal behavior of the different features of the measured difference spectra.

Champion's group has also examined the ultrafast dynamics of two different high-spin, five coordinate iron (III) porphyrin halides.[13] Using femtosecond coherence spectroscopy (FCS), his group has fully characterized the low frequency, 'soft-modes' of the porphyring ring with frequencies less than 400 cm^{-1} that are excited with broadband, ultrafast pulses. As the molecule coherent vibrates at allowed frequencies (Raman selection rules apply), the measured probe transmission is modulated at the same frequencies. The fitted kinetic traces are then subtracted off the data and a Fourier transform calculates the vibrations coherently excited by the pulse. Such a measurement can identify the vibrational mode of axial ligands and determine the extent to which photolysis has occurred.

In contrast to the case of ferrous Cyt c, some Mb species and HbO_2, the vibrational information from the FCS measurements shows that the Fe-halide bond of $Fe^{(III)}PCl$ or $Fe^{(III)}PBr$ is not photolysed after excitation on the Soret transition. A vibration measured at 343 cm^{-1} in $Fe^{(III)}PCl$ was assigned to two closely-spaced Fe-Cl and porphyrin out-of-plane distortion combination modes via DFT calculations. These vibrations appear at very early times in the measurement (<500 fs). Since sub-ps photolysis and geminate recombination of the axial ligand is unlikely given the recombination dynamics measured in heme proteins, it is very likely that the Cl is not photolyzed upon Soret excitation of $Fe^{(III)}PCl$. Given that the peripheral substitution of the porphyrin marcocycle should not significantly affect the metal-halide bonding, it seems reasonable to conclude that photolysis does not play a significant role in the transient dynamics of excited $Fe^{(III)}$TPPCl.

With this information on the transient, ultrafast dynamics of other iron-centered porphyrin analog systems in hand, we can begin to unravel the excited state dynamics of $Fe^{(III)}$TPPCl from above. First, for 400 nm excitation, we measure an initial, fast lifetime of 0.53 ps in toluene, 0.5 ps in the 1:1 mixture of toluene and DCM and 0.58 ps in DCM. The temporal instrument function over a given 5 nm probe bandwidth ranges between 0.2-0.25 ps. This instrument function is limited by the fits at early times, which are problematic due to cross-phase modulation between the pump and probe in the sample. In the absence of a photolysis pathway upon excitation, the lifetime of the initially excited state should be longer than in system in which photolysis occurs. For the case where no photolysis pathway exists, the fastest lifetime measured in ferric Cyt C is 0.3 ps.[19]

Again, from the FCS measurements of $Fe^{(III)}$PCl,[13] it seems likely that there is not a measureable photolysis pathway in $Fe^{(III)}$TPPCl. With time resolution shorter than 0.3 ps, our measurement seems to show that this circa 0.5 ps lifetime in the decay of $Fe^{(III)}$TPPCl is an internal conversion, either between the initially and other excited states or the initially excited state and the ground electronic state of the molecule. To decipher between these competing processes, spectrally resolved transient information from the broadband probe is necessary.

In analyzing the transient dynamics of the photolyzed MbNO, Champion and co-workers compare the temporal changes in the spectral region to the blue of the Soret transition (~385 nm) to those of the spectral region to the red of the Soret transition (~435 nm). [32] Based on this comparison they conclude that a vibrationally ‘hot’ electronic ground state is the most likely identity of the measured photoproduct. The changes in these two regions move in opposition directions in their measurement on differing time scales. They claim that the decay of a single intermediate, electronic state would show changes in absorption of the same sign and at the same rate. These authors also compare the transient dynamics measured at 400 nm and 420 nm to draw the same conclusion.

In these regions of the difference spectrum of Fe$^{(III)}$TPPCl excited on the Soret transition measured at rm. T in a 1:1 mixture of toluene and DCM, similar behavior is observed, as seen in FIG. 4.6. (Fits in the first 0.2-0.25 ps show anomalous behavior due to nonlinear mixing of the pump and probe at early times, as discussed above.)

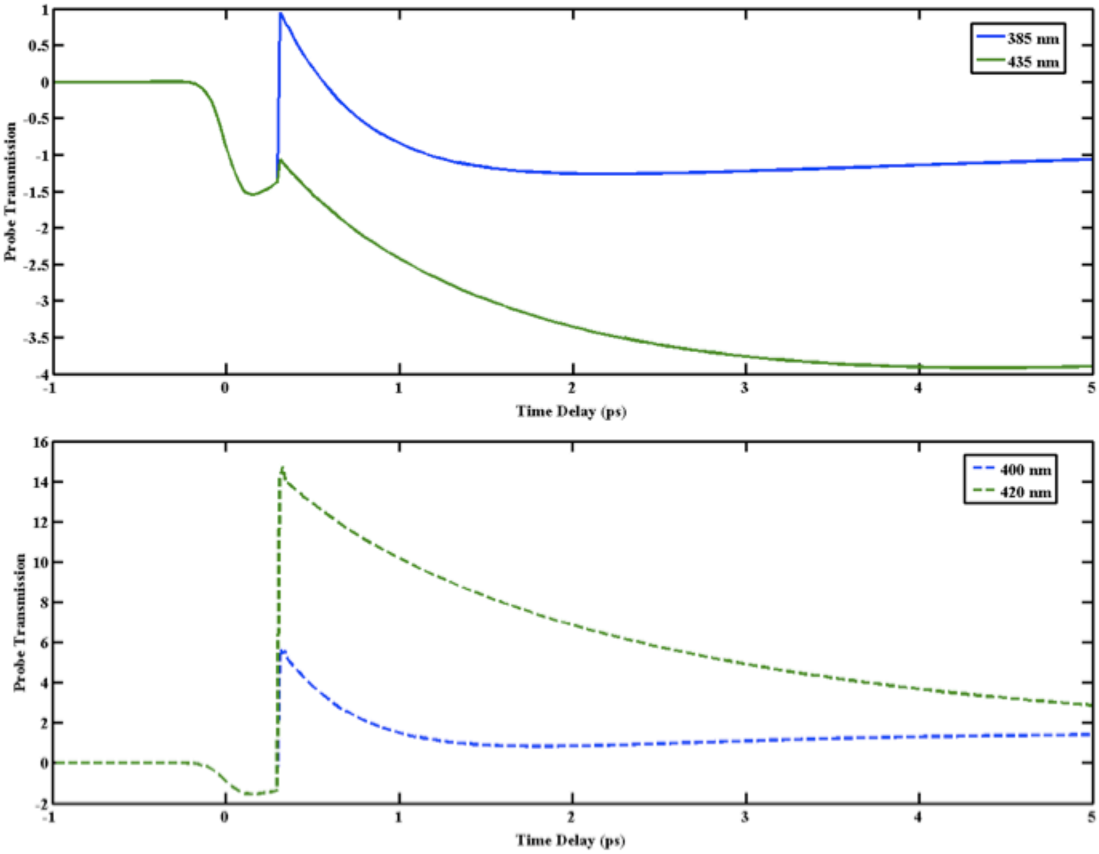

FIG. 4.6. Comparison of probe transmission between (upper panel) 385 nm and 435 nm absorption features and (lower panel) 400 nm and 420 nm ground state bleach features of Fe$^{(III)}$TPPCl in 1:1 mixture of toluene and DCM. The difference in the temporal behavior in these pairs of probe wavelengths was used to show the features did not correspond to the same state and promote the model of 1-10 ps vibrational cooling of the ground electronic state of MbNO.

Comparing the temporal behavior of these pairs of spectral features in the difference spectra of Fe$^{(III)}$TPPCl, we see that differing dynamics are present in each case. The absorption feature at 385 nm rises visibly faster than that at 435 nm. As in the case of Mb, these two features cannot correspond to a single state. The same is true of the comparison of the bleaches at 400 nm and 420 nm. While the ground state Soret bleach decays from its initial appearance, there is a rise to the bleach at 400 nm. Again, as pointed out by Champion, these features cannot describe the dynamics of a single state. The similarity between these traces and those presented by Champion is striking considering that each respective measurement was pumped on a different electronic transition.

The longer time constants from the global fit of the three solvents also points to similar results to those seen in biological hemes.[8, 10-12, 19, 32] The third time constant is Table I. is strongly solvent dependent. This decay is fastest in toluene and slowest in DCM, with the 1:1 mixture falling between the two. Possible co-facial packing of the toluene solvent molecule could provide a mechanism for increased transfer of energy to the solvent environment in these measurements. As a polar solvent, DCM molecules encounter more repulsion and may not dissipate energy away from the ring as easily as toluene. The probe anisotropies across the probe region also do not show any significant dynamics after a few hundred fs, similarly to the transient dynamics of Mb measured by Hochstrasser and co-workers. [8, 10-12, 19, 32]

Based on the work of Champion and Hochstrasser, the rm. T TA dynamics of $Fe^{(III)}$TPPCl excited at 400 nm seem to mimic those of biological hemes. These dynamics would then be explained well by a fast internal conversion (~0.5 ps) followed by two slower vibrational relaxations of the electronic ground state with lifetimes of ~2 ps and ~15 ps, respectively.

At least two aspects of the TA results do not fit with the accepted models of Fe-centered heme proteins, however. First, difference spectra at 88 K show anomalous results based upon a dominant thermal relaxation of the electronic ground state at longer times (>0.5 ps). As seen in FIG. 4.2(c), at probe delays of ~500 ps there is still a substantial difference spectrum present in the sample. This difference spectrum closely resembles that of the state B in the sequential model presented in the Results section B.2. The presence of this long-lived feature in the low temperature transient dynamics is inconsistent with a model proposing circa 1 ps vibrational relaxation of the electronic ground state of this system.

Mizunati and Kitagawa have studied the vibrational energy relaxation (VER) of several transition metalloporphyrins.[72] They have proposed a model for intermolecular vibrational energy relaxation based on time-resolved resonance Raman measuring the transient dynamics of the anti-Stokes scattering in photo-excited systems. This model claims that very-fast dissipation of vibrational energy is caused by interactions between the excited metalloporphyrin and solvent environment. A slower time constant is due to a solvent-solvent interactive rate-determining step in the full vibrational relaxation of the photo-excited chromophore. This solvent-solvent interaction is dependent on the solvent thermal conductivity.

With this model in mind, there are two distinct physical possibilities for this long-lived state at 88 K: 1) a vibrationally 'hot' ground electronic state insulated from its environment by a significantly smaller thermal conductivity of the glass form of the solvent than that of the room temperature solvent environment or 2) an excited electronic state/s normally populated in rm. T transient dynamics whose lifetime/s become elongated at 88 K. As stated above, the contribution to the long time (VER) component is dependent on the solvent's thermal conductivity. To determine if the nature of the state appearing in the low T. TA measurements, we must find a method to estimate the thermal conductivity of the 1:1 mixture of toluene and DCM around 88 K.

Research into the formation, dynamics and properties of dielectric, amorphous solids has been ongoing for over 70 years.[73-78] However, explicit measurements of the thermal properties of the glass used in these measurements have not been made as of yet. This fact makes comparison to similar and dissimilar glasses a necessity in providing the clearest possible picture of the measured excited state dynamics. Some of the most recent research into glasses formed from ethanol and glycerol shows that thermal conductivity does not vary by more than a factor of 10 from room temperature values.[76, 77] This variation in the magnitude of the thermal conductivity has also been seen in a range of inorganic glasses.[74, 78] One organic polymer (PMMA) whose structure and, possibly, properties resemble those of the glass we use in our measurements shows an even smaller change in its thermal conductivity over the temperature range 80-290 K.[74]

Mizunati and Kitagawa show that a decrease in the thermal conductivity of the solvent of a factor of 10 leads to an increase in the lifetime of the VER much smaller than a factor of 10 for a model system.[72] We observe a change in the lifetime of the B state in our measurements of larger than a factor of 100. Based on the simplistic model of Mizunati and Kitagawa one would expect a change in the thermal conductivity of several orders of magnitude in order to produce such a substantial increase in the lifetime based on a VER analysis alone. A change in the thermal properties of the solvent environment, however, is very unlikely.

The lack of a very dramatic change in the thermal diffusivity of the solvent environment in the glass phase makes the conclusion that a vibrationally excited ground state could persist for 100's ps in a solvent environment at 88K highly improbable. This conclusion can also be reached from simple physical intuition. With no change in the excitation wavelength, the same amount of energy is being deposited into the chromophore. However, a dramatic decrease in the thermal energy of the solvent molecules creates a much larger temperature gradient between the solute and solvent. Physical intuition of thermal diffusion leads one to conclude that this increased temperature gradient will decrease, not increase, the lifetime associated with intermolecular VER. As the gradient gets larger, the energy will flow 'downhill' more quickly, not more slowly.

Based on both the lack of clear evidence of very large changes in the thermal conductivity of other glasses (both organic and inorganic) and the physical intuition of thermal diffusion at low temperatures, the low temperature difference spectrum measured at ~500 ps probe delay likely comes from an excited electronic state or states. From the discussion above and Champion's work on Mb, however, we know that the dynamics of the absorption and bleach features in the region between 380-440 nm cannot occur from a single state. The data then seem to point in the direction of at least two contributing electronic states to the transient dynamics measured at both rm. and low temperatures. These states have only recently been identified and assigned in the region to the red of the Soret transition excited in these measurements.

The second inconsistency with the application of the accepted model for heme dynamics to those of Fe$^{(III)}$TPPCl concerns the evolution of the zero-crossing to the red of the Soret bleach in the measured difference spectra. As stated above, the isosbestic point between the Soret bleach and the absorption feature to redder wavelengths in the difference spectrum of both metMb and deoxyMb continues to rapidly evolve to bluer wavelengths until the ground state is fully recovered. The conclusion from this facet of the measurement is that the thermal relaxation implied by the blue-shift must be occurring on the ground electronic state.

In contrast to the case of metMb and deoxyMB, Fe$^{(III)}$TPPCl shows a different evolution of this isosbestic point. FIG. 4.7 shows a representative time series of the evolution of the difference spectrum of Fe$^{(III)}$TPPCl excited at 400 nm and measured in a 1:1 mixture of DCM and toluene. Time delays between 5 and 50 ps are shown with 5 ps time steps.

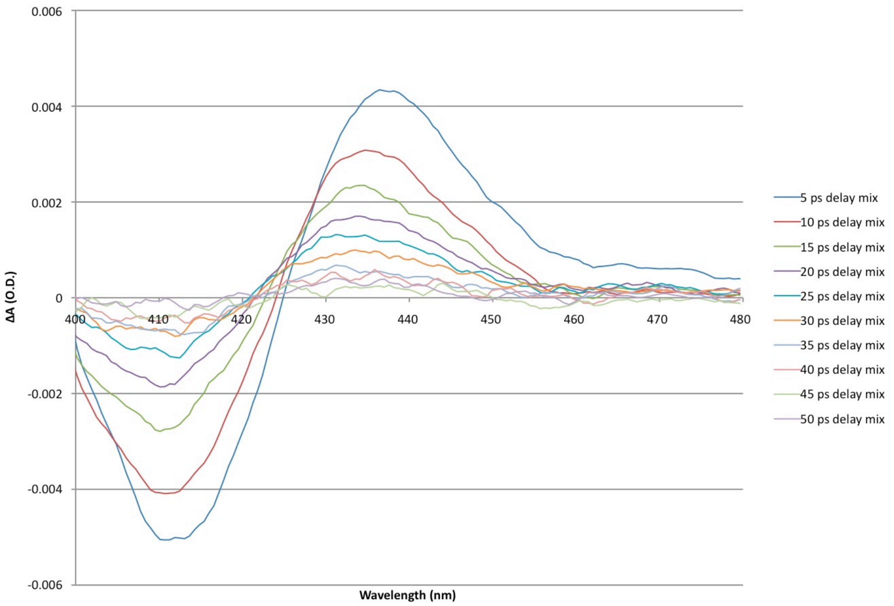

FIG. 4.7. Representative time series of difference spectra of Fe$^{(III)}$TPPCl excited at 400 nm in a 1:1 mixture of toluene and DCM. For time delays longer than 5 ps the isosbestic point near 420 nm shows shifts much smaller and less rapid than observed in non-photolyzed Mb systems indicative of a dominant electronic non-radiative relaxation pathway on these time scales.

From FIG. 4.7 is clear that as the ground electronic state recovers, Fe$^{(III)}$TPPCl does not show a shift of this isosbestic point at a rate or magnitude similar to those observed in Mb systems by Champion and co-workers. The solvent-dependent kinetic traces of this isosbestic point are shown in FIG. 4.8.

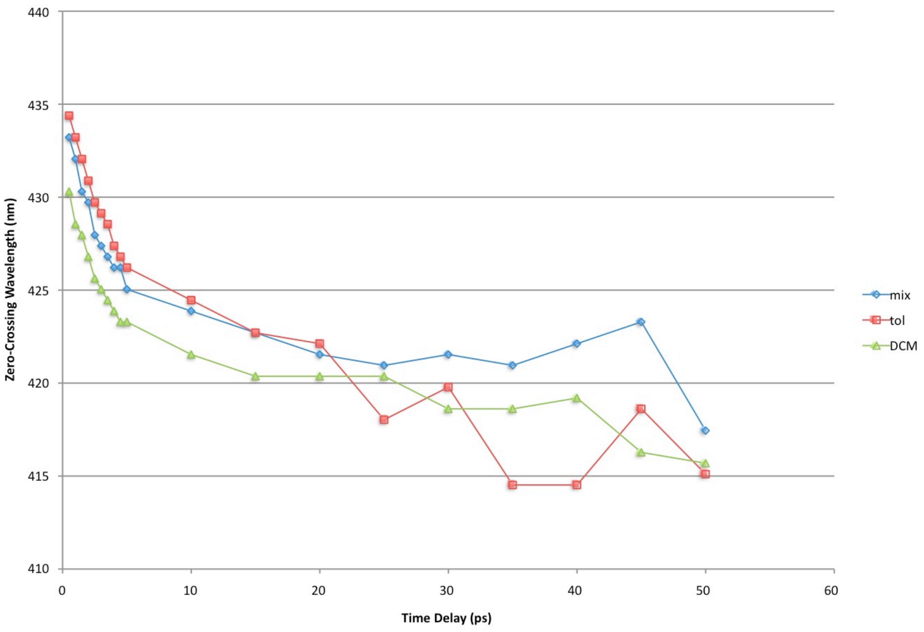

FIG. 4.8. Kinetic traces of isosbestic point to the red of the Soret bleach as a function of the solvent environment. Each solvent shows evolution of the zero-crossing on two distinct time scales: 1) a more rapid and larger shift for time delays less than 5 ps and 2) a less rapid and smaller shift on time scales longer than 5 ps. A clear trend at longer times is difficult to assign due to smaller signal-to-noise at those probe delays.

While trends in FIG. 4.8 are clearly identified at early times, they are harder to decipher at longer times. There also seems to be a solvent-dependent variation in the extent to which such a long-time trend can be seen. Both of these aspects of FIG. 8 are due to the fact that the signal around the zero-crossing at the latest probe time delays is much smaller than measured at earlier times. The apparent solvent dependence is largely due to the fact that the largest signals were measured in DCM. Therefore, the DCM kinetic trace contains less noise at the latest times.

At early times, FIG. 4.8 shows that the isosbestic point shifts by almost 10 nm in every solvent. This shift also occurs as rapidly as observed in Mb derivatives. From these observations it seems that vibrational cooling is playing a significant role in the non-radiative relaxation.

On time scales longer than 5 ps, however, the zero-crossing evolves very differently than those of the Mb systems. The isosbestic point significantly slows its shift to bluer wavelengths. In the mixture of the two solvents it seems that the isosbestic might begin to shift back to redder wavelengths, although the small signal-to-noise ratios at those time delays mean that further measurements would be needed to substantiate that trend. The time series difference spectra from 5-50 ps in FIG. 4.7 also does not show any shifts characteristic of vibrational relaxation. By 10 ps the feature centered at 435 nm shows neither the peak shifts nor narrowing that signify vibrational relaxation.

The dynamics of the position of this zero-crossing show similar behavior when excited on the Q_v near 520 nm. FIG. 4.9 shows the comparison of these dynamics when Soret excited to Q_v when the sample is dissolved in a 1:1 mixture of toluene and DCM. The same time steps are shown as in FIG. 4.8. (0.5-50 ps time delay)

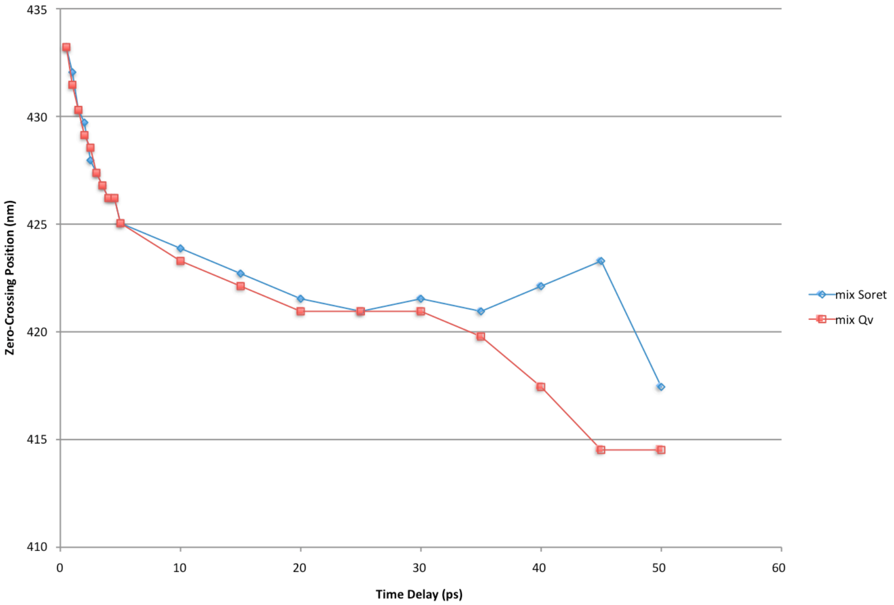

FIG. 4.9. Comparison of the dynamics of the isosbestic point to redder wavelengths of the Soret bleach of Fe$^{(III)}$TPPCl for Soret excitation near 400 nm to Q_v excitation near 520 nm in a 1:1 mixture of toluene and DCM. The traces are very similar for probe time delays up to 35 ps.

From FIG. 4.9, one clearly sees that this isosbestic point shows the exact same qualitative behavior for both excitation wavelengths in the first 5 ps of evolution. While this similarity in the trends does not conclusively mean that the same relaxation processes are taking place at the same time delays for both excitation wavelengths, it seems unlikely that two completely different combinations of electronic and vibrational relaxations would result in qualitatively indistinguishable dynamics of this zero-crossing. Therefore, we tentatively conclude that by 0.5 ps after excitation the same electronic states are populated upon excitation at either wavelength. This puts an upper limit on the lifetime of the state initially excited at 400 nm and shows that the entire electronic relaxation is substantially longer than this lifetime.

Both the appearance of a much longer-lived signal at low temperature and the lack of the characteristic features of vibrational relaxation at room temperature disagree with the model of very rapid (<0.3 ps) electronic relaxation to the ground state followed by sequential vibrational relaxation on longer time scales. As discussed above, studies on the VER of transition metal porphyrins cannot account for a lifetime 100 times longer at low temperatures based upon changes in the thermal conductivity of the solvent. Physical intuition also leads one to question how and why a vibrationally excited ground electronic state would persist so much longer at significantly lower temperatures.

The characteristics of the room temperature measurements also do not conform to the standard observations of heme proteins dynamics. While there is a rapid and large shift of the isosbestic point red of the Soret bleach for the first 5 ps after the arrival of the pump pulse, this shift slows dramatically at longer times. The observed spectral features also do not show the characteristic narrowing as the ground state fully recovers at significantly longer times. The spectrum simply decays, indicative of an electronic non-radiative decay channel as the longest process in the dynamics of the photo-excited molecule. For time delays longer than 0.5 ps this longer lifetime decay is not dependent on the wavelength of excitation.

If the longest-lived state is an excited electronic state, the states populated before that relaxation must also be excited electronic states. Therefore, the ultrafast dynamics of

$Fe^{(III)}$TPPCl are dominated by some sort of sequential excited electronic state relaxation. The fastest processes also show significant thermal cooling, indicated by the strong shift to the blue by the isosbestic point of interest explored above.

As discussed in the introduction, Paulat and Lehnert have investigated the electronic structure and optical transition of $Fe^{(III)}$TPPCl via DFT calculations, rm. T UV-vis measurements and low and rm. T magnetic circular dichroism (MCD) measurements.[79] In addition to several prototypical ππ* excitations, they identify 6 different types of charge transfer (CT) transitions in which either the porphyrin ring or axial Cl atom donate an electron to the central Fe atom (LMCT states). The out-of-plane LMCT transitions involving Cl are especially important in the context of the comparison of our results to those involving biological hemes. Since much smaller atoms are bound to the central Fe atom in heme systems and photolysis plays a significant role in transient dynamics, out-of-plane axial LMCT transitions may not be possible.

For their analysis, Paulat and Lehnert calculate several excited states of $Fe^{(III)}$TPPCl from TD-DFT methods to assign the observed optical transitions. These calculations show several electronic states populated via different LMCT processes that lie in energy between the states populated on 400 nm and 413 nm excitation and those populated with Q_v. This region is especially important in the context of the photochemistry elucidated from rR scattering, as discussed below. Upon a LMCT process, the toluene solvent environment could provide enough energy stabilization that at least two of the excited states in this energy region would live for dramatically longer at low temperatures.

The fact that there are several states in this energy region also strengthens the argument that several different electronic states are participating in both the rm. and low temperature transient dynamics. Such a dynamical model would agree with the temporal behavior exposed in FIG. 4.6. With several states very close in energy, the potential energy surface crossings are likely very complex, including internal conversion to out-of-plane Fe-Cl LMCT states. There are also likely different energy barriers to relaxation along different reaction coordinates that are sensitive to the thermal energy of the solvent environment. With this sensitivity these barriers could trap population for substantial periods of time lengthen the lifetimes of contributing excited states at 88 K.

As $Fe^{(III)}$TPPCl is a large, complex molecule, the assignment of these states, surface crossings and energy barriers is difficult. The data from the above measurements alone does not allow us to assign which excited states should be contributing or the height of the barriers that trap population at low temperatures. We are only able to show that proposed models for the ground state vibrational cooling of other metalloporphyrins on time scales longer than 5 ps cannot account for the observed difference spectra at low temperature or the observed dynamics an important zero-crossing.

One cannot, however, easily extrapolate these results to the transient dynamics of biological heme proteins. A complete comparison would necessitate measured dynamics excited in a range of energies not explored above. Also, as stated previously, axial ligation dynamics are very important in the ultrafast transient behavior of several hemes. With small diatomic molecules composed of N, C and O and water axial ligands, biological hemes are not offered the same types of LMCT transitions and states as systems possessing halide axial ligands like Cl and Br. Since Cl and Br are significantly larger with many more electrons than first row non-metals, their atomic structure affords more flexibility in CT processes. As pointed out by Paulat and Lehnert, many of the states and transitions in the region to lower energy of both Soret the Q_v resonances in $Fe^{(III)}$TPPCl contain out-of-plane LMCT character. These states do not exist in biological hemes due to the differences in the axial ligands in each case.

In both of these energy regions exist several CT transitions and states that do contain porphyrin-Fe LMCT character. With the observations from the measurements explored above we have no way to explicitly rule out that porphyrin-Fe LMCT transitions and states could provide enough non-radiative pathways in biological hemes to account for the observed dynamics in several studies. The presence of aspects inconsistent with the model of ultrafast (<0.1-0.3 ps) internal conversion to the electronic ground state followed by sequential vibrational cooling in the measurement above may mean ultrafast, excited state dynamics some in hemes and Fe-porphyrins need re-evaluation. This new information could help to elucidate dynamics and behavior in a range of molecular systems important to biology, materials science, electrical engineering and optics.

Conclusions

Temperature and solvent dependent broadband, ultrafast transient absorption measurement were measured with Soret (~400 nm) and Q_v (520 nm) pump excitation to elucidate the excited state dynamics of $Fe^{(III)}$TPPCl. Measurements were made in three solvent environments at room temperature: neat toluene, neat DCM and a 1:1 mixture of toluene and DCM. At low temperature measurements were made in a 1:1 mixture solvent environment of toluene and DCM.

A three state model is proposed to account for the observed dynamics based on a global spectral analysis of the room temperature measurements. The shortest-lived state shows a distinct dependence on the excitation energy, likely due to the difference in the initially populated state in each case. The two longer lifetimes show stronger dependence on the solvent environment with DCM displaying longer lifetimes than toluene. The mixture solvent shows intermediate values for these lifetimes.

Measurements show the lifetime of longest-lived state increases dramatically at low temperature. While this state decays in less than 20 ps at room temperatures, it displays a strong signal in measurements at 500 ps probe delay at low temperature (88 K). Subsequent calculations in Chapter 5 using power dependent resonance Raman scattering measurements place a range of lifetimes for this state between 1ns and 10 us.

At room temperature, the isosbestic point to redder wavelengths of the Soret bleach in the measured difference spectra does not vary as substantially for $Fe^{(III)}$TPPCl as similarly structured heme proteins. The position of the isosbestic point is close to constant over the time range that the longest-lived state decays (5-50 ps). A constant isosbestic point during the decay in such a measurement is an indication of a dominant electronic decay mechanism.

An electronic decay mechanism for the longed-lived state at room temperature implies that the ultrafast excited state dynamics of $Fe^{(III)}$TPPCl differ from those of heme proteins. In hemes, the dominant relaxation pathway is sub-ps internal conversion to the ground electronic state followed by its vibrational cooling. The dynamics of the isosbestic to the red of the Soret bleach indicate an electronic relaxation on time scales of 10's of ps. Observations of longer-lived transient at lower temperatures are also consistent with a dominant sequential electronic relaxation model for the ultrafast dynamics of Fe$^{(III)}$TPPCl. This result sheds new light onto the ability of heme proteins to correctly model the ultrafast dynamics of synthetic iron porphyrins.

References

1. P. A. Cornelius, A. W. Steele, D. A. Chernoff and R. M. Hochstrasser, Chem. Phys. Lett. **82** (1), 9-14 (1981).
2. Y. Liang, D. K. Negus, R. M. Hochstrasser, M. Gunner and P. L. Dutton, Chem. Phys. Lett. **84** (2), 236-240 (1981).
3. S. Sorgues, L. Poisson, K. Raffael, L. Krim, B. Soep and N. Shafizadeh, J. Chem. Phys. **124** (11), 10 (2006).
4. M. C. Yoon, D. H. Jeong, S. Cho, D. Kim, H. Rhee and T. Joo, J. Chem. Phys. **118** (1), 164-171 (2003).
5. M. Gouterman, in *The Porphyrins*, edited by D. Dolphin (Academic Press, New York, 1978), Vol. 3, pp. 1-166.
6. A. Warshel, Chem. Phys. Lett. **43** (2), 273-278 (1976).
7. F. Paulat, V. K. K. Praneeth, C. Nather and N. Lehnert, Inorganic Chemistry **45** (7), 2835-2856 (2006).
8. Y. Kholodenko, M. Volk, E. Gooding and R. M. Hochstrasser, Chemical Physics **259** (1), 71-87 (2000).
9. B. M. Cho, C. F. Carlsson and R. Jimenez, J. Chem. Phys. **124** (14), 15 (2006).
10. M. Negrerie, S. Cianetti, M. H. Vos, J. L. Martin and S. G. Kruglik, Journal of Physical Chemistry B **110** (25), 12766-12781 (2006).
11. W. Wang, X. Ye, A. A. Demidov, F. Rosca, T. Sjodin, W. X. Cao, M. Sheeran and P. M. Champion, Journal of Physical Chemistry B **104** (46), 10789-10801 (2000).
12. A. Yabushita and T. Kobayashi, Journal of Physical Chemistry B **114** (35), 11654-11658 (2010).
13. M. Kubo, F. Gruia, A. Benabbas, A. Barabanschikov, W. R. Montfort, E. M. Maes and P. M. Champion, Journal of the American Chemical Society **130** (30), 9800-9811 (2008).
14. J. C. Postlewaite, J. B. Miers and D. D. Dlott, Journal of the American Chemical Society **111** (4), 1248-1255 (1989).
15. M. H. Ha-Thi, N. Shafizadeh, L. Poisson and B. Soep, Physical Chemistry Chemical Physics **12** (45), 14985-14993 (2010).

16. L. Zhu, P. Li, M. Huang, J. T. Sage and P. M. Champion, Physical Review Letters **72** (2), 301-304 (1994).
17. X. Ye, D. Ionascu, F. Gruia, A. Yu, A. Benabbas and P. M. Champion, Proceedings of the National Academy of Sciences of the United States of America **104** (37), 14682-14687 (2007).
18. L. Y. Zhu, J. T. Sage and P. M. Champion, Science **266** (5185), 629-632 (1994).
19. D. Lowenich, K. Kleinermanns, V. Karunakaran and S. A. Kovalenko, Photochemistry and Photobiology **84** (1), 193-201 (2008).
20. S. Franzen, L. Kiger, C. Poyart and J.-L. Martin, Biophysical Journal **80** (5), 2372-2385 (2001).
21. D. Kim, C. Kirmaier and D. Holten, Chemical Physics **75** (3), 305-322 (1983).
22. B. I. Greene, Chem. Phys. Lett. **117** (2), 191-195 (1985).
23. D. Kim and D. Holten, Chem. Phys. Lett. **98** (6), 584-589 (1983).
24. S. K. K. Kumar, V. Tiwari, T. Goswami and D. Goswami, Chem. Phys. Lett. **476** (1-3), 31-36 (2009).
25. M. Maiti and R. P. Steer, Chem. Phys. Lett. **482** (4-6), 254-258 (2009).
26. C. D. Tait, D. Holten and M. Gouterman, Chem. Phys. Lett. **100** (3), 268-272 (1983).
27. J. Rodriguez and D. Holten, J. Chem. Phys. **91** (6), 3525-3531 (1989).
28. J. Rodriguez, C. Kirmaier and D. Holten, J. Chem. Phys. **94** (9), 6020-6029 (1991).
29. T. Suemoto, H. Ebihara, H. Nakao and M. Nakajima, J. Chem. Phys. **134** (3), 034502 (2011).
30. P. A. Cornelius, R. M. Hochstrasser and A. W. Steele, Journal of Molecular Biology **163** (1), 119-128 (1983).
31. A. N. Okhrimenko, A. V. Gusev and M. A. J. Rodgers, J. Phys. Chem. A **109** (34), 7653-7656 (2005).
32. X. O. Ye, A. Demidov, F. Rosca, W. Wang, A. Kumar, D. Ionascu, L. Y. Zhu, D. Barrick, D. Wharton and P. M. Champion, J. Phys. Chem. A **107** (40), 8156-8165 (2003).
33. H. Z. Yu, J. S. Baskin and A. H. Zewail, J. Phys. Chem. A **106** (42), 9845-9854 (2002).
34. M. Andersson, J. Davidsson, L. Hammarstrom, J. Korppi-Tommola and T. Peltola, Journal of Physical Chemistry B **103**, 3258-3262 (1999).
35. L. Y. Luo, C. H. Chang, Y. C. Chen, T. K. Wu and E. W. G. Diau, Journal of Physical Chemistry B **111** (26), 7656-7664 (2007).
36. D. W. Dixon, C. Kirmaier and D. Holten, Journal of the American Chemical Society **107** (4), 808-813 (1985).
37. C. R. Guest, K. D. Straub, J. A. Hutchinson and P. M. Rentzepis, Journal of the American Chemical Society **110** (16), 5276-5280 (1988).
38. D. Kim, D. Holten and M. Gouterman, Journal of the American Chemical Society **106** (10), 2793-2798 (1984).
39. D. Taube, T. G. Traylor, D. Magde, K. Walda and J. Luo, Journal of the

American Chemical Society **114** (23), 9182-9188 (1992).
40. J. J. Loparo, C. M. Cheatum, M. R. Ondrias and M. C. Simpson, Chemical Physics **286** (2-3), 353-374 (2003).
41. J. C. Austin, S. E. J. Bell and R. E. Hester, Chem. Phys. Lett. **169** (4), 342-346 (1990).
42. B. Dietzek, R. Maksimenka, W. Kiefer, G. Hermann, J. Popp and M. Schmitt, Chem. Phys. Lett. **415** (1-3), 94-99 (2005).
43. M. Inamo, C. Okabe, T. Nakabayashi, N. Nishi and M. Hoshino, Chem. Phys. Lett. **445** (4-6), 167-172 (2007).
44. L. Y. Luo, C. W. Chang, C. Y. Lin and E. W. G. Diau, Chem. Phys. Lett. **432** (4-6), 452-456 (2006).
45. J. P. M. Schelvis and C. A. Varotsis, Chem. Phys. Lett. **321** (1-2), 37-42 (2000).
46. P. M. Champion and R. Lange, J. Chem. Phys. **73** (12), 5947-5957 (1980).
47. P. M. Champion and G. J. Perreault, J. Chem. Phys. **75** (1), 490-491 (1981).
48. S. Tobita, Y. Kaizu, H. Kobayashi and I. Tanaka, J. Chem. Phys. **81** (7), 2962-2969 (1984).
49. Y. Zhang, H. Fujisaki and J. E. Straub, J. Chem. Phys. **130** (2) (2009).
50. R. V. Maxirniano, E. Piovesan, S. C. Zilio, A. E. H. Machado, R. de Paula, J. A. S. Cavaleiro, I. E. Borissevitch, A. S. Ito, P. J. Goncalves and N. M. B. Neto, Journal of Photochemistry and Photobiology a-Chemistry **214** (2-3), 115-120 (2010).
51. N. Mataga, H. Chosrowjan and S. Taniguchi, Journal of Photochemistry and Photobiology C: Photochemistry Reviews **6**, 37-79 (2005).
52. S. Sato, K. Kamogawa, K. Aoyagi and T. Kitagawa, Journal of Physical Chemistry **96** (26), 10676-10681 (1992).
53. J. Terner, D. F. Voss, C. Paddock, R. B. Miles and T. G. Spiro, Journal of Physical Chemistry **86** (6), 859-861 (1982).
54. J. S. Baskin, H. Z. Yu and A. H. Zewail, J. Phys. Chem. A **106** (42), 9837-9844 (2002).
55. R. T. Hayes, C. J. Walsh and M. R. Wasielewski, J. Phys. Chem. A **108** (13), 2375-2381 (2004).
56. S. C. Jeoung, D. Kim, D. W. Cho and M. Yoon, J. Phys. Chem. A **104** (21), 4816-4824 (2000).
57. J. Karolczak, D. Kowalska, A. Lukaszewicz, A. Maciejewski and R. P. Steer, J. Phys. Chem. A **108** (21), 4570-4575 (2004).
58. D. LeGourrierec, M. Andersson, J. Davidsson, E. Mukhtar, L. Sun and L. Hammarstrom, J. Phys. Chem. A **103**, 557-559 (1999).
59. X. Liu, U. Tripathy, S. V. Bhosale, S. J. Langford and R. P. Steer, J. Phys. Chem. A **112** (38), 8986-8998 (2008).
60. A. Marcelli, P. Foggi, L. Moroni, C. Gellini and P. R. Salvi, J. Phys. Chem. A **112** (9), 1864-1872 (2008).
61. A. Morandeira, L. Engeli and E. Vauthey, J. Phys. Chem. A **106** (19), 4833-4837 (2002).

62. L. Moroni, C. Gellini, P. R. Salvi, A. Marcelli and P. Foggi, J. Phys. Chem. A **112** (44), 11044-11051 (2008).
63. J. Szmytkowski, T. Bond, M. F. Paige, R. W. J. Scott and R. P. Steer, J. Phys. Chem. A **114** (43), 11471-11476 (2010).
64. L. Y. Luo, C. F. Lo, C. Y. Lin, I. J. Chang and E. W. G. Diau, Journal of Physical Chemistry B **110** (1), 410-419 (2006).
65. C. D. Tait, D. Holten, M. H. Barley, D. Dolphin and B. R. James, Journal of the American Chemical Society **107** (7), 1930-1934 (1985).
66. C. D. Tait, D. Holten and M. Gouterman, Journal of the American Chemical Society **106** (22), 6653-6659 (1984).
67. N. Banerji, S. V. Bhosale, I. Petkova, S. J. Langford and E. Vauthey, Physical Chemistry Chemical Physics **13** (3), 1019-1029 (2011).
68. K. C. Tang, A. Rury, M. B. Orozco, J. Egendorf, K. G. Spears and R. J. Sension, J. Chem. Phys. **134** (10) (2011).
69. X. W. Yan and D. Holten, Journal of Physical Chemistry **92** (21), 5982-5986 (1988).
70. J. Rodriguez, C. Kirmaier and D. Holten, Journal of the American Chemical Society **111** (17), 6500-6506 (1989).
71. J. R. Hill, C. J. Ziegler, K. S. Suslick, D. D. Dlott, C. W. Rella and M. D. Fayer, Journal of Physical Chemistry **100** (46), 18023-18032 (1996).
72. Y. Mizutani and T. Kitagawa, Journal of Molecular Liquids **90** (1998), 233-242 (2001).
73. C. Kittel, Physical Review **75** (6), 972-974 (1949).
74. D. G. Cahill and R. O. Pohl, Phys. Rev. B **35** (8), 4067-4073 (1987).
75. X. Y. Kuang, I. Morgensternbadarau and I. Malfant, Phys. Rev. B **47** (9), 5455-5458 (1993).
76. S. Vieira, M. A. Ramos, Q. W. Zou and C. Talon, Phase Transitions **64** (1-2), 87-102 (1997).
77. C. Talon, Q. W. Zou, M. A. Ramos, R. Villar and S. Vieira, Phys. Rev. B **65** (1), 012203 (2001).
78. R. O. Pohl, X. Liu and E. Thompson, Reviews of Modern Physics **74** (4), 991-1013 (2002).
79. F. Paulat and N. Lehnert, Inorganic Chemistry **47** (11), 4963-4976 (2008).

Chapter 5:
Low Temperature Photochemistry of $Fe^{(III)}$TPPCl

Introduction

Metalloporphyrins and their analogs are among the most extensively studied systems in chemistry[1-29]. Interest in the chemical, electronic, optical, and photochemical properties of porphyrin-ring molecules arises from their widespread use in applications spanning from biology to molecular electronics and light harvesting to chemical catalysis. While many metalloporphyrins have been well characterized using the plethora of spectroscopic techniques available to the modern researcher, questions concerning important excited state dynamics and reactivity remain. Among these questions is: What is the connection between optically mediated electronic transitions and the spin dynamics and behavior of the centrally-ligated transition metal atoms and how can such a connection be controlled?

Over the past 40 years, spin crossover transitions in transition metal-complexed molecules have garnered intense interest.[30-36] It has been shown that varying temperature, pressure and exposure to light can lead to a transition of the spin of several different transition metal atoms ligated in spin crossover systems. The response of the magnetic moment of a molecule to its surrounding temperature is the most extensively studied mechanism for inducing an atomic spin state transition. At low enough temperatures, the spin state of the atom changes due to changes in the interactions between the metal atoms and their surrounding ligands.[37-40]

Within a specific range of temperatures, the magnetic moments of the spin crossover molecules also show hysteresis effects. That is, within this temperature range the magnetic moment of the molecule differs when temperature is decreased versus when it is increased. Researchers have proposed that this hysteresis represents an avenue tomolecular materials for information storage in analogy to memory systems based on the hysteresis loops of magnetization in response to applied magnetic fields.[33]

In the process of developing this molecular magnetic materials, researchers have found that within the temperature range over which hysteresis occurs optical interactions can couple differing spin states of ligated transition metal atoms via intersystem crossing relaxation pathways. As an example of one form of the coupling of optical and magnetic properties, light induced excited spin-state trapping (LIESST) was first demonstrated over 25 years ago in $Fe^{(II)}$ centered spin-crossover complexes.[35] In that form of LIESST, an optically allowed transition from the low-spin (LS) ground state produces the high-spin (HS) form of the $Fe^{(II)}$ via an intersystem crossing along non-radiative relaxation pathway. Some spin crossover molecules show that this intersystem crossing occurs on sub-ps time scales.[41] At low temperatures steady state light illumination at particular frequencies drives large amounts of population through the spin crossover transition. The long lifetime of the HS state produces a photostationary state.

LIESST and similar processes coupling the optical and magnetic properties of molecules containing transition metal are the basis for hundreds of studies of magneto-optical properties of spin crossover molecules and development molecular magneto-optical materials. However, researchers have also been left to finds ways to identify, characterize and scale-up synthetic protocols for embedding inorganic light-induced spin crossover structures into functional materials for magneto-optical technologies. Other molecular moieties may provide a better platform from which functional magnetic molecular materials are developed.

Since metalloporphyrins represent the basic units of many chemically and photo-chemically efficient molecular structures in biology, a great deal of effort has gone into developing materials for catalysis, light harvesting and molecular electronics based on metalloporphyrins. These materials range from supramolecular structures of photoinduced electron transfer,[42] to self-assembled thin films,[43] to Fe-porphyrin-like nanotube structures for oxygen reduction catalysis.[44] Recent research highlights the possibility of using metalloporphyrins for opto-magnetic technologies via selective photo-associative and dissociative channels.[45] Matching the suitability of metalloporphyrins for functional materials in technological devices with an ability to optically control their magnetic state may provide the necessary avenue to real-world magneto-optical materials for bio-sensing, solar energy conversion and information technology and storage.

In the work reported here resonance Raman (rR) and transient absorption (TA) spectroscopies are used to investigate the low temperature excited electronic dynamics and photochemistry of iron (III) tetraphenylporphyrin [$Fe^{(III)}$TPPCl]. Measurements were performed at room temperature and at low temperature, 77 K and 88 K. Raman spectra obtained with 413 nm Soret band excitation at 77K show both a solvent and power dependence that has yet to be elucidated in the literature[46-51]. The power dependence indicates photochemistry in which at least three products are formed. The formation of all three photoproducts is well described by a 2-photon model based on light absorption from an excited electronic state populated in the room temperature ultrafast transient dynamics of $Fe^{(III)}$TPPCl. Low temperature extension of the lifetime of this electronic state accounts for the difference in the photochemistry of this molecule at low and room temperatures.

Two features of the observed changes in the rR spectra are novel. First, the intensity of two high frequency toluene solvent vibrations shows a nonlinear dependence on the incident laser power. This nonlinear power dependence indicates a resonant enhancement likely due to exciplex formation between toluene and the photo-excited Fe-porphyrin. This phenomenon has been observed with iron porphyrins in similar, but distinctly more reactive solvent environments.[52]

Second, a two sets of a triplet of structure-sensitive Raman vibrations are consistent with the formation of a spin admixture [high-spin (HS) and low-spin (LS)] of six-coordinate $Fe^{(III)}$ species. The LS state is populated via a spin crossover transition through nonradiative relaxation of the initially populated six-coordinate HS $Fe^{(III)}$TPP. Both states likely include coordination of at least one toluene solvent molecule. According to the limits of the 2-photon model, the range of possible lifetimes of this mixture of spin states is 10 ms to 10 s. This result represents the first demonstration of coupling between the optical and magnetic properties of an iron-centered porphyrin molecule.

Experimental Methods

$Fe^{(III)}$TPPCl was synthesized using literature techniques.[48, 49] Purification was achieved by column chromatography on silica, eluted first with 100% CH_2Cl_2 to remove free H_2TPP and then +5% MeOH to elute $Fe^{(III)}$TPPCl. Metallated bands were combined and then washed twice with 1M HCl. The organic layer was dried with Na_2SO_4 and roto-vapped to dryness.

For resonance Raman scattering measurements, 1 mM solutions of $Fe^{(III)}$TPPCl were prepared in both 1:1 mixtures of toluene and DCM and neat DCM. Both solvents were used as received. These samples were pipetted into quartz EPR tubes and immersed in liquid nitrogen in a custom-made cold finger apparatus allowing the pump laser beam a clear window to the sample. Between gathered spectra, the sample EPR tube was moved both azimuthally and vertically such that a new portion of the sample was illuminated for each spectrum.

Resonance Raman (rR) spectra were taken at both the Soret and first vibrational overtone of the Q resonances (Q_v resonance for short). Wavelengths of 413.4 nm, 488.0 nm, and 514.5 nm from Spectra Physics continuous wave Ar-Kr ion laser were used for pumping these respective transitions. Scattered light was collected with a 2 inch diameter collection lens, collimated, passed through a Kaiser Optical Inc. holographic notch filter for rejection of both pump light and Rayleigh scattering and then free-spaced coupled into a Princeton Instruments Tri-Vista Raman Spectrometer fitted with a liquid nitrogen cooled CCD detector. The spectrometer was used in double additive mode with two 1800 gr/mm gratings for production of high-resolution spectra. Several scans, generally eight to twenty, were taken for each frequency window and laser power. Cosmic ray spikes were removed from the individual traces before averaging them together to produce the final spectra reported here.

Power dependent rR spectra excited with 413 nm laser light were collected in three spectral windows centered at: 350 cm^{-1}, 800 cm^{-1} and 1425 cm^{-1}. Reproducible changes predominantly occurred in the highest of these spectral windows. To reliably compare the changes in the rR scattering between the different energy windows, test spectra in the highest energy window were taken randomly in between the collection of spectra in the two lower energy windows. This was done to verify that systematic power dependent changes were still occurring for particular incident laser powers. While this done not allowed for quantitative comparison of the intensity of individual bands in different spectral windows, it does allow qualitative comparison of the any changes that occur in each of the individual windows as a function of power. Low temperature transient absorption (TA) measurements outlined in Chapter 4 were also used to aid in elucidating the observed photochemistry.

Experimental Results

The Raman spectrum of $Fe^{(III)}$TPPCl at 77 K in a 1:1 mixture of toluene and CH_2Cl_2 excited at 413.1 nm in the Soret band resonance are plotted in FIG. 5.1 for both high power (ca. 7 mW) and low power (ca. 1.5 mW) excitation.

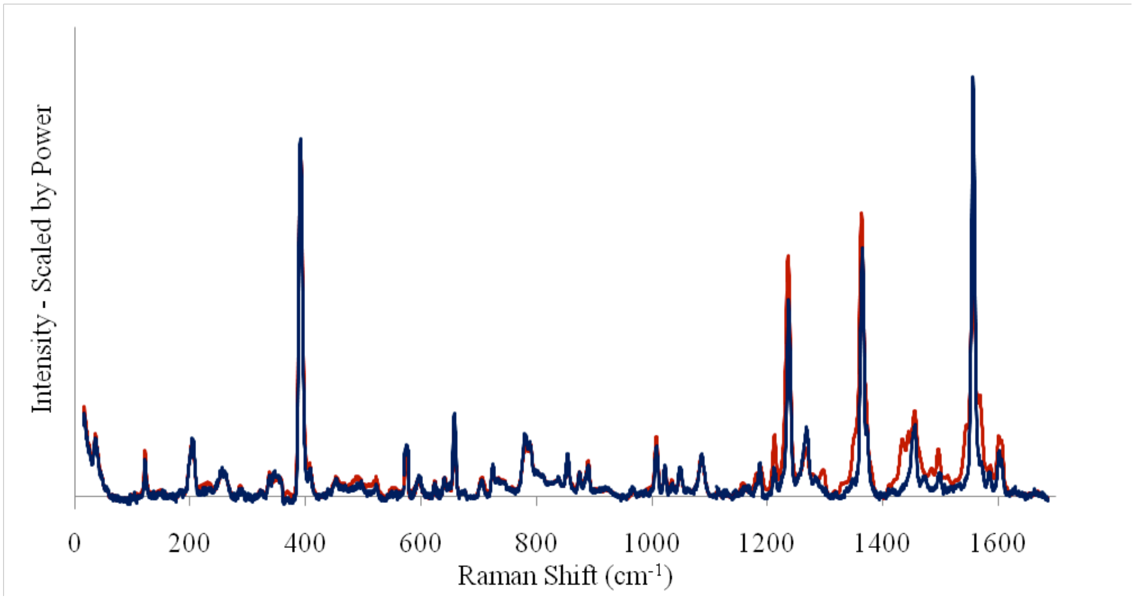

FIG. 5.1. Parallel polarized resonance Raman scattering spectrum of $Fe^{(III)}$TPPCl in 1:1 mixture of toluene and CH_2Cl_2 at 77 K excited at 413.14 nm for two differing incident laser powers ca. 1.5 mW (blue) and 7 mW (red).

The low power 413 nm Raman spectrum is dominated by the totally symmetric polarized transitions observed in the 454.5 nm spectrum reported previously.[50] There are some important differences however. The 1235 cm^{-1} ring breathing vibration is significantly more intense, several B_{2g} and/or B_{1g} transitions appear. Intensity is also observed in a large number of weak transitions, these may include fundamentals, overtones, and combination bands. Of particular note, intensity is observed in a 778 cm^{-1} mode assigned to the overtone of the 390 cm^{-1} Fe-N breathing mode. The increase in overtone or combination modes and the appearance of non-totally symmetric B_{1g} and B_{2g} vibrational modes are consistent with an excitation wavelength near the peak of a Jahn-Teller distorted Soret excited electronic state.[51]

Of more significance for the issues under consideration in this chapter is the strong power dependence in the Raman spectrum between 1100 cm^{-1} and 1700 cm^{-1}. This region is characteristically sensitive to the oxidation and spin state of the central iron atom and the overall charge of the porphyrin ring.[52-54] The power dependence observed with 413 nm excitation is shown in FIG. 5.2.

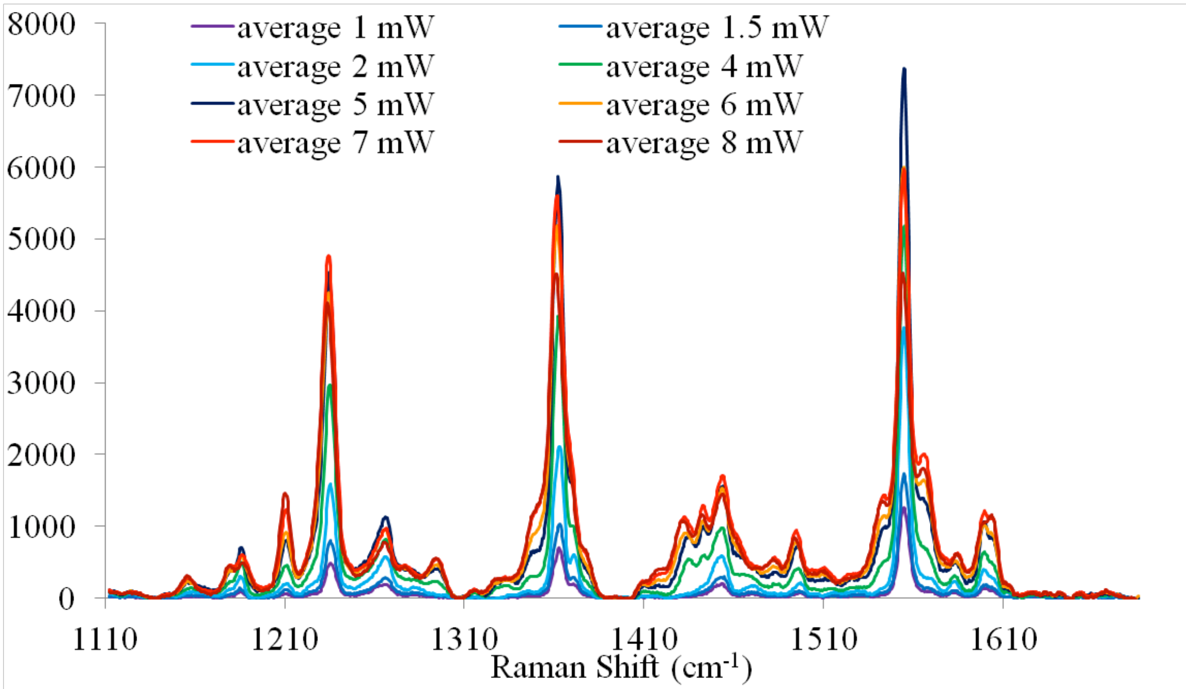

FIG. 5.2. The spectrum of Fe$^{(III)}$TPPCl in the 1:1 mixture of toluene and CH_2Cl_2 as a function of the intensity of the excitation laser. There is clear formation of a photoproduct as the laser intensity is increased.

The strongest peak at 1557 cm^{-1}, corresponding to a combination of interior carbon ring vibrations, decreases in relative intensity as the incident laser power is increased. Along either side of this vibration appear peaks that increase in intensity as the laser power is increased. In the 1425 cm^{-1} region of the spectrum a group of peaks appear as the laser power is increased. At lower energies, both the 1365 cm^{-1} and 1235 cm^{-1} peaks grow in intensity and shift to slightly lower frequency as the incident laser intensity is increased. There is a shoulder near 1350 cm^{-1} that grows in, as well as broadening of the peak centered at 1235 cm^{-1} as power is increased. A peak at 1296 cm^{-1} also appears as power is increased.

FIG. 5.3 shows the same spectral region of the Raman spectrum of $Fe^{(III)}$TPPCl with incident laser power varied over the same powers and cooled to the same temperature. These two spectra were taken in neat CH_2Cl_2, however, which crystallizes instead of forming a glass at LN2 temperatures.

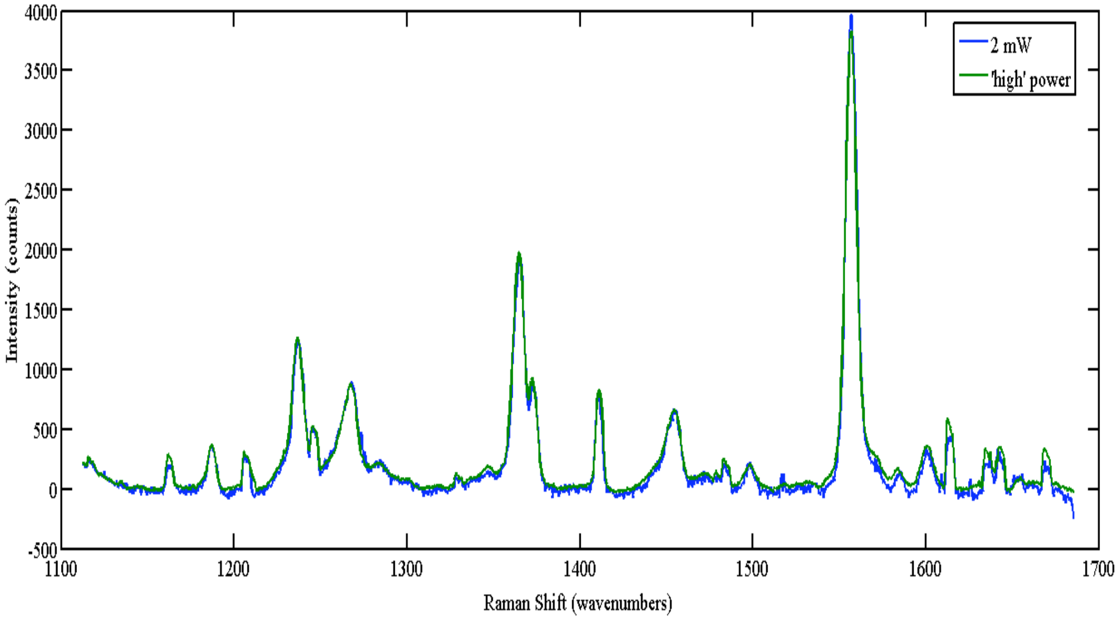

FIG. 5.3. High energy vibration region of the resonance Raman scattering from $Fe^{(III)}$TPPCl dissolved in neat CH_2Cl_2 excited at 413.1 nm at LN2 temperatures.

FIG. 3 clearly shows none of the same changes in the rR spectra seen in the 1:1 mixture of toluene and DCM as a function of the incident laser power.

Power dependent resonance Raman spectra were also collected from the sample dissolved in the 1:1 mixture of toluene and CH_2Cl_2 under the same experimental conditions in the same spectral region, but excited on the Q_v resonance at both 488.0 nm and 514.5 nm. FIG. 5.4 shows the resonance Raman scattering for two 488.0 nm incident laser powers of 50 mW and 350 mW.

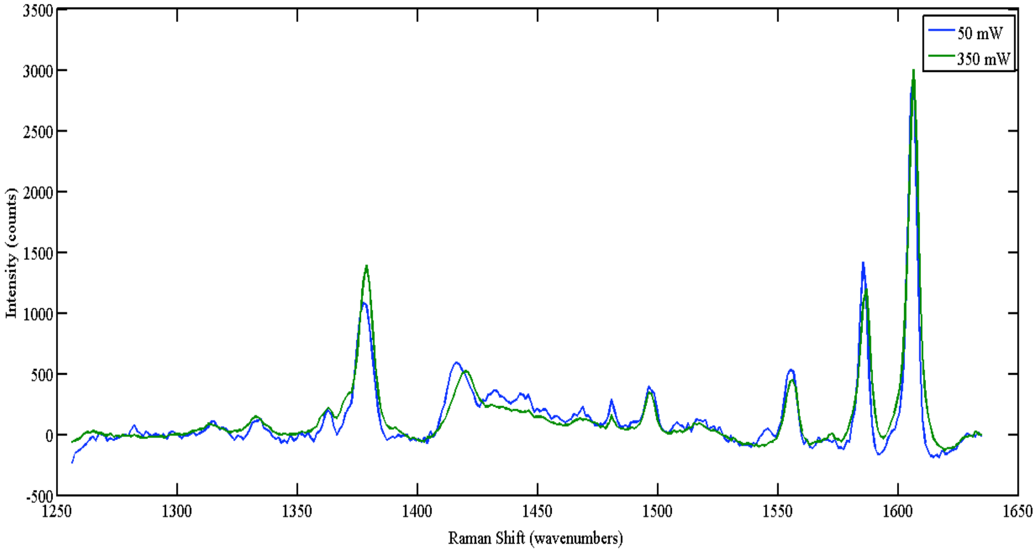

FIG. 5.4. Power dependent resonance Raman spectra of Fe$^{(III)}$TPPCl excited on the Q_v resonance at 488.0 nm in 1:1 mixture of toluene and CH_2Cl_2 at LN2 temperatures.

FIG. 5.5 shows the resonance Raman scattering excited at 514.5 nm for three incident laser power of 30 mW, 110 mW and 250 mW.

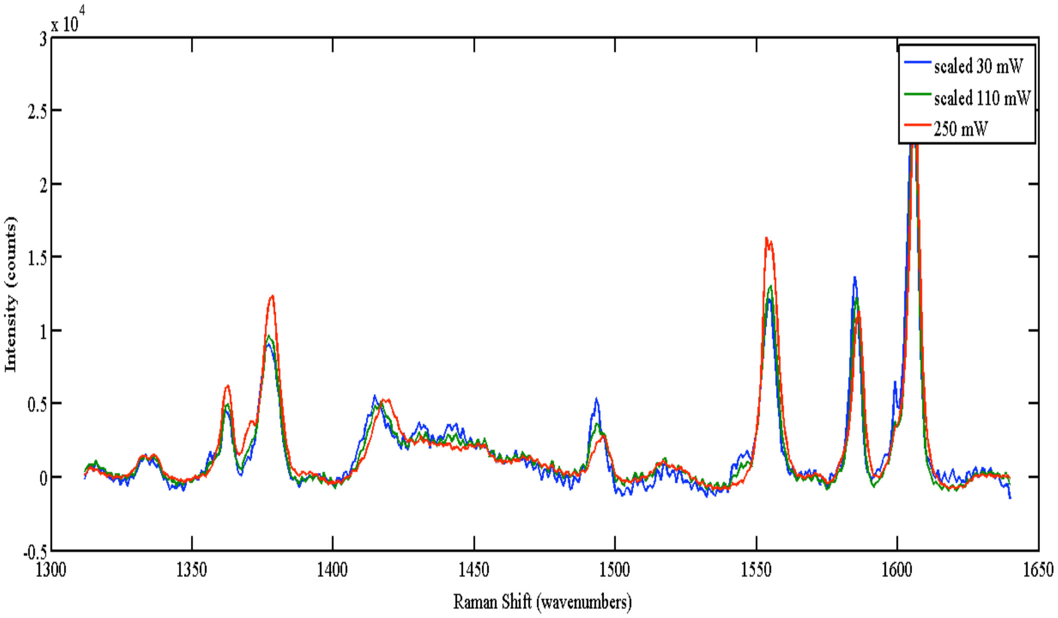

FIG. 5.5. Power dependent resonance Raman spectra of Fe$^{(III)}$TPPCl excited on the Q_v resonance at 514.5 nm in 1:1 mixture of toluene and CH_2Cl_2 at LN2 temperatures.

The spectra collected at different powers were scaled to the intensity of the solvent toluene peak at 1610 cm^{-1} in the highest incident power spectrum for both excitation wavelengths. The spectra excited at both 488.0 and 514.5 nm do not show any of the same power dependence as the spectra excited at 413.1 nm. There are some qualitative changes in spectra as seen in the CH_2Cl_2 solvent peak at 1410 cm^{-1}. We believe these changes occur due to local heating effects in the low temperature glass at the highest laser fluences.

As oxygen-containing molecules have been shown to coordinate to the central iron atom in $Fe^{(III)}$TPPCl,[5] control measurements using a sample washed with acetone were taken to observe changes in shifts of characteristic structure-sensitive bands in the rR spectra. FIG. 5.6 shows the measured rR spectrum of $Fe^{(III)}$TPPCl dissolved in a 1:1 mixture of toluene and DCM when the sample EPR tube was washed with acetone before sample deposition.

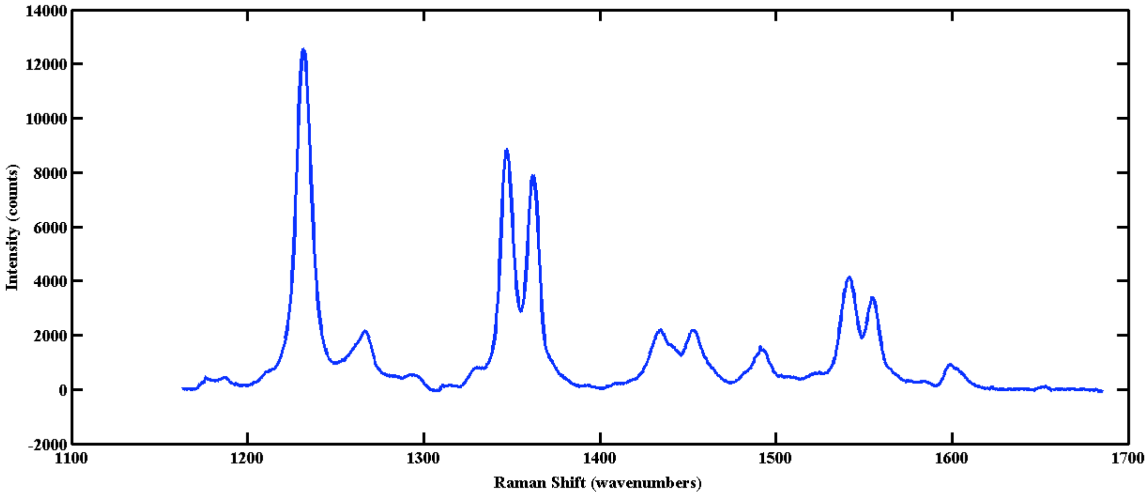

FIG. 5.6. Resonance Raman spectrum of $Fe^{(III)}$TPPCl dissolved in 1:1 mixture of toluene and DCM in acetone-washed EPR tube excited at 413.1 nm at LN2 temperatures.

A qualitatively different rR spectrum is measured in this case showing changes that are characteristic of a five-coordinate, high-spin $Fe^{(II)}$ species, as discussed below.

The photoproduct observed in the data plotted in FIG.s 5.1 and 5.2 does not appear to be permanent. When the intensity of the laser is reduced while remaining focused on the same area of the sample the spectrum recovers to the spectrum obtained with low power illumination of a fresh area of the sample. In addition the features in the spectrum are not a function of the length of the illumination time. Thus the data reflects formation of a photostationary mixture of ground state $Fe^{(III)}$TPPCl and a photoproduct state under steady state illumination.

Resonance Raman spectra of five-coordinate, $Fe^{(III)}$ porphyrins photoproducts following Soret band excitation have been reported in the literature.[4, 5, 55-63] These have been attributed primarily to iron reduction from oxygen or nitrogen-containing solvent molecules. The features observed in the presence of toluene, however, are qualitatively and quantitatively different from those reported in the literature in the presence of oxygen or nitrogen.

The power dependent spectra in the 1:1 mixture of toluene and CH_2Cl_2 can be decomposed into two different species associated spectra. A singular value decomposition (SVD) algorithm was used to accomplish the separation of the spectra:[64]

$$\mathbf{A} = \mathbf{U} \cdot \mathbf{S} \cdot \mathbf{V}^{\mathbf{T}} = \mathbf{U}' \cdot \mathbf{V}^{\mathbf{T}} \tag{5.1}$$

where the data matrix A containing the Raman spectra as a function of power is decomposed into U, a matrix of the basis spectra, S, a diagonal matrix containing the singular values, and V^T, a matrix containing the basis amplitude vectors. Only two of the basis spectra contained significant signal, while the remaining vectors were predominantly noise. The two basis spectra obtained from the SVD analysis are rotated to obtain physically meaningful spectra under the assumption that the spectrum obtained at the lowest power represents the linear resonance Raman spectrum of $Fe^{(III)}$TPPCl and one of the two basis vectors should correspond to this species.

$$\mathbf{F} = \mathbf{U}' \cdot \mathbf{P}^{\mathbf{T}} \tag{5.2}$$

P is a 2×2 rotation matrix and the matrix F contains the resulting basis spectra. The two basis spectra are shown in FIG. 5.7. The spectrum labeled F_1 is essentially the spectrum obtained with 1 mW excitation while the spectrum labeled F_2 is a difference spectrum representing the conversion of $Fe^{(III)}$TPPCl into the photoproduct.

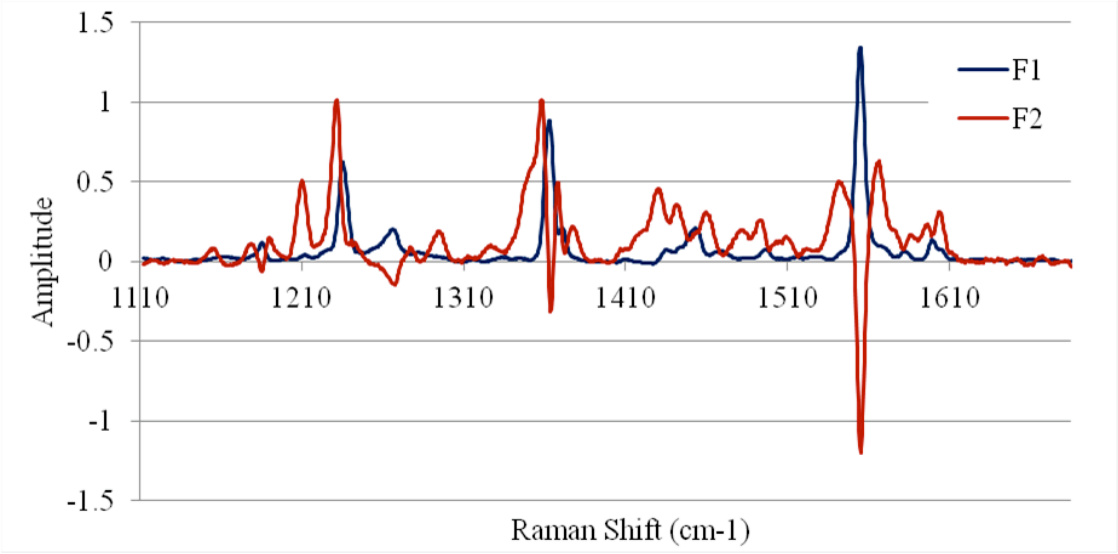

FIG. 5.7. Spectral basis vectors obtained from the singular value decomposition. The vector F_1 from eqn. (2) is the spectrum obtained with 1 mW excitation. The spectrum F_2 is a difference between the ground state spectrum and the photoproduct spectrum.

The difference spectrum F_2 can be used to estimate the photoproduct spectrum, S_{prod} by adding the appropriate amount of the ground state spectrum F_1 back into F_2.

$$S_{prod} = F_2 + \alpha F_1 \tag{5.3}$$

There are two clear limits constraining the value for α. (1) The product spectrum must be everywhere positive. Therefore the minimum possible value for α is the value that makes this true. (2) The spectrum obtained at the highest power used in these experiments cannot be more than 100% photoproduct. Therefore the maximum value for α is obtained by assuming that the spectrum obtained at the highest power is entirely due to the photoproduct. These limits for the photoproduct spectrum are compared in FIG. 5.8.

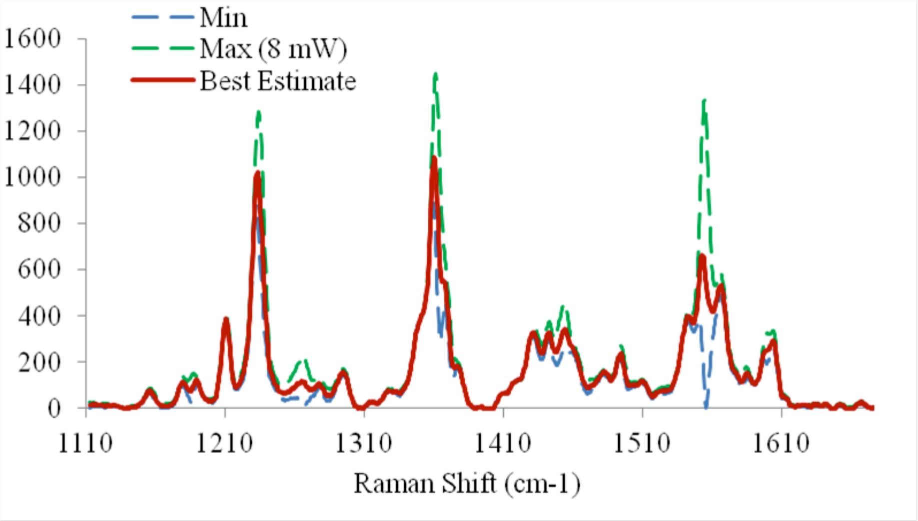

FIG. 5.8. The photoproduct spectrum derived from the SVD analysis of the power dependent data. The spectrum plotted in blue uses the minimum α required to ensure that the spectrum is everywhere positive. The spectrum plotted in green assumes unit conversion to photoproduct in the Raman spectrum obtained with 8 mW excitation. The spectrum plotted in red is an intermediate estimate for the photoproduct.

Most of the Raman bands observed in FIG.s 5.2, 5.7, and 5.8 are attributed to either $Fe^{(III)}$TPPCl or the photoproduct/s. There are a few weak transitions, however, which arise from the 1:1 toluene:DCM solvent. There are a few weak transitions, however, which arise from the 1:1 toluene:CH_2Cl_2 solvent. Of particular note, the band at 1210 cm^{-1} is a totally symmetric phenyl-methyl stretching mode of toluene. When deuterated toluene (C_7D_8) is used in the solvent mixture this band shifts to 1174 cm^{-1} as shown in Figure 6. This band is relatively well separated from both the $Fe^{(III)}$TPPCl vibrational bands and the photoproduct bands. The totally symmetric C=C stretching band observed at 1605 cm^{-1} in toluene and 1583 cm^{-1} in deuterated toluene is also observed in the photoproduct spectrum. While the resonance enhancement of the $Fe^{(III)}$TPPCl ground state and the photoproduct are not identical, the intensity of the solvent band should increase linearly with laser power. However, if solvent molecules participate in a photochemistry, some Raman-active solvent bands become resonantly enhanced. Bands assigned to ligated solvent molecules have been observed in resonance Raman spectra of iron porphyrin compounds when the excitation wavelength is resonant with a charge transfer band.[47, 52] The toluene bands at 1210 cm^{-1} and 1605 cm^{-1} in the product spectrum demonstrate one of two distinct possibilities: 1) toluene acts as a ligand to the iron porphyrin in the photoproduct or 2) the resonance enhancement of the photoproduct at 413 nm is approximately one fifth that of Fe$^{(III)}$TPPCl. This decrease in the resonance enhancement results in an increase in the relative intensity of the solvent bands. These possibilities will be discussed in greater detail in the discussion section below.

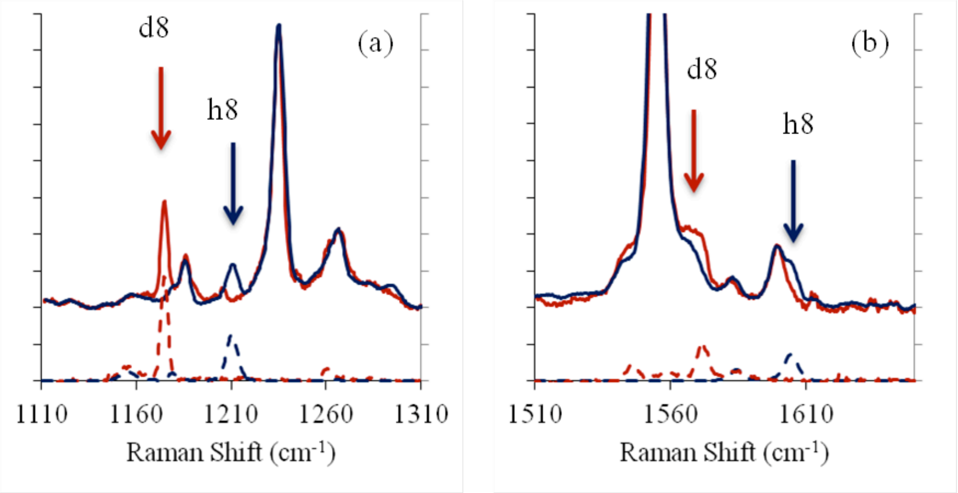

FIG. 5.9. (a) Comparison of the spectrum of Fe$^{(III)}$TPPCl obtained with 4 mW excitation toluene (blue) or deuterated toluene (red) in the solvent. The totally symmetric phenyl-methyl stretching mode is indicated with the arrows. The solvent spectra are offset below the Fe$^{(III)}$TPPCl spectra, 1:1 CH_2Cl_2: perdeuterotoluene (red dashed) or CH_2Cl_2:toluene (blue dashed). (b) Comparison of the Fe$^{(III)}$TPPCl and solvent spectra around the 1557 cm^{-1} band. Solvent bands are also observed in this spectral region although they are not well separated from the Fe$^{(III)}$TPPCl bands.

Discussion

1. *Model for the Power Dependent Raman Spectrum*

The resonance Raman scattering from Fe$^{(III)}$TPPCl in a 1:1 mixture of toluene and CH_2Cl_2 clearly shows effects due to the presence of one or more long-lived photoproduct states at low temperatures. From Chapter 4, the difference spectra for different pump-probe time delays in low absorption transient absorption measurements also show distinct changes consistent with photochemistry, as well as long-lived (τ>500 ps) excited electronic states. Therefore, the two measurements provide information about the nature of the product formed and the mechanism of its formation in a low temperature glass environment.

There are three key observations. First, the power dependent rR scattering at low temperature shows a significant solvent dependence. In the poly-crystalline CH_2Cl_2 environment at 77 K, the rR spectrum of $Fe^{(III)}$TPPCl shows no discernible power dependence. In the presence of toluene, however, several power-dependent features appear in the high-energy spectral window of 1150-1600 cm^{-1}. This dependence on toluene seems to imply a role for solvent molecules in the formation of the photoproduct/s giving rise to the power-dependent scattering.

Second, the appearance of triplets of polarized peaks near 1555 cm^{-1} and 1445 cm^{-1} along with shoulders to both the higher and lower energy sides of the strong peak at 1363 cm^{-1} implies the existence of at least three distinct chemical products. The SVD analysis of the power dependent spectra was able to efficiently project the data onto only two components. This leads to a separation into a component that depends approximately linearly on the laser power (the ground state of $Fe^{(III)}$TPPCl) and a component that shows a uniform nonlinear dependence on laser power. There is no evidence for additional high order processes. Thus all products are produced in comparable yield from the photoexcitation process.

Third, rR scattering from both the Soret and Q_v transitions provides a clear distinction between the ability of each excitation frequency to produce the photoproducts. While the $\pi\pi^*$ Soret transition excited at 413 nm produces a power dependent rR spectrum with incident laser powers between 1 and 10 mW, much larger power increases at 488 nm or 514 nm excitation produce no change in the observed spectra. Large enough laser powers at 488 nm and 514 nm were used to produce significantly more excited states than with 413 nm excitation.

These observations lead to two possible models for the photochemistry of $Fe^{(III)}$TPPCl: a 1-photon model or a 2-photon model. In the case of a 1-photon model, the excitation of the ground state forms an excited state that either returns to the ground state of the compound or produces the observed products. Alternatively, in the 2-photon model the excitation of the ground state forms of an excited state that absorbs a second photon to produce a state from which the observed products are formed. These two models are sketched in FIG 5.10.

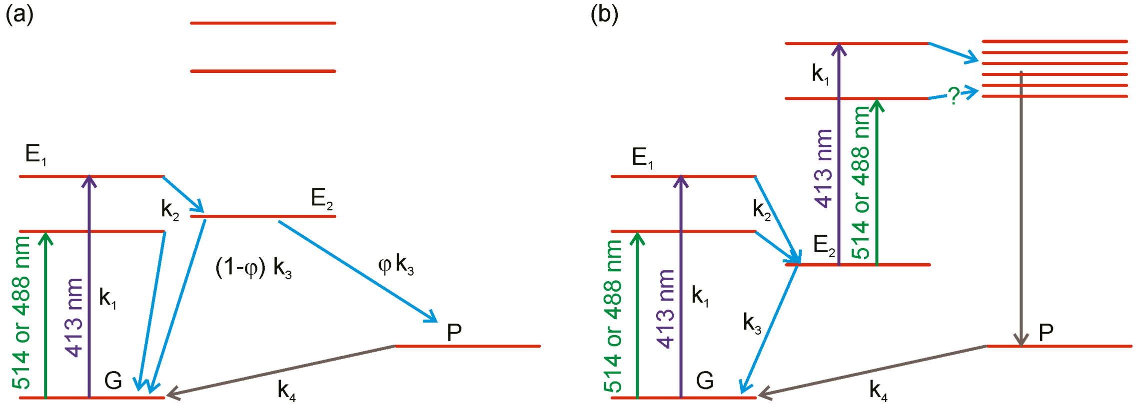

FIG. 5.10. Schematic diagrams for the one-photon (a) or two-photon (b) photochemistry of Fe$^{(III)}$TPPCl in a 1:1 mixture of CH_2Cl_2 and Toluene.

The low temperature TA measurements also provide useful information. The difference spectrum observed at time delays of 50 and 500 ps demonstrate formation of a long lived excited state with a lifetime on the order of 1 ns or longer. This excited state has an absorption spectrum with a slightly red-shifted Soret band, but displaying structures and intensities otherwise similar to that of the ground state. This difference spectrum corresponds to formation of the state labeled "E_2" in FIG. 5.10. The state "P" is either produced directly following one-photon excitation at 413 nm or following two-photon excitation at 413 nm, first by the ground state and then by an excited state. The long-lived difference spectrum from the low temperature TA measurements exhibits a decrease in the intensity on the red-side of the Soret band and an increase in the intensity of the Q_v band between 490 nm and 530 nm.

The data in FIG 5.2 can be fit to a linear combination of the ground state (GS) and product state (PS) Raman spectra shown in FIG. 5.8. Without knowledge of the relative Raman enhancement of each species it is impossible to precisely analyze the photochemical mechanism quantitatively. Despite this limitation, the observed spectra place strict limits on the range of acceptable decompositions.

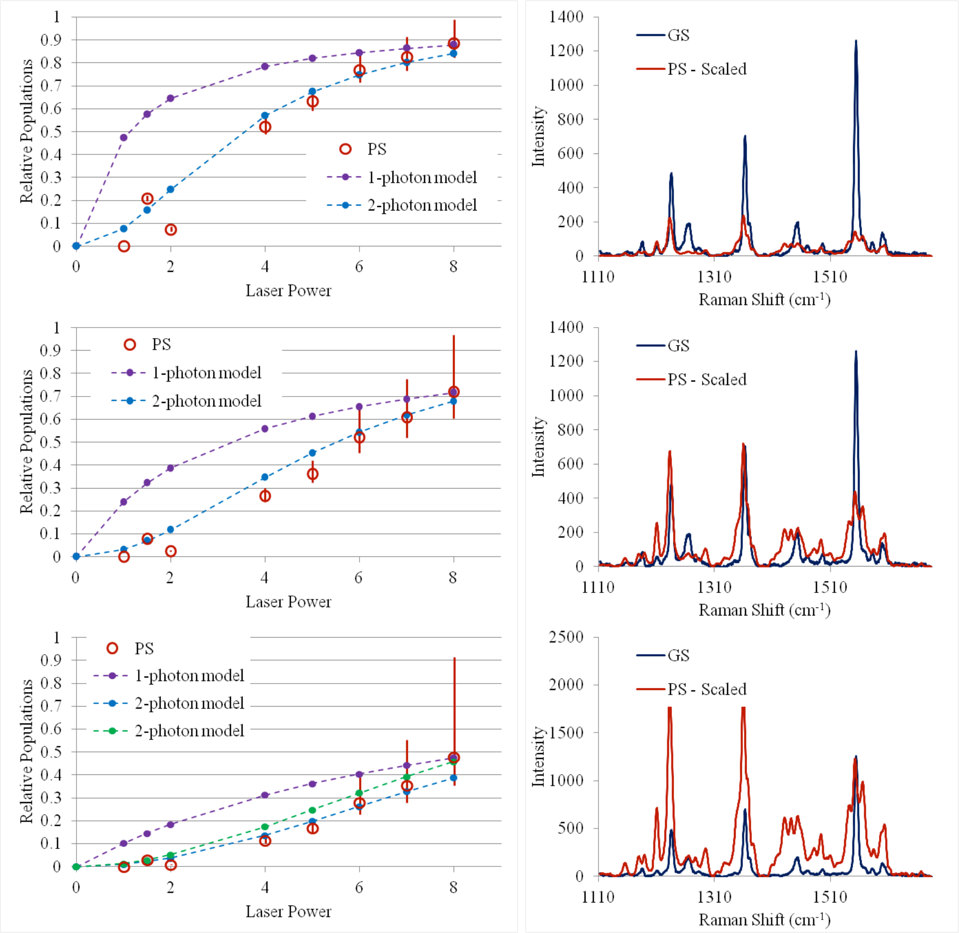

FIG. 5.11. Comparisons of the basis spectra for the ground state and photoproduct (right) and the population as a function of laser power (left) for a range of relative resonant enhancements. The upper row assumes that the toluene bands are not resonantly enhanced in the product spectrum. This provides a lower limit for the intrinsic intensity of the photoproduct spectrum. The middle row assumes that the integrated intensity of the 1557 cm^{-1} ν_2 region is constant. The intensity of the product spectrum is approximately a factor of three larger than in the top row. The bottom row assumes an additional factor of three increase in the intensity of the photoproduct spectrum.

The populations of the states in FIG. 5.10 can be modeled using a master equation approach to the dynamics. For the 1-photon model:

$$\dot{n}_G(t) = -k_1 n_G(t) + k_3\left(1-\phi\right) n_{E_2}(t) + k_4 n_P(t), \tag{5.4a}$$

$$\dot{n}_{E_1}(t) = k_1 n_G(t) - k_2 n_{E_1}(t), \tag{5.4b}$$

$$\dot{n}_{E_2}(t) = k_2 n_{E_1}(t) - k_3 n_{E_2}(t), \tag{5.4c}$$

$$\dot{n}_P(t) = \phi k_3 n_{E_2}(t) - k_4 n_P(t). \tag{5.4d}$$

The rate constant k_1 describes production of the electronic state excited from the ground state. This rate constant depends on the power of the incident laser beam (P), the excitation frequency ($\nu = c/\lambda$), and number of molecules in the excited volume (N). The number of molecules in the excited volume depends in turn on the concentration of the sample (C) and the effective volume (V), determined by the extinction coefficient at the excitation wavelength and the size of the focus.

$$k_1 = \frac{r_{ph}}{N} = \frac{P}{h\nu\left(CN_AV\right)} \tag{5.5}$$

From Chapter 4, the rate constant k_2 for decay of the initially excited state at room temperature is ca. 1 ps^{-1}. Since our low temperature transient absorption measurements from Chapter 4 show that the initially excited state is not populated at 50 ps probe delay, we know k_2 must be greater than 0.02 ps^{-1} at 88K. However, any rate constant larger than 0.02 ps^{-1} still models the data well.

At low temperature, the rate constant for decay of E_2 is $k_3 \leq 1$ ns^{-1}. The rate constant k_4 for decay of the product state must less than 1000 s^{-1}, but $\geq\sim 0.1$ s^{-1} since steady state is reached in the Raman measurements with an integration time on the order of minutes. However, the amount of product does not depend on the precise integration time. There is a trade-off between the quantum yield, φ, for formation of the product and the rate constant for decay of the product. For this model it is assumed that $k_4 = 0.1$ s^{-1} and the quantum yield of product formation, φ, is 10^{-4} to 10^{-5}. If k_4 is larger, the quantum yield must be larger as well to achieve the same steady state population.

As illustrated in FIG. 5.11, the 1-photon model does not fit the observed power dependence. The amount of photoproduct population formed in this model increases more quickly than the observed data. This model only agrees with the data at the highest incident power where most of the population has been driven into the product state.

The 2-photon model with photoproduct formation from absorption from the excited electronic state E_2 , however, does fit the observed power dependence reasonably well. In this case we assume that the rate constant for absorption from E_2 is the same as that for absorption from the ground state. This approximation is justified by the small ΔA observed in the transient absorption measurements for this state. Using the 2-photon model, the rate equations for the populations are:

$$\dot{n}_G(t) = -k_1 n_G(t) + k_3 n_{E_2}(t) + k_4 n_P(t), \tag{5.6a}$$

$$\dot{n}_{E_1}(t) = k_1 n_G(t) - k_2 n_{E_1}(t) \tag{5.6b}$$

$$\dot{n}_{E_2}(t) = k_2 n_{E_1}(t) - k_3 n_{E_2}(t) - k_1 n_{E_2}(t) \tag{5.6c}$$

$$\dot{n}_P(t) = k_1 n_{E_2}(t) - k_4 n_P(t) \tag{5.6d}$$

Similarly to the 1-photon model, k_2 in the 2-photon model must be greater than 0.02 ps^{-1} based on our measurements, but the model's fit to the data is not sensitive to its precise value above that threshold and below 1 ps^{-1}. The rate constant, k_4, for decay of the product state, must be less than 1000 s^{-1} and greater than ≥~0.1 s^{-1}. Assuming that k_4 = 0.1 s^{-1} (i.e. lifetime = 10 s) the rate constant k_3 for decay of E_2 is adjusted to match the observed data. The 2-photon fits in FIG. 5.11 find k_3 = 0.125 to 0.5 ns^{-1} making the lifetime of E_2 is between 2 and 8 ns. If the lifetime of the product is smaller, the lifetime of E_2 must be larger to achieve the same steady state population. This model fits the data quite well with a physically reasonable lifetimes ranging from τ_{E2} = 1ns, τ_P = 10 s to τ_{E2} = 1 μs, τ_P = 10 ms. Time-dependent absorption measurements outside the time range available in our laboratory would be required to determine the lifetimes more precisely.

The model for photolysis put forth in FIG. 5.10 and Eqns. 5.6 requires the assumption that the excited state responsible for product formation is not accessible with 488 nm or 514 nm excitation. If the state is accessible, the 250-350 mW laser power used in these experiments should have produced substantial photoproduct, with yields similar to those observed with 8 mW of 413 nm. Since the photochemical pathways following 1-photon excitation at room temperature are independent of excitation wavelength, and the difference spectra observed at low-temperature are consistent with the room temperature difference spectra, it seems likely that the difference is in photochemical channels accessible following excitation of population in E_2. Excitation at 413 nm provides access to a reactive state not available following 488 nm or 514 nm excitation.

The lack of an appearance of a difference spectrum in the early times after the arrival of the 400 nm pump pulse distinct from those observed at rm. temperature necessitates that the quantum yield of photoproduct formation be very low. In order to measure a photoproduct with very low quantum yield, however, the lifetime of the product state must be on the order of 100's of us to 10's of ms. While the lifetime of this state was not directly measured using TA, the ability of the 2-photon model to explain the relative population of the ground and product states in the observed data with specific values for these lifetimes is informative. As seen in Chapter 4, a qualitatively distinct difference spectrum from any of the rm. temperature species or decay associate spectra is measured at time delays close to 1 ms. That the spectral features of this difference spectrum are of comparable magnitude as those of the early time difference spectra also implies that the population in this long-lived state/s must be comparable. The population in this state/s may actually be larger based on the difference in the resonant enhancement observed in the rR measurements. Therefore, it seems reasonable to conclude that the quantum yield of photoproduct formation is very small, likely smaller than 1%. As discussed above, a quantum yield below 1% is also consistent with the predictions of the 2-photon model.

While the low temperature transient absorption measurements of Chapter 4 show difference spectra distinct from those in the room temperature measurements, comparison of the mechanism producing that state to the mechanism dominating the power dependent rR spectra is difficult. As noted above, the 2-photon model predicts the rR product is formed from absorption by an excited electronic state populated at time delays of up to 1 ns after the initial excitation of the ground electronic state. In the time-domain measurements, a second pump pulse is not incident on the sample 1 ns after the initial excitation. Also, since the probe is measuring changes in absorption at time delays of ~1 ms, it will not excite a state with a lifetime of 1-10 ns relative to the arrival of the pump. Therefore, direct 2-photon absorption by the ground state has to account for any photochemistry occurring in the TA measurements at low temperature. Without a time-resolved Raman measurement of the products of that chemistry, it is difficult to say that the same state is formed in both measurements. Nonetheless, direct, ground state 2-photon to the formation of either the same or a distinct product state indicates the reactive nature of the highly excited states of this metalloporphyrin at low temperature in this solid-state environment.

The data help provide clear picture of the parameters for photoproduct formation. (1) The product state forms only in the presence of toluene. (2) Product is formed below 100 K through absorption by an excited electronic state that is populated during the room temperature ultrafast dynamics of the molecule. This states lives between two and three orders of magnitude longer below 100 K. The products do not form via absorption from this state with 488 nm, 514 nm or 520 nm excitation. No measurable amount of product forms when the ground state is excited on the Q_v resonance even under very high laser power conditions. (3) The quantum yield of formation is very low, likely below 1%, but the lifetime of the product is very long. This allows enough electronic population to build up in the product state to create a photo-stationary state. This information must now be used to provide a clearer picture of the identity of the product state formed.

While the low temperature transient absorption measurements of Chapter 4 show difference spectra distinct from those in the room temperature measurements, comparison of the mechanism producing that state to the mechanism dominating the power dependent rR spectra is difficult. As noted above, the 2-photon model predicts the rR product is formed from absorption by an excited electronic state populated at time delays of up to 1 ns after the initial excitation of the ground electronic state. In the time-domain measurements, a second pump pulse is not incident on the sample 1 ns after the initial excitation. Also, since the probe measure changes in absorption at time delays of ~1 ms, it will not excite a state with a lifetime of 1-10 ns relative to the arrival of the pump. Therefore, direct 2-photon absorption by the ground state has to account for any photochemistry occurring in the TA measurements at low temperature. Without a time-resolved Raman measurement of the products of that chemistry, it is difficult to say that the same state is formed in both measurements. Nevertheless, direct, ground state 2-photon to the formation of either the same or a distinct product state indicates the reactive nature of the highly excited states of this metalloporphyrin at low temperature in this solid-state environment.

2. *Analysis of the Photoproduct Raman Bands*

The Raman spectra of the photoproduct plotted in Figure 5 exhibit at least three distinct triplets of bands in the spectra region between 1100 cm^{-1} and 1700 cm^{-1}. These features are summarized in Table 1 and compared with the same bands in the spectrum of the Fe$^{(III)}$TPPCl ground state.

In contrast to the characteristic changes observed in the high frequency region, there are no substantive changes in the low frequency region or the mid-frequency region (see FIG. 5.1). In particular, there is no shift in the frequency of the ν_8 totally symmetric Fe-N breathing vibration at 392 cm^{-1} as the incident laser power is increased (Raman bands here and in what follows are numbered according to the convention in Paulat *et al.*[55]). The relative intensity may decrease slightly, but no other change is observed.

Table 5.1. Summary of vibrational bands undergoing significant changes in frequency or intensity in the photoproduct. A selection of comparisons with analogous compounds is also included.

Spin		Characteristic Strongly Polarized Vibrations (a_{1g})				Potentially Depolarized Vibrations (b_{1g}/b_{2g})	
		ν_1(cm^{-1})	ν_2(cm^{-1})	ν_4(cm^{-1})	ν_8(cm^{-1})	ν_{12}/ν_{27}(cm^{-1})	ϕ_5'(cm^{-1})
hs	Ground State Fe$^{(III)}$TPPCl	1452	1556	1363	392	1264/1278	1494
	Product Spectrum A	1454	1566	1372		1294	1508
	Product Spectrum B	1442	1553	1359	392	1276	1494
	Product Spectrum C	1431	1542	1349		1264	1481
ls	$[Fe^{(III)}TPP(ImH)_2]^+ Cl^-$	1459	1561	1365	(390)[a]		1501
	$[Fe^{(III)}TPP(N\text{-}MeIm)_2]^+Cl^-$ [b]		1564	1369	390		
hs	$[Fe^{(III)}TPP(DMSO_2]^+ Cl^-$	1438	1541	1356			1486
	$[Fe^{(III)}TPP(DMSO_2]^+ Cl^-$ [a]		1550	1360	391		
ls	$[Fe^{(II)}TPP(ImH)_2]$	1448	1557	1354	(382)[a]		1497
	$[Fe^{(II)}TPP(py)_2]$ [a]		1558	1360	388	1265	1484
hs	$[Fe^{(II)}TPP(2\text{-}MeIm)]$	1431	1538	1341	(372)[a]		(1484)[a]
	$[Fe^{(II)}TPP(1,2\text{-}DiMeIm)]$ [b]		1539	1344	373		

Unless otherwise specified comparison frequencies from Parthasarathi *et al.* JACS 1987[52]. Others (a) – Burke *et al.* JACS 1978[48]; (b) – Oshio *et al.* Spectrochim. Acta A 1984.[53] The spin designation indicates whether the compound is high-spin (hs) or low-spin (ls). Im = imidazole, MeIm = methylimidazole, DMSO = dimethylsulfoxide, py = pyridine.

The Raman spectroscopy and photochemistry of metalloporphyrins have been studied extensively over the years.[4,9,56,58,59,61-70] The vibrational bands exhibiting substantive changes in the photoproduct spectrum reported here are well known to correlate with the oxidation and spin state as well as the identity of the ligand in the iron atom's axial position. In response to a change in oxidation state, spin state [low-spin (LS) and high-spin (HS)] or ligation the metal atom may move in or out of the plane of the porphyrin ring, depending on the population of the different d-orbitals and the change the character of the bonding to the porphyrin ring. The motion of the metal atom is correlated with changes in the size of the porphyrin core. These changes cause characteristic shifts in the specific totally symmetric Raman bands of the porphyrin ring. The bands observed in the photoproduct resonance Raman spectrum can be placed into context of these characteristic shifts with a brief survey of the relevant literature.

A. A brief survey of the literature.

A key study by Parthasarathi *et al.* compiled Raman frequencies for several iron porphyrin compounds and correlated these with the core size around the iron atom as determined by x-ray crystallography.[59] When imidazole is added to $Fe^{(III)}TPPCl$ a six-coordinate LS $[Fe^{(III)}TPP(ImH)_2]^+ Cl^-$ complex is formed. The porphyrin center to pyrrole N distance (C_t –N) distance shrinks from 2.019 Å to 1.989 Å and the vibrational frequencies increase as shown in Table 1. Similar vibrational frequencies are reported for $[Fe^{(III)}TPP(N\text{-}MeIm)_2]^+ Cl^-$.

Reduction of the iron atom to $Fe^{(II)}$ causes the iron atom to increase in size and shift more into the plane of the porphyrin ring.[5,9,56,58-60,66,69] The expansion of the ring shifts the characteristic ν_1, ν_2, ν_4 and ν_8 vibrations to lower energy. Five-coordinate HS $Fe^{(II)}$ compounds can be formed with 2-methylimidazole or 1,2-dimethylimidazole ligands. For the $Fe^{(II)}TPP(2\text{-}MeImH)$ compound the C_t –N distance expands to 2.045 Å and the characteristic vibrational frequencies red-shift by about 20 cm^{-1}.

The six-coordinate LS $Fe^{(II)}$ compounds are formed with a variety of nitrogen containing ligands including N-methylimidazole, pyridine, piperidine, and γ-picoline. These compounds have intermediate C_t –N distances (1.997 Å for N-MeIm) and the observed vibrational frequencies are in the same range as those observed for the high-spin $Fe^{(III)}$TPPCl compound.[58-60]

The structure sensitive bands of several six-coordinate HS $Fe^{(III)}$ porphyrins have also been studied.[59,71-73] In the case of $(DMSO)_2Fe^{(III)}$TPP, the C_t –N distance increases, relative to the ground state structure of $Fe^{(III)}$TPPCl, to 2.045 Å.[59] This increase causes the structure sensitive rR bands shift down in energy, as seen in Table I.

In addition to the characteristic shifts observed for the porphyrin breathing modes of these compounds, solvent Raman bands may show enhancement in the event of exciplex formation with a metalloporphyrin. Spiro and Burke observed resonance enhancement of vibrational bands assigned to γ-picoline and pyridine ligands in the six-coordinate [$Fe^{(II)}$"XP"$(py)_2$] and [$Fe^{(II)}$"XP"$(pic)_2$] upon excitation at 457.9 nm where XP is mesoporphyrin IX or tetraphenylporphyrin.[52,58] The 1599 cm^{-1} and 1215 cm-1 bands of pyridine strongly enhanced while other ligand modes exhibit a weaker resonance enhancement.

Finally, we note that Evans et al. used x-ray crystallography to demonstrate the ability of benzene, toluene, and p-xylene to be weak ligands to the hard metal in $[Fe^{(III)}(TPP)]^+$.[74] $Fe^{(III)}$(TPP)Y with Y an appropriately chosen weakly coordinating anion, was dissolved in the aromatic solvent and crystallized. Crystal forces allowed biasing of the equilibrium forming crystals of $[Fe^{(III)}(TPP)(arene)]^+$ Y^-. These workers also demonstrated heptane coordination to a carefully protected $Fe^{(II)}$ porphyrin compound.[75]

B. Assignment of the Product States

Given the information summarized above we can assign the triplets of bands observed in the photoproduct spectrum to three distinct $Fe^{(III)}$TPP complexes, one corresponding to the red-shifted components of the major bands (Product A), one corresponding to the blue-shifted components (Product C), and one corresponding to the components near, but not identical to, the ground state $Fe^{(III)}$TPPCl bands (Product B).

The low frequency components of the photoproduct ν_2 (1541 cm^{-1}) and ν_4 (1349 cm^{-1}) bands corresponding Product A to are consistent with shifts that are observed following chemical or photochemical formation of a five-coordinate HS $Fe^{(II)}$ species accompanied by changes in ligation of the Fe. However, the absence of significant change in the low frequency region of the spectrum casts doubt on such an assignment for the bands observed here. There may be a modest decrease in the relative intensity of the ν_8 vibration at 392 cm^{-1} and the appearance of a very weak band at ca. 372 cm^{-1}, but it is far from clear in the data. The shifts of the ν_1, ν_2 and ν_4 vibrations are also smaller than previously reported for reduction upon axial photolysis.[5,9,56]

In order for a HS Fe$^{(II)}$ species to account for this set of structure sensitive vibrations the resonant enhancement of its ν_8 vibration must be dramatically smaller than that of the ground state. Also, to make up for the drop in population of states possessing a ν_8 vibration near 392 cm^{-1} the other products would need to show a larger enhancement of the scattering from this vibration. It is unlikely both of these conditions are met in the data observed above.

This set of high frequency vibrations at lower frequency than the ground state corresponding to Product B are also consistent with a six-coordinate HS Fe$^{(III)}$ species. Similarly coordinated HS Fe$^{(III)}$TPP systems also show ν_8 vibration in the region of 390 cm^{-1}. Based on these comparisons, it is likely that these bands [ν_2 (1541 cm^{-1}) and ν_4 (1349 cm^{-1})] belong to a six-coordinate HS Fe$^{(III)}$TPP species.

The central components corresponding to Product C are consistent with the rR scattering of the ground state, high-spin Fe$^{(III)}$ species, although slightly shifted to lower frequency from the ground state values. The position of these structure-sensitive bands implies that this product state does not have a structure that substantially varies from that of the ground state. These bands can be assigned to either a five-coordinate HS Fe$^{(III)}$ compound or a LS six-coordinate Fe$^{(II)}$ compound. Formation of the LS Fe$^{(II)}$ compound is generally accompanied by a small red-shift of the frequency of the 392 cm^{-1} ν_8 vibration but the magnitude of the shift can be only a few cm^{-1}. There is no clear evidence for such a shift in the spectrum, but decrease in the relative intensity of the ν_8 band could mask the influence of a small frequency shift.

The high frequency ν_2 and ν_4 bands at 1566 cm^{-1} and 1376 cm^{-1} accompanied by a dominant unshifted 392 cm^{-1} ν_8 vibration are consistent with ring contraction accompanying formation of a six-coordinate LS Fe$^{(III)}$ species or a four-coordinate Fe$^{(II)}$TPP. Structure-sensitive rR vibrations aid in deciphering between the oxidation state of the central Fe atom in this product state. Early work by Spiro and coworkers showed that six-coordinate, LS Fe$^{(III)}$ centered TPP complexes with a polarized band at 1568 cm^{-1} also show a polarized band at 1456 cm^{-1}.[58] This vibration is absent, however, in the four-coordinate Fe$^{(II)}$ species. The photoproducts produced from Fe$^{(III)}$TPPCl in the presence of toluene exhibit a triplet of ν_3 bands at 1454 cm^{-1}, 1442 cm^{-1}, and 1431 cm^{-1}. This band is absent, however, in the photoinduced formation of Fe$^{(II)}$ in the presence of acetone (see FIG. 5.6). The appearance of a polarized band in this spectral region supports assignment of the photoproduct to a six-coordinate LS Fe$^{(III)}$ species rather than a four-coordinate Fe$^{(II)}$TPP.

This comparison with a range of known compounds leads to the following conclusion: *The most likely assignments for the vibrational bands observed in the photoproduct are a six-coordinate high-spin Fe$^{(III)}$ compound, a five-coordinate high-spin Fe$^{(III)}$ compound, and a six-coordinate low-spin Fe$^{(III)}$ compound.*

Fitting the vibrational bands in the 1500 cm^{-1} to 1600 cm^{-1} region of the spectrum to a sum of Gaussians provides an estimate for the relative contribution of each component to the Raman scattering: 26 ± 3% high-spin, six-coordinate; 40 ± 5% high-spin, five-coordinate; 34 ± 3% low-spin, six-coordinate (see Supporting Information). If the resonance enhancements and the forms of the normal coordinates for all three compounds are the same, these percentages provide approximate populations. As it is likely that the resonance enhancements and the form of the normal coordinates are similar, it is reasonable to assume that the three products are formed with comparable yields although the populations may not correspond quantitatively to the relative intensities.

C. Photochemical Pathways

Excitation of Fe$^{(III)}$TPPCl in a 1:1 mixture of toluene and CH_2Cl_2 at 77K results in formation of an excited electronic state with a lifetime greater than 1 ns. From the low temperature transient absorption measurements, this excited state has an absorption spectrum similar to that of the ground state with a slight red-shift of the Soret absorption band. Absorption of a second photon at 413 nm from this excited state accesses a photochemical pathway that is unavailable with 514.5 nm or 488.0 nm excitation.

As described above, two high frequency toluene vibrations show nonlinear changes in peak intensity as a function of the incident laser power. The ligand recruitment of near-by solvating toluene molecules is supported by the resonance enhancement of toluene bands at 1210 cm^{-1} and 1605 cm^{-1} and the absence of any detectable photochemistry in neat CH_2Cl_2 solvent. These bands shift to lower frequencies when the solvent contains deuterated toluene as illustrated in FIG 5.9. This shift eliminates the possibility that this observation represents enhancement of vibrations of the phenyl groups decorating the porphyrin ring.

All of the 2-photon models in section 1 of this discussion presume that the absorption rate of the state E_2 is the same as that of ground state. Therefore, any nonlinear increase in the intensity of solvent bands as a function of the incident laser power points to solvent-chromophore exciplex formation. Upon formation of the exciplex, the solvent bands likely become resonantly enhanced by an electronic transition that contains character from a Fe to toluene charge transfer process.[52] This resonant enhancement produces a nonlinear laser power-dependent peak intensity of these bands. However, from this resonance enhancement we cannot tell if one, two or all three of the product states feature one or more ligated toluene molecules.

As discussed in the preceding section, researchers have shown that different aromatic solvent molecules ligate in the axial position to $[Fe^{(III)}TPP]^+$ ions.[76] It is likely that a toluene-$Fe^{(III)}$TPP exciplex forms in these measurements due to dissociation of the axial bond and formation of a chloride (Cl^-) and $[Fe^{(III)}TPP]^+$ ion pair. Dissociation of the axial Cl atom can occur in one of at least two ways: 1) direct photodissociation upon 413 nm excitation from the E_2 state or 2) populating a dissociative state along the non-radiative relaxation pathway of the state excited by 413 nm absorption by the E_2 state. The measurements presented above cannot decipher between these two pathways.

Once the Cl^- forms, it may or may not leave the coordination sphere of the iron atom. On one hand, the Cl^- may find stabilization outside of the coordination sphere due to the presence of CH_2Cl_2. In such case a HS $[Fe^{(III)}TPP(Tol)]^+$ species likely corresponds to the middle frequency set of structure sensitive bands. Distortions due to steric hindrance between the ligated tolune and the porphyrin ring may account for the slight shifts to lower frequency of these bands relative to those of the ground state.

On the other hand, the Cl^- may be stabilized within the coordination sphere of the iron, but still remain a distinct ion. Santha et al. report characteristics of a six-coordinate HS $Fe^{(III)}TPP$ in which one axial ligand is a 1,2-DiMeIm and the other is a dissociated Cl^- ion forming a $[Fe^{(III)}TPP(1,2\text{-}DiMeIm)]^+Cl^-$ species.[56] It is likely that while Cl^- is formed, it cannot move far from the coordinate sphere of iron atom due to the solid nature of its environment and low temperature at which the experiments were conducted. It is possible that after formation of the toluene-$Fe^{(III)}TPP$ exciplex the Cl^- still acts as an axial ligand on the opposite face of the porphyrin ring from the newly recruited toluene molecule. Therefore, this six-coordinate $[Fe^{(III)}TPP(Tol)]^+$ Cl^- is the likely identity of the species displaying the lowest and highest frequency sets of the structure sensitive rR active vibrations in the observed spectra in FIG. 5.2. These spectra also show that this six-coordinate $Fe^{(III)}$ appears in both its high ($^6A_{1g}$) and low ($^2T_{2g}$) spin states.

Formation of the ground state from the long-lived product states occurs with high yield since the Cl^- is likely never far from the coordinate sphere of the Fe atom. Barriers to re-combination likely include electrostatic interactions between the Cl^- and CH_2Cl_2 solvent molecules. At low temperature the time necessary for substantial amounts of dissociated Cl^- ions to cross this and over barriers is long enough that metastable product states form to be measured. However, given the measurements at lower incident laser powers the product state is not permanent and Cl^- can cross this barrier.

D. Spin Transitions in the Photochemistry of $Fe^{(III)}TPPCl$

In the presence of weak ligands, the ground electronic states of iron(III)-centered porphyrins have shown characteristics consistent with mixtures of spin states.[77] At 77 K and 88 K the ground state of $[Fe^{(III)}TPP(Tol)]^+$ Cl^- may not be represented simply by the HS state from which it formed. Since the dissociated state forms from the HS species of the $Fe^{(III)}TPP$, it is likely that all of the formed $[Fe^{(III)}TPP(Tol)]^+ Cl^-$ initially populates the HS state. However, from this initially excited species a sizable amount of spin population crosses over to the LS state.

The photochemistry of $Fe^{(III)}TPPCl$ begins from a high-spin $Fe^{(III)}$ compound and it is expected that the initial products are formed in an electronically excited high-spin state. The ground state of the metastable product will depend on the strength of the ligands and the distortion, if any, of the porphyrin ring. From this initial high-spin excited state species a sizable population crosses over to the low-spin six-coordinate $[Fe^{(III)}TPP(Tol)^+Cl^-]$ state. The spin transition forming the low-spin compound likely occurs via an intersystem crossing along the non-radiative relaxation pathway of the electronically excited high-spin $[Fe^{(III)}TPP(Tol)^+Cl^-]$,[35,36,41] but the conversion is not complete and the steady state product distribution contains comparable populations of both the high-spin and the low-spin species.

At least two possible mechanisms explain the accumulation of both high-spin and low-spin products. First, the additional toluene ligand bound to the Fe atom produces an increased ligand-field such that the energy necessary to pair the *d*-electrons is smaller than the splitting of the e_g and t_{2g} *d*-orbitals of the iron. After initial formation of the six-coordinate species, intersystem crossing occurs from the high- to the low-spin ground state of the molecule. Some of the population remains trapped in the high-spin configuration. A second possibility is that the six-coordinate product has an intermediate ligand field and corresponds to a spin crossover compound. In this case, at sub-100 K temperatures a spin equilibrium between the high- and low-spin states could be observed. Here, distortions to the porphyrin ring induced by the toluene ligand in the solid state of the solvent glass could mediate the spin transition. At these temperatures, population would then thermally equilibrate in the two spin states producing the ratios observed in our data. Each of the possibilities is examined below.

First, the ground states of many six-coordinate ferric porphyrins possess a $Fe^{(III)}$ ion in its low-spin configuration. The strong ligand field present due to the large number of bonds increases the splitting of the *d*-orbitals of the Fe atom. The increased splitting makes pairing the *d*-electrons in the t_{2g} orbitals more energetically favorable than populating the higher lying e_g orbitals. This pairing produces the low-spin configuration.

In our case, the five-coordinate species is excited to a high lying state in which the e_g orbitals are populated due to weaker ligand field splitting. This state ligates a near-by toluene molecule forming a six-coordinate species. The ligand field splitting of this state changes such that pairing the *d*-electrons is energetically favorable. Therefore, electronic population crosses over to the t_{2g} orbitals producing the low-spin configuration.

Dynamically, this transition necessitates either an intersection of the potential energy surfaces of the two spin species or tunneling between the states. However, our data cannot distinguish between these two dynamical processes. If this coordination-driven mechanism accounts for the spin transition, one would need a temperature-dependent study of the relative populations of each spin state. Changes in the relative populations of the different spin states as a function of temperature would point to a crossing between energy surfaces over a barrier, while no change in the relative populations as a function of temperature would point to tunneling as the dominant mechanism for the spin transitions observed above.

However, induction of a strong ligand field by the proposed axial ligands necessitates examination of the role of this mechanism in the observed photochemistry. On one hand, toluene likely acts as a weak ligand to Fe in this product state similar to the toluene observed by Evans *et al.* in an x-ray crystal structure.[76] This conclusion is also supported by the fact that the product is not permanent, even at 77 K. On the other hand, the ligand field splitting due to Cl^- is quite low in the spectrochemical series. In fact, Santha *et al.* report the room temperature formation of a high-spin, six-coordinate $Fe^{(III)}$TPP ligated to a Cl^- and 1,2-dimethylimidazole in the axial positions.[60] Since toluene is a weaker ligand than 1,2-dimethylimidazole, it is possible that the room temperature ground state of the product is a high-spin configuration and another mechanism accounts for the spin transition.

In this second mechanism, the six-coordinate product formed after excitation is actually a spin crossover complex where the high- and low-spin states are essentially isoenergetic. Because of this, a thermal equilibrium of spin states could then be observed at the low temperatures used for the Raman measurements. Here, the spin transition between the two states could be modulated by vibronic coupling between the *d*-electrons of the Fe$^{(III)}$ to the vibrations of the ligands.[35,36,41]

This mechanism may be supported by the power dependent Raman scattering. From the power dependence spectra in FIG 5.2, several vibrations appear in regions where no ground state Raman active vibrations exist. Of note are the distinct band at 1296 cm^{-1}, the two shoulders near 1330 cm^{-1} and 1315 cm^{-1}, two peaks between 1140 cm^{-1} and 1190 cm^{-1} as well as a peak to lower frequency from the ground state vibration at 1495 cm^{-1}. It is likely that these bands appear in the photoproduct spectra due to symmetry lowering caused by distortions to the porphyrin ring in the presence of a toluene ligand. Alleviating restrictions on selection rules for inelastic light scattering, lowering the symmetry of the ring increases the number of Raman active vibrations. These same distortions may account for the appearance of a LS species of the proposed photoproduct. However, Jahn-Teller distortions to the excited state participating in the resonantly enhanced scattering process may also account for the appearance of these vibrations. Our data cannot distinguish between these two mechanisms.

These mechanisms could be unraveled by a combination of optical pump-EPR or NMR probe and more extensive time-resolved optical pump, optical probe and optical pump, Raman probe measurements as a function of temperature. The current data set provides only Raman data on the power-dependent photostationary state population.

Conclusions

We have presented power and solvent dependent resonance Raman scattering of Fe$^{(III)}$TPPCl at cryogenic temperatures excited on the Soret resonance. When the incident 413.14 nm laser power is increased, the resonance Raman scattering begins to show evidence of the presence of a state of the molecule other than the ground state. Singular value decomposition (SVD) was used to produce species associated spectra.

Low temperature transient absorption spectroscopy was used to confirm that a state with distinct changes in absorption is produced upon excitation of the Soret. This state shows distinct changes in absorption at time delays of up to 1 ms. Room temperature measurements were also made to test the validity of the low temperature measurements.

The key parameter to the photochemistry and LIESST in Fe$^{(III)}$TPPCl is the lifetime of the longest-lived excited electronic state. If a synthetic iron (III) porphyrin were be tuned such that the room temperature lifetime of this state were long enough, we believe that similar spin crossover transitions would occur. Solvent and solid state considerations would also be necessary since we observe a strict solvent dependence in the measured photochemistry.

Given the wide breadth of research into tuning the parameters of porphyrin-based materials in a wide variety of condensed phase conditions, it is believable that such a synthetic porphyrin will be found. Therefore, this result opens new possibilities for controllable magnetism in fields ranging from solar energy conversion, information technology.

References

1. P. A. Cornelius, A. W. Steele, D. A. Chernoff and R. M. Hochstrasser, Chemical Physics Letters **82** (1), 9-14 (1981).
2. Y. Liang, D. K. Negus, R. M. Hochstrasser, M. Gunner and P. L. Dutton, Chemical Physics Letters **84** (2), 236-240 (1981).
3. M. A. Lopez and P. A. Kollman, Journal of the American Chemical Society **111** (16), 6212-6222 (1989).
4. J. C. Austin, S. E. J. Bell and R. E. Hester, Chemical Physics Letters **169** (4), 342-346 (1990).
5. S. N. Terekhov and S. G. Kruglik, Chemical Physics Letters **245** (2-3), 268-272 (1995).
6. J. R. Reimers, T. X. Lu, M. J. Crossley and N. S. Hush, Chemical Physics Letters **256** (4-5), 353-359 (1996).
7. J. R. Hill, C. J. Ziegler, K. S. Suslick, D. D. Dlott, C. W. Rella and M. D. Fayer, Journal of Physical Chemistry **100** (46), 18023-18032 (1996).
8. T. G. Spiro, P. M. Kozlowski and M. Z. Zgierski, Journal of Raman Spectroscopy **29** (10-11), 869-879 (1998).
9. S. C. Jeoung, D. Kim, D. W. Cho and M. Yoon, Journal of Physical Chemistry A **104** (21), 4816-4824 (2000).
10. A. K. Burrell and M. R. Wasielewski, Journal of Porphyrins and Phthalocyanines **4** (4), 401-406 (2000).
11. T. Wondimagegn and A. Ghosh, Journal of the American Chemical Society **123** (24), 5680-5683 (2001).

12. Q. H. Xu, D. E. Thompson, K. A. Merchant and M. D. Fayer, Chemical Physics Letters **355** (1-2), 139-146 (2002).
13. J. H. Mao, Y. Zhang and E. Oldfield, Journal of the American Chemical Society **124** (46), 13911-13920 (2002).
14. J. S. Baskin, H. Z. Yu and A. H. Zewail, Journal of Physical Chemistry A **106** (42), 9837-9844 (2002).
15. H. Z. Yu, J. S. Baskin and A. H. Zewail, Journal of Physical Chemistry A **106** (42), 9845-9854 (2002).
16. C. K. Chang, N. Bag, B. M. Guo and S. M. Peng, Inorganica Chimica Acta **351**, 261-268 (2003).
17. T. Nishino, T. Ito and Y. Umezawa, Proceedings of the National Academy of Sciences of the United States of America **102** (16), 5659-5662 (2005).
18. S. Sorgues, L. Poisson, K. Raffael, L. Krim, B. Soep and N. Shafizadeh, Journal of Chemical Physics **124** (11), 10 (2006).
19. J. D. Harvey and C. J. Ziegler, Journal of Inorganic Biochemistry **100** (4), 869-880 (2006).
20. J. Y. Zhuang, J. H. Amoroso, R. Kinloch, J. H. Dawson, M. J. Baldwin and B. R. Gibney, Inorganic Chemistry **45** (12), 4685-4694 (2006).
21. M. U. Winters, E. Dahlstedt, H. E. Blades, C. J. Wilson, M. J. Frampton, H. L. Anderson and B. Albinsson, Journal of the American Chemical Society **129** (14), 4291-4297 (2007).
22. L. Grill, M. Dyer, L. Lafferentz, M. Persson, M. V. Peters and S. Hecht, Nature Nanotechnology **2** (11), 687-691 (2007).
23. H. Wende, M. Bernien, J. Luo, C. Sorg, N. Ponpandian, J. Kurde, J. Miguel, M. Piantek, X. Xu, P. Eckhold, W. Kuch, K. Baberschke, P. M. Panchmatia, B. Sanyal, P. M. Oppeneer and O. Eriksson, Nature Materials **6** (7), 516-520 (2007).
24. A. Marcelli, P. Foggi, L. Moroni, C. Gellini and P. R. Salvi, Journal of Physical Chemistry A **112** (9), 1864-1872 (2008).
25. N. Xu, J. Yi and G. B. Richter-Addo, Inorganic Chemistry **49** (14), 6253-6266 (2010).
26. M. Jurow, A. E. Schuckman, J. D. Batteas and C. M. Drain, Coordination Chemistry Reviews **254** (19-20), 2297-2310.
27. S. P. Koiry, P. Jha, D. K. Aswal, S. K. Nayak, C. Majumdar, S. Chattopadhyay, S. K. Gupta and J. V. Yakhmi, Chemical Physics Letters **485** (1-3), 137-141.
28. G. G. Qian, S. Saha and K. M. Lewis, Applied Physics Letters **96** (24).
29. B. Grimm, A. Hausmann, A. Kahnt, W. Seitz, F. Spanig and D. M. Guldi, in *Handbook of Porphyrin Science: With applications to chemistry, physics, materials science, engineering, biology, and medicine*, edited by K. M. Kadish, K. M. Smith and R. Guilard (World Scientific, Singapore, 2010), Vol. 1, pp. 133-219.
30. M. Sorai and S. Seki, J. Phys. Chem. Solids **35** (4), 555-570 (1974).
31. G. Molnar, V. Niel, J. A. Real, L. Dubrovinsky, A. Bousseksou and J. J. McGarvey, J. Phys. Chem. B **107** (14), 3149-3155 (2003).

32. V. Ksenofontov, G. Levchenko, H. Spiering, P. Gutlich, J. F. Letard, Y. Bouhedja and O. Kahn, Chem. Phys. Lett. **294** (6), 545-553 (1998).
33. J. Zarembowitch and O. Kahn, New J. Chem. **15** (2-3), 181-190 (1991).
34. J. A. Real, H. Bolvin, A. Bousseksou, A. Dworkin, O. Kahn, F. Varret and J. Zarembowitch, J. Am. Chem. Soc. **114** (12), 4650-4658 (1992).
35. S. Decurtins, P. Gutlich, C. P. Kohler, H. Spiering and A. Hauser, Chemical Physics Letters **105** (1), 1-4 (1984).
36. S. Decurtins, P. Gutlich, K. M. Hasselbach, A. Hauser and H. Spiering, Inorganic Chemistry **24** (14), 2174-2178 (1985).
37. E. A. Juban, A. L. Smeigh, J. E. Monat and J. K. McCusker, Coordination Chemistry Reviews **250** (13-14), 1783-1791 (2006).
38. M. R. Wasielewski, Chemical Reviews **92** (3), 435-461 (1992).
39. D. Q. Li, B. I. Swanson, J. M. Robinson and M. A. Hoffbauer, Journal of the American Chemical Society **115** (15), 6975-6980 (1993).
40. D. H. Lee, W. J. Lee, W. J. Lee, S. O. Kim and Y.-H. Kim, Physical Review Letters **106** (17), 175502 (2011).
41. M. Andersson, J. Davidsson, L. Hammarstrom, J. Korppi-Tommola and T. Peltola, Journal of Physical Chemistry B **103**, 3258-3262 (1999).
42. R. T. Hayes, C. J. Walsh and M. R. Wasielewski, Journal of Physical Chemistry A **108** (13), 2375-2381 (2004).
43. Y. K. Kang, T. V. Duncan and M. J. Therien, Journal of Physical Chemistry B **111** (24), 6829-6838 (2007).
44. D. LeGourrierec, M. Andersson, J. Davidsson, E. Mukhtar, L. Sun and L. Hammarstrom, Journal of Physical Chemistry A **103**, 557-559 (1999).
45. N. Mataga, H. Chosrowjan and S. Taniguchi, Journal of Photochemistry and Photobiology C: Photochemistry Reviews **6**, 37-79 (2005).
46. J. Petersson, M. Eklund, J. Davidsson and L. Hammarstrom, Journal of the American Chemical Society **131** (23), 7940-+ (2009).
47. T. G. Spiro and J. M. Burke, J. Am. Chem. Soc. **98** (18), 5482-5489 (1976).
48. A. D. Adler, F. R. Longo, Finarell.Jd, Goldmach.J, J. Assour and Korsakof.L, Journal of Organic Chemistry **32** (2), 476 (1967).
49. A. D. Adler, F. R. Longo, F. Kampas and J. Kim, Journal of Inorganic & Nuclear Chemistry **32** (7), 2443-2445 (1970).
50. F. Paulat, V. K. K. Praneeth, C. Nather and N. Lehnert, Inorganic Chemistry **45** (7), 2835-2856 (2006).
51. T. Rush, R. Kumble, A. Mukherjee, M. E. Blackwood and T. G. Spiro, Journal of Physical Chemistry **100** (29), 12076-12085 (1996).
52. J. M. Burke, J. R. Kincaid, S. Peters, R. R. Gagne, J. P. Collman and T. G. Spiro, Journal of the American Chemical Society **100** (19), 6083-6088 (1978).
53. G. Chottard, P. Battioni, J. P. Battioni, M. Lange and D. Mansuy, Inorganic Chemistry **20** (6), 1718-1722 (1981).
54. N. Parthasarathi, C. Hansen, S. Yamaguchi and T. G. Spiro, Journal of the American Chemical Society **109** (13), 3865-3871 (1987).

55. V. Fidler, T. Ogura, S. Sato, K. Aoyagi and T. Kitagawa, Bulletin of the Chemical Society of Japan **64** (8), 2315-2322 (1991).
56. C. Bartocci, A. Maldotti, G. Varani, P. Battioni, V. Carassiti and D. Mansuy, Inorganic Chemistry **30** (6), 1255-1259 (1991).
57. S. Sato, K. Kamogawa, K. Aoyagi and T. Kitagawa, Journal of Physical Chemistry **96** (26), 10676-10681 (1992).
58. P. K. Shantha, G. S. S. Saini, H. H. Thanga and A. L. Verma, Journal of Raman Spectroscopy **32** (3), 159-165 (2001).
59. P. K. Shantha, G. S. S. Saini, H. H. Thanga and A. L. Verma, Journal of Raman Spectroscopy **34** (4), 315-321 (2003).
60. P. K. Shantha, H. H. Thanga and A. L. Verma, Journal of Raman Spectroscopy **29** (10-11), 997-1001 (1998).
61. D. N. Hendrickson, M. G. Kinnaird and K. S. Suslick, Journal of the American Chemical Society **109** (4), 1243-1244 (1987).
62. M. Hoshino, K. Ueda, M. Takahashi, M. Yamaji and Y. Hama, Journal of the Chemical Society-Faraday Transactions **88** (3), 405-408 (1992).
63. S. C. Jeoung, D. Kim and D. W. Cho, Journal of Raman Spectroscopy **31** (4), 319-330 (2000).
64. E. R. Henry and J. Hofrichter, Methods in Enzymology **210**, 129-192 (1992).
65. L. Leondiadis, M. Momenteau and A. Debois, Inorganic Chemistry **31** (22), 4691-4696 (1992).
66. K. S. Suslick and R. A. Watson, Inorganic Chemistry **30** (5), 912-919 (1991).
67. K. S. Suslick, J. F. Bautista and R. A. Watson, Journal of the American Chemical Society **113** (16), 6111-6114 (1991).
68. C. Bizet, P. Morliere, D. Brault, O. Delgado, M. Bazin and R. Santus, Photochemistry and Photobiology **34** (3), 315-321 (1981).
69. H. Oshio, T. Ama, T. Watanabe, J. Kincaid and K. Nakamoto, Spectrochimica Acta Part A: Molecular Spectroscopy **40** (9), 863-870 (1984).
70. F. Paulat and N. Lehnert, Inorganic Chemistry **47** (11), 4963-4976 (2008).
71. R. J. Cheng, L. Latosgrazynski and A. L. Balch, Inorganic Chemistry **21** (6), 2412-2418 (1982).
72. J. M. Burke, J. R. Kincaid and T. G. Spiro, Journal of the American Chemical Society **100** (19), 6077-6083 (1978).
73. J. P. Costes, F. Dahan and J. P. Laurent, Inorganic Chemistry **29** (13), 2448-2452 (1990).
74. A. H. Ewald, R. L. Martin, E. Sinn and A. H. White, Inorganic Chemistry **8** (9), 1837-& (1969).
75. W. D. Federer and D. N. Hendrickson, Inorganic Chemistry **23** (24), 3861-3870 (1984).
76. Evans, D. R.; Fackler, N. L. P.; Xie, Z. W.; Rickard, C. E. F.; Boyd, P. D. W.; Reed, C. A. *J. Am. Chem. Soc.* **1999**, *121*, 8466-8474.
77. X. Y. Kuang and K. W. Zhou, Journal of Physical Chemistry A **104** (31), 7308-7313 (2000).

78. I. Lawthers and J. J. McGarvey, Journal of the American Chemical Society **106** (15), 4280-4282 (1984).
79. X. Y. Kuang, I. Morgensternbadarau and I. Malfant, Physical Review B **47** (9), 5455-5458 (1993).
80. G. Harris, Theoretica Chimica Acta **10** (2), 119-& (1968).
81. A. K. Gregson, Inorganic Chemistry **20** (1), 81-87 (1981).
82. T. Otsuka, T. Ohya and M. Sato, Inorganic Chemistry **24** (5), 776-782 (1985).
83. M. A. Halcrow, Chemical Society Reviews **40** (7), 4119-4142 (2011).
84. M. Nihei, T. Shiga, Y. Maeda and H. Oshio, Coordination Chemistry Reviews **251** (21-24), 2606-2621 (2007).
85. A. L. Smeigh, M. Creelman, R. A. Mathies and J. K. McCusker, Journal of the American Chemical Society **130** (43), 14105-+ (2008).
86. F. A. Walker, Chemical Reviews **104** (2), 589-615 (2004).
87. P. Kukura, D. W. McCamant and R. A. Mathies, in *Annual Review of Physical Chemistry* (2007), Vol. 58, pp. 461-488.
88. D. W. McCamant, P. Kukura and R. A. Mathies, Journal of Physical Chemistry A **107** (40), 8208-8214 (2003).
89. D. W. McCamant, P. Kukura, S. Yoon and R. A. Mathies, Review of Scientific Instruments **75** (11), 4971-4980 (2004).

Chapter 6:
Experimental Test of LG-Amended Resonance Raman Scattering

Experimental Methods

To test the theoretical predictions of Chapter 3 and Alexandrescu et al.,[1] two different experimental tests of were undertaken on two different molecular systems interacting with LG beams. First, diatomic iodine (I_2) was dissolved in liquid cyclohexane (C_6H_{12}), flowed for constant refreshing of the illuminated sample and excited with the second harmonic from a Spectra Physics Millenia V diode-pumped Nd:YAG laser at room temperature. This 532 nm laser light is near the peak absorption of I_2, as seen in FIG. 6.1. The excitation of the electronic transition at 532 nm means that the resonance-enhanced formalism accounts for the observed scattering.

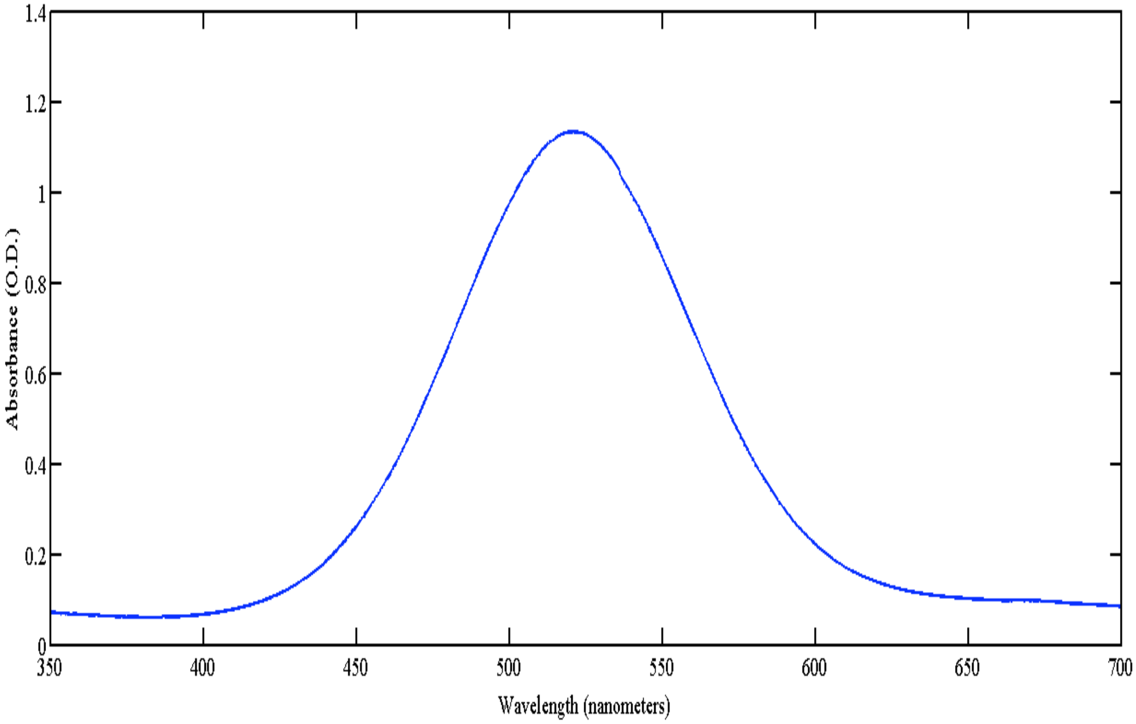

Figure. 6.1. UV-vis absorption of I_2 dissolved in C_6H_{12} showing that the scattering process excited at 532 nm is well-described by the resonance-enhanced formalism.

Scattered light was collected, passed through a Kaiser Optical Systems Inc. holographic notch filter for 532 nm light and free-space coupled in a Spex 500M single monochromator fitted with a LN2-cooled 1100x330 pixel Princeton Instruments Inc. CCD detector. Spectra were collected for the integration time of 60 seconds and 4 individual spectra were averaged together and filtered to remove spikes due to 'cosmic ray' detection.

The excitation beam was converted to an LG beam using the 527 nm position of an l=1 Vortex Phase Plate from Rochester Photonics Inc. A vortex phase plate uses a polymer of azimuthally varying thickness deposited on a glass substrate to produce a LG beam with a helical wavefront.[2, 3] It is not clear that the phase plate produces a pure l=1 mode, but the mode is clearly a vortex with components $l \geq 1$. To maintain a fundamental beam as output by the laser the phase plate was translated vertically so that while the beam was still traveling through the substrate, it was not traveling through the polymer layer. The beam passing only through the substrate does not attain the spatial variation characteristic of a higher order transverse mode. Spectra obtained with the laser beam passing through the substrate and with the phase plate removed from the beam altogether were identical.

Experimental tests were also undertaken with $Fe^{(III)}$TPPCl dissolved in a 1:1 mixutre of toluene (C_7H_8) and dichloromethane (CH_2Cl_2). The room temperature sample was illuminated by the 413.1 nm and 514.5 nm lines of a Spectra Physics Ar-Kr gas laser. These wavelengths correspond to near the peak of the Soret and Q_v, respectively, as explained in Chapters 4 and 5 and shown in Figure 6.2. This experiment tests the predictions in Chapter 3 since the scattering is resonantly enhanced by each respective transition. In the case $Fe^{(III)}$TPPCl, the excitation beam was passed through a $\lambda/2$-plate to test against the possibility of changes in the polarization of the scattered light as well as its intensity.

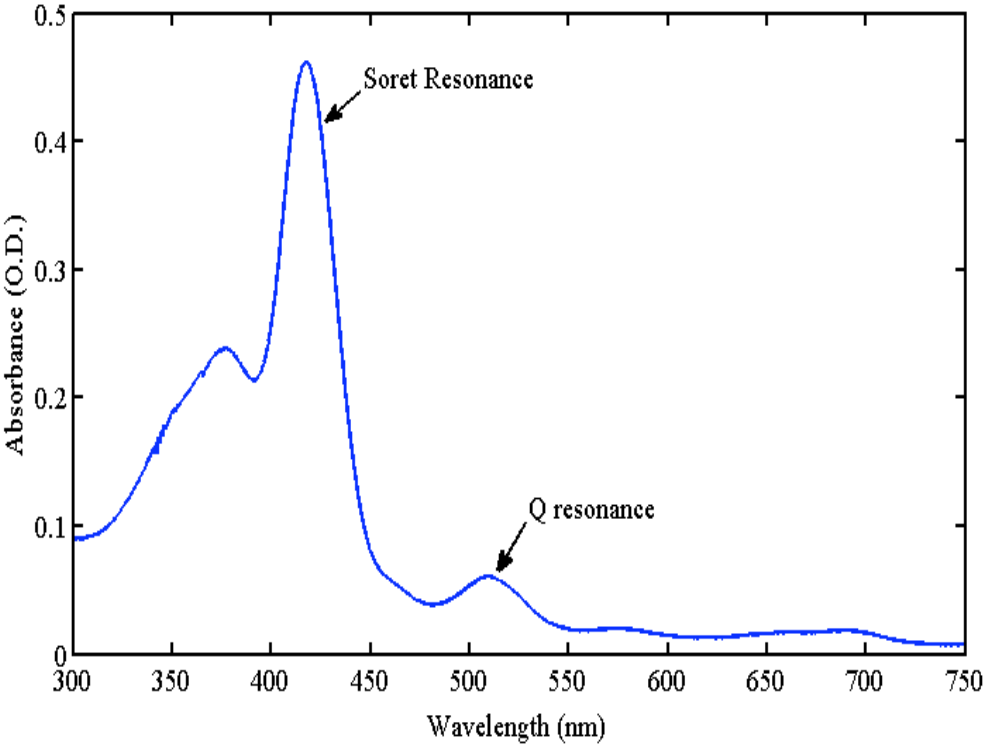

Figure 6.2. UV-vis absorption of Fe$^{(III)}$TPPCl in 1:1 mixture of toluene and dichloromethane showing electronic resonances with 413.14 nm and 514.5 nm excitations.

The scattered lighted was collected, passed through a Kaiser Optical Holographic Notch filter designed for the laser line of a given measurement to remove the residual laser and Rayleigh scattering and free-spaced coupled into a Princeton Instruments Tri-Vista Raman Spectrometer fitted with a liquid N_2 cooled CCD detector. The spectrometer was used in double additive mode with two 1800 gr/mm gratings for production of high-resolution spectra.

A similar protocol used for production of the LG beam. Given the difference in excitation wavelength for each respective electronic resonance of this molecule, the 419.1 nm position of a l=2 Rochester Photonics Inc. phase plate was used for this experiment was used for scattering resonantly enhanced by the Soret transition at 413.1 nm. The 512.4 nm position of a l=1 phase plate and the 520.1 nm position of a l=2 phase plate were used for scattering resonantly enhanced by the Q_v transition. Spectra excited with the TEM_{00} mode were checked with and without the phase plate, showing no measureable difference at either excitation wavelength.

Experimental Results

Collected resonance Raman spectra from I_2 are shown in FIG. 6.3. The first, second and third overtones of the 211 cm^{-1} vibration of I_2 are shown. The fundamental exciation of this vibration is not shown due to experimental constraints of the setup. As pointed out in Chapter 3, the vibrational overtone excitations in a diatomic molecule should serve as a very sensitive probes of how strongly the transverse profile of a higher order LG laser beam couples to the vibrational degrees of freedom of the molecules to amend the scattering process.

Within the limits of detection with this experimental system, however, there is no difference between the scattering using a TEM_{00} beam and that of the l=1 LG beam. Giving the noise of each measurement and the average signal-to-noise ration (SNR), we believe our detection limit is about 1/1000 with this system. This limit allows us to provide a ceiling on the magnitude of the coefficient of the sixth term in Eqn. (3.27). The resonance Raman scattering from I_2 due to a l=0 beams is compared to that of a l=1 in FIG. 6.3.

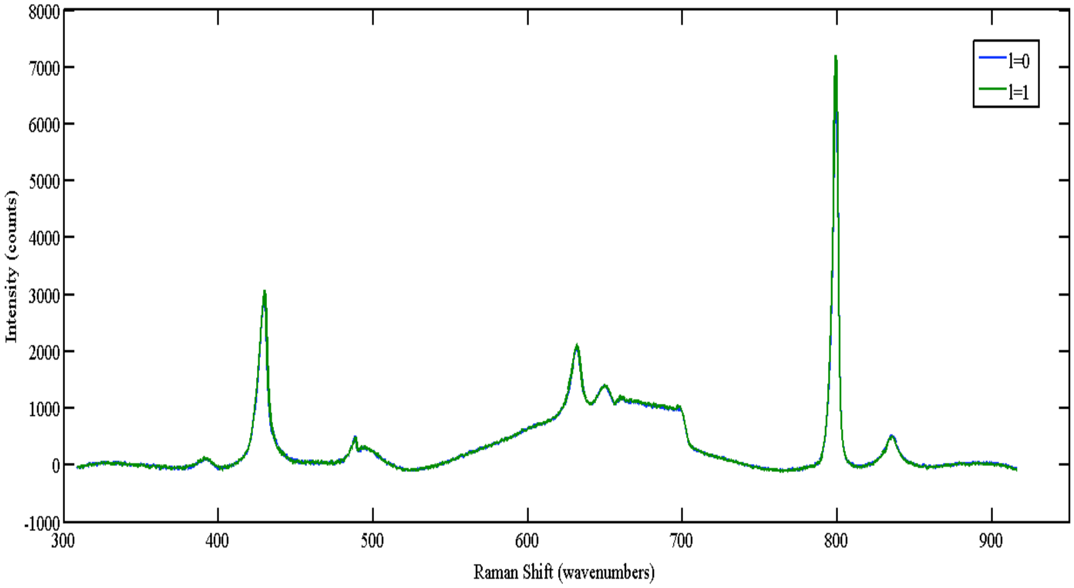

FIG. 6.3. 532 nm excited resonance Raman spectra of I_2 dissolved in cyclohexane for l=0 and l=1 excitation beams. The first three overtones are shown for comparison of scattering as a function of the transverse profile of the excitation beam. There is no detectable difference in the scattering as a function of the incident beam profile or OAM.

Measurements of the beam-dependent scattering of $Fe^{(III)}$TPPCl would allow for direct tests of the predictions made in Chapter 3 of the interference effects introduced by an incident LG beams. A representative sample of collected spectra scattering from this molecule and excited at 413.1 nm is shown in FIG. 6.4. The spectra correspond to the fundamental excitation high-energy ring vibrations in the interior porphyrin ring structure. Most notable are the v_2 (1556 cm^{-1}), v_4 (1365 cm^{-1}) and v_1 (1237 cm^{-1}) totally symmetric vibrations. For these totally symmetric vibrations that the theory from Chapter 3 predicts interesting effects dependent on the detuning from the peak of the electronic transision due to the presence of the LG excitation beam. There is also a non-totally symmetric vibration near 1200 cm^{-1} present in the 'A' term scattering here due to a Jahn-Teller distortion of the excited electronic state along that coordinate.[4]

For each of the present vibrations, however, given our detection limit with this instrument, there is no detectable difference in the scattering as a function of the excitation laser beam. This is also true of the scattering when accounting for the polarization of the scattered light. We see no significant changes in the polarization ratio, ρ, as a function of the excitation beam. Slight differences between the parallel-polarized spectra in FIG. 6.4 are likely due to differences in our ability to fit the raw data to a flat baseline.

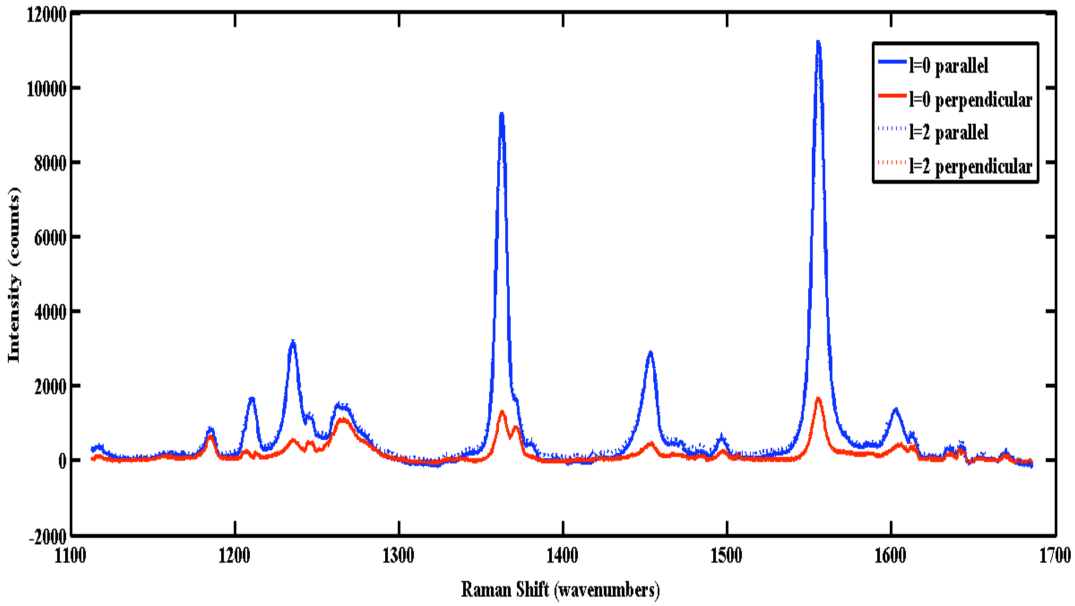

FIG. 6.4. 413.14 nm excited polarized resonance Raman spectra of high-energy ring vibrations of $Fe^{(III)}$TPPCl in 1:1 mixture of toluene and CH2Cl2 as a function of transverse profile of excitation beam.

FIG. 6.5 shows the mode-dependent scattering of Fe(III)TPPCl in a 1:1 mixture of toluene and CH_2Cl_2 excited to the Q_v transition. Excitation on this transition will lead resonance enhancement of several non-totally symmetric vibrations, most notably the anomalously polarized bands at 1520 cm^{-1} and 1337 cm^{-1}. While Chapter 3 did not make specific predictions with respect to non-totally symmetric or anti-symmetric vibrations, it is possible for these bands to be affected by the coupling of the LG beam. However, again, with within the sensitivity limits of the measurement, there is no difference in the observed spectra as a function of the incident laser mode.

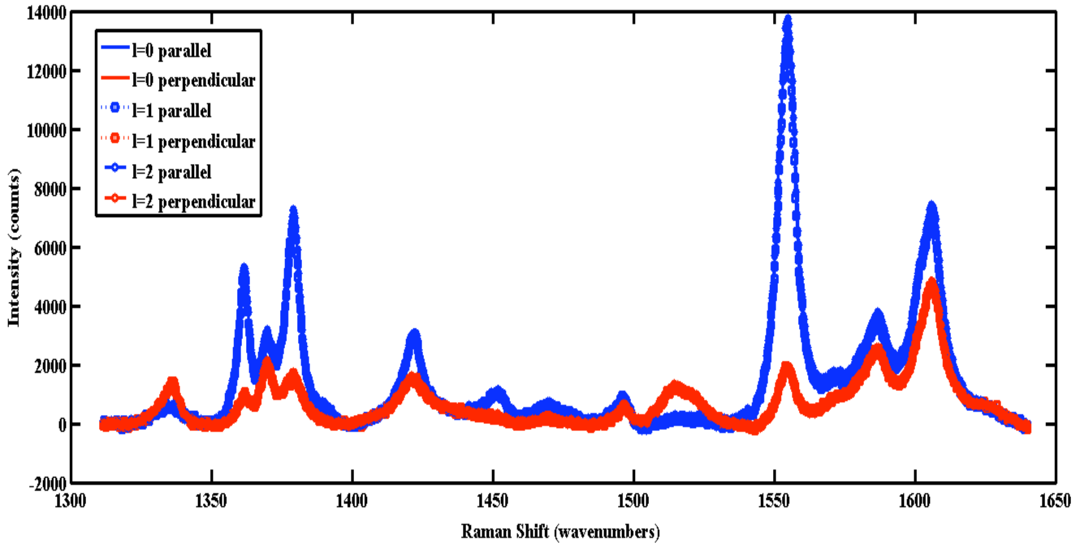

FIG. 6.5. Room temperature scattering of Fe(III)TPPCl in 1:1 mixture of toluene and CH_2Cl_2 excited at 514.5 nm. There is no detectable difference in the scattering from any of the excited non-totally symmetric and anomalously polarized vibrations in this region.

Discussion

Both in Ref. [1] and the extension from Chapters 2 and 3, predictions are made concerning the ability of LG beams to change the single molecule vibrational behavior of a large ensemble of molecules associated with a dipole allowed electronic transition. The extension of the Ref. [1] interaction Hamiltonian in Chapters 2 and 3 makes very specific predictions for changes in the intensity of totally and vibrations measured in a resonance-enhanced Raman scattering experiment. In the experimental tests, however, changes in the intensity of totally or non-totally symmetric vibrations in two different molecular systems are not observed when different excitation beams are incident on a large ensemble of molecules.

For $Fe^{(III)}$TPPCl, FIG. 6.6 shows the difference in the scattered intensity from 4 vibrations, 1234 cm^{-1}, 1362 cm^{-1}, 1454 cm^{-1} and 1554 cm^{-1}, between l=0 and l=2, 413.1 nm excitation beams. This difference is zero within the noise of the measurement.

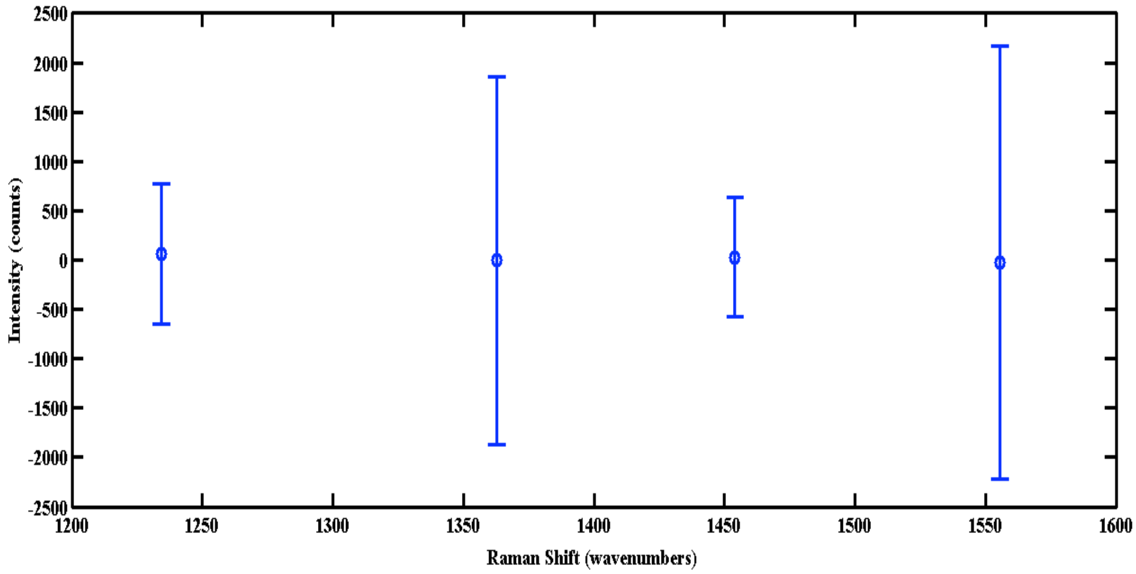

FIG. 6.6. Difference between l=0 and l=2 incident laser modes in resonance Raman scattering from Fe$^{(III)}$TPPCl in 1:1 mixture of toluene and CH_2Cl_2 excited at 413.14 nm at four peaks: 1234 cm^{-1}, 1363 cm^{-1}, 1454 cm^{-1} and 1555 cm^{-1}

FIG. 6.7 shows the same information of the 1337 cm^{-1}, 1516 cm^{-1}, 1524 cm^{-1} and 1555 cm^{-1} vibrations excited at 514.5 nm on the first vibronic overtone of the Q resonance. While it looks to one's eye that the difference in the mean intensity between a l=0 and l=2 excitation beam is consistently below zero, within the noise of the measurement the difference is also zero.

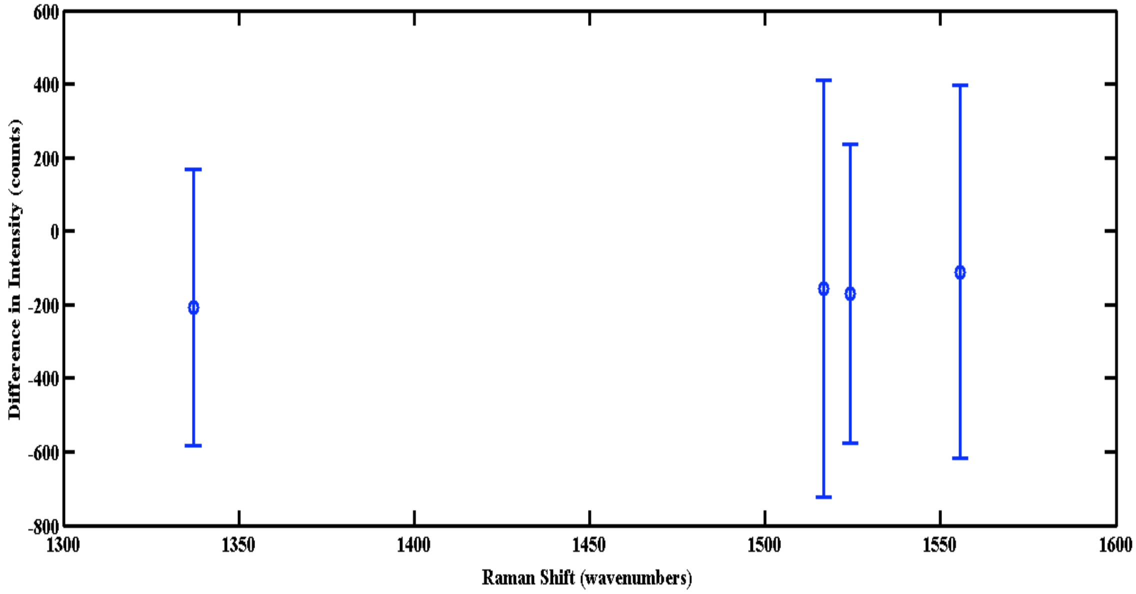

FIG. 6.7. Difference between l=0 and l=1 incident laser modes in resonance Raman scattering from Fe$^{(III)}$TPPCl in 1:1 mixture of toluene and CH_2Cl_2 excited at 514.54 nm at four peak: 1337 cm^{-1}, 1516 cm^{-1}, 1524 cm^{-1} and 1555 cm^{-1}

Based on the theoretical derivations and experimental evidence found, one can identify possible explanations for this outcome, two of which are of interest here. First, the derivation of the interaction Hamiltonian used to make the predictions tested with the above experiments (or any previous derivations from which it is based) is incorrect. This would mean the predictions themselves are incorrect and one should not expect to see the predicted changes in experimental data.

In exploring the incorrectness of the derivation of the second order perturbative corrections leading to light scattering processes, there is an important assumption worth exploring further. As pointed out in Chapter 3, this extension is only taking terms in the effective molecular polarizability in which the interaction Hamiltonian of Ref. [1] is used in the excitation transition matrix elements. The spontaneous scattering of a photon cannot occur into a LG mode, given the LG modes do not serve as a basis for the vacuum states of an EM field.

The most rigorous derivation of the second order corrections to a molecule's energy due to the LG interaction Hamiltonian might have to include terms in which there is a LG optical coupling in both the excitation and scattering processes. This would mean including all the terms of the state tensor from Eqn. (3.20). Experimentally, all of the processes implied by the terms in Eqn. (3.20) could be explored via a stimulated Raman experiment. In such an experiment, both the exciting and stimulating EM fields would need to come from LG beams, which could easily be undertaken with phase plates in a CSRS/CARS experiment.

Given that spontaneous resonance Raman scattering is not the most rigorous possible test of the predictions of the vibrational behavior of a molecule based on interaction Hamiltonian of Ref. [1], one cannot substantiate predictions with the most rigor. It may be that the assumptions on the nature of the light-matter interaction itself preclude the ability to test those predictions using a spontaneous coupling to the vacuum field.

The second possibility explaining the null result in the above experiments is that the above predictions are correct, but these experiment results have provided an upper limit on the magnitude of the contribution of terms that lead to the ‘new’ physical processes explored here and Ref. [1]. Since the interference effect derived and discussed in Chapter 3 picks up intensity from the cross term between the first and fourth terms in eqn. (3.27b), one would expect that this process to contribute more substantially than the square of the fourth term. If this were the case, these experiments provide the upper limit on the coefficient of the fourth term of eqn. (3.27b). This upper limit is between 1/10000 and 1/1000 times the coefficient of the first term. This provides a ceiling for the effect on the molecules’ vibrational behavior of a LG beam during an electronic transition among a large ensemble of those molecules. Further scattering experiments exploring lower noise floors and higher SNR’s will either detect the effects predicted here or extend the ceiling for relative magnitude of the effects to an even lower limit.

If the derivations of Chapter 2 and Chapter 3 are correct in its assumptions then there is a significant portion of the volume illuminated by the exciting LG beam in which the radial variation of the laser beam is coupled to the quantized vibrations of the molecule. If a substantial portion of the illuminated molecules is coupled to the radial variation of the LG beam, then it is meaningful to equate the SNR from the above measurements with a real ceiling of the interference effect derived in Chapter 3.

If the molecules must interact with the LG beam on its axis, then the relative magnitude of the contribution of the LG coupling can be substantially larger. The fact that such a coupling is not measureable would mean that the background of all the molecules that do not ‘sense’ such a coupling make a much more sensitive measurement necessary. Such cases would likely necessitate sensitivity down to 1 part in 10^{15} or smaller, depending on the resonance enhancement of the particular vibration of interest.

Conclusions

The extension of the LG interaction Hamiltonian of Ref. [1] to the inelastic light scattering of neutral diatomic and complex polyatomic molecules was tested with the resonantly enhanced Raman scattering of two molecular systems in condensed phase: I_2 and $Fe^{(III)}$TPPCl. Taking the appropriate terms from the state tensor derived in Chapter 3, resonance Raman scattering provides enough sensitivity to detect effects 1000 to 10000 times smaller than the plane wave interactions.

Given the detection limit of these measurements, effects due the LG excitation on the vibrational behavior of the totally symmetric vibrations of I_2 or $Fe^{(III)}$TPPCl dissolved in different solvents at room temperature were not detected. Although these experiments point to questioning the correctness of the interaction Hamiltonian of Ref. [1], more rigorous experimental tests of the predictions of Chapter 3 are possible. More rigorous experiments could be conducted with LG beams both exciting and scattering processes in a stimulated Raman scattering experiment.

References

1. A. Alexandrescu, D. Cojoc and E. Di Fabrizio, Phys. Rev. Lett. **96** (24) (2006).
2. V. V. Kotlyar, A. A. Almazov, S. N. Khonina, V. A. Soifer, H. Elfstrom and J. Turunen, J. Opt. Soc. Am. A-Opt. Image Sci. Vis. **22** (5), 849-861 (2005).
3. S. S. R. Oemrawsingh, J. A. W. van Houwelingen, E. R. Eliel, J. P. Woerdman, E. J. K. Verstegen, J. G. Kloosterboer and G. W. t Hooft, Appl. Optics **43** (3), 688-694 (2004).
4. T. Rush, R. Kumble, A. Mukherjee, M. E. Blackwood and T. G. Spiro, Journal of Physical Chemistry **100** (29), 12076-12085 (1996).

Chapter 7:
Angular Momentum Conservation in Classical Electromagnetic Scattering: Induced Transparency and Amended Nano-Plasmonics

Introduction

In this chapter, the scattering of beams carrying orbital angular momentum (OAM) from a spherical metal nano-particles is treated analytically using a projection of the participating EM fields onto traditional angular momentum states of the electromagnetic field.[1] This treatment helps to understand the ways in which the incident OAM affects the intensity and spatial variation of the scattered electric and magnetic fields in limit of a metallic particle smaller than an optical wavelength. Calculations show that the OAM of the incident field is conserved in the scattered and internal fields resulting in interesting changes to the scattering cross-section and plasmonic response of a sub-micron particle.

First, the electromagnetic response is calculated for an arbitrarily sized particle. The analytical results are then applied to the scattering of a sub-micron particle. The effects of OAM on the light scattering from a metal particle are contrasted against the same interaction with a circularly polarized plane wave. This comparison aids in more fully understanding the applicability of beams carrying OAM in nano-structure technologies.

For a small particle, the scattering of an incident p=0, l=1 right circularly polarized (RHP) LG beam leads to the leading multipole term in the scattered field expansion that possesses an angular distribution with vanishing amplitude at specific observation angles. This case contrasts that of a RHP plane wave in which there are no such angles. These zero intensity angles in the angular distribution of the scattered power are due to the presence of OAM in the scattered fields.

Plasmonic effects associated with metallic particles of sub-micron radius are also treated. Metallic particles in this size limit show substantially different absorption and scattering behavior than the same materials in bulk. These changes are due to the dominance of the surface plasmon optical response.[2] This chapter shows that the incident angular momentum density changes the lowest order contribution to the field internal to a nanometer-sized metallic particle. This consequence of the conservation of angular momentum changes the plasmonic response of the particle in two interesting ways.

First, higher plasmonic surface and volume modes of the particle confine more of the excited fields near the metal-dielectric interface.[2] The enhanced confinement of the plasmonic response to the metal-dielectric interface is useful for several applications. In the nano-scale limit, the localized excitation of collective electronic response in light-absorbing nano-scale metallic structures have opened doors to sub-diffraction limited photonic devices. Such structures are of great interest in a variety of fields ranging from chemical sensing to energy science and telecommunication applications.[3-9] In particular, the utility of these structures to chemical sensing comes from the increased intensity of the EM fields near the metal-dielectric interface. By confining the nano-scale plasmonic response closer to the metal-dielectric surface, circularly polarized LG beams can play a significant role in advancing the identification and characterization of molecular systems of interest via surface-based spectroscopic techniques.

Also, the spatial variation of the higher order volume mode of sphere matches that of the transverse radial variation of the incident electric field. The matching of these modes strengthens the coupling between the incident and excited fields. Since the internal fields are excited coherently with the scattered fields, strong coupling between the incident and internal modes of the spherical particle also affects the multipole contributions to the scattered fields. In the small particle limit the dipole response of the particle dominates the scattering cross section. Matching the transverse spatial profile of the incident field to those of higher order volume modes of the sphere leads to dramatic attenuation of the dipole contribution to the scattering, making the particle virtually transparent to the light field.

Second, plasmon modes excited in the scattering process also contribution to determining the angular momentum state of the scattered fields. Each of the surface plasmon modes is resonant at different frequencies set by spherical geometry of the nano-structure. Therefore, different angular momentum states of the scattered field are resonant at different frequencies. From this perspective a model is developed to control attributes of the scattering spectra of plasmonic nano-spheres through the conservation of angular momentum. To achieve this control, fractional vortex beams with non-integer valued OAM density provide multiple lowest order multipole contributions to the scattered field, which are enhanced in coherent electromagnetic scattering. By providing interference between the different angular momentum states of the scattered fields, coherent light scattering of fractional OAM beams allows selective tailoring of specific attributes of plasmonic scattering spectra.

Classical Electromagnetic Scattering of LG Beams

The theory of classical electromagnetic scattering dates back to the turn of the 20th century. Mie was among the first to show the closed-form expressions for an EM field scattered by a small, spherical particle.[10] Since that time, the topic of light scattering from both conducting and dielectric particles has been revisited for a number of applications whose importance has waxed and waned over time. Recently, with ever-increasing techniques and technologies for fabricating a host of precision sub-micron material motifs, classical EM scattering has seen resurgence in importance in the optics community.

Mie's formal solution of Maxwell's equations for scattering of light by a homogeneous sphere can be cast in the form of vectors to see how changes in the incident field's angular momentum density affect the overall scattering intensity, the angular distribution of the scattered intensity as well as the angular momentum density of the scattered fields. Treatments of the scattering of LG beams using the Mie formalism have yet to address how changes in the incident field's angular momentum density affect that of the scattered fields or the plasmonic response of the scattering center. These studies have focused instead on utilizing the scattered field to characterize the incident field in the context of projections onto the complete set of LG modes.[11, 12]

A series summation of vector spherical harmonics represents general solutions to the Maxwell equations in an empty, source-free region of space filled with a dielectric medium.[1] That is the magnetic and electric fields, respectively, are written as,

$$\vec{H} = \sum_{m,n} \left[a_E(m,n) f_m(kr) \vec{X}_{mn} - \frac{i}{k} a_M(m,n) \vec{\nabla} \times g_m(kr) \vec{X}_{mn} \right] \tag{7.1a}$$

$$\vec{E} = \frac{\mu_d \omega}{k_d} \sum_{m,n} \left[a_M(m,n) g_m(kr) \vec{X}_{mn} + \frac{i}{k} a_E(m,n) \vec{\nabla} \times f_m(kr) \vec{X}_{mn} \right], \tag{7.1b}$$

where,

$$\vec{X}_{mn} = \frac{1}{\sqrt{m(m+1)}} \vec{L} Y_{mn}. \tag{7.2}$$

are the vector spherical harmonics. The vector operator L is the orbital angular momentum operator, Y_{mn} are the spherical harmonics, k is the wavevector of the EM field in question and f_m and g_m are linear combinations of first and second order spherical Hankel functions. The subscript d on both k and μ indicate the wavelength and magnetic permeability in this dielectric medium.

Calculating the appropriate electric and magnetic multipole moment coefficients (a_E and a_M, respectively) allows one to ‘transparently see’ the angular momentum states of a LG beam. A RHP, p=0, l=1 LG beam focused to it’s waist, w_0, traveling in the z-direction is

$$\vec{E}_{01} = (\hat{x} + i\hat{y}) E_0 \frac{r\sqrt{2}}{w_0} e^{-\frac{r^2}{w_0^2}} e^{i\phi} e^{ikz} \tag{7.3a}$$

$$\vec{H}_{01} = \frac{-i\vec{E}_{01} k_d}{\omega \mu_d} = -i(\hat{x} + i\hat{y}) E_0 \frac{r k_d \sqrt{2}}{\omega \mu_d w_0} e^{-\frac{r^2}{w_0^2}} e^{i\phi} e^{ikz}. \tag{7.3b}$$

in the same dielectric medium described above. At the beam’s waist one ignores the radius of curvature and Guoy phase of the beam, which complicate the analytical calculation of the electric and magnetic multipole coefficients of the incident fields.

After transforming the RHP polarization state of the beam into spherical coordinates, the electric and magnetic fields of the RHP p=0, l=1 LG beam can be written in terms of the vector spherical harmonics as

$$\vec{E}_{01} = \sum_{m=2}^{\infty} -i^{l} \sqrt{\frac{4\pi(2m+1)}{m(m+1)}} \frac{E_0\sqrt{2}}{kw_0}$$
$$\times \left[\exp\left[-\left(\frac{kr}{kw_0}\right)^2\right](kr)^2 j_m(kr)\vec{X}_{m2} + \frac{1}{k}\vec{\nabla}\times \exp\left[-\left(\frac{kr}{kw_0}\right)^2\right](kr)^2 j_m(kr)\vec{X}_{m2}\right] \qquad (7.4a)$$

$$\vec{H}_{01} = \frac{-i\vec{E}_{01}k_d}{\omega\mu_d} = \frac{-ik_d}{\omega\mu_d}\sum_{m=2}^{\infty} -i^{l} \sqrt{\frac{4\pi(2m+1)}{m(m+1)}} \frac{E_0\sqrt{2}}{Z_0 kw_0}$$
$$\times \left[-i\exp\left[-\left(\frac{kr}{kw_0}\right)^2\right](kr)^2 j_m(kr)\vec{X}_{m2} - \frac{i}{k}\vec{\nabla}\times \exp\left[-\left(\frac{kr}{kw_0}\right)^2\right](kr)^2 j_m(kr)\vec{X}_{m2}\right]. \qquad (7.4b)$$

Most notable about equations (7.4a) and (7.4b) is the fact that the summation over the index m in the expansion over the vector spherical harmonics begins with the value m=2. This is directly due to the fact that the RHP, p=0, l=1 LG beam carries two units of angular momentum along the propagation direction, z in this case. One unit of angular momentum is associated with the circular polarization of the fields while the other is associated with the helical structure of the beam's wave front, or the OAM, of the beam.

Had the EM fields of a LHP p=0, l=1 LG beam been derived using this method, the expansion of the fields would have began with the m=1 term. This is because the LHP state and l=1 helical phase front of the LG beam counter each other in that case and the units of the quantized angular momentum associated with each of these degrees of freedom cancel. Despite the fact that the opposite-handedness of the circular polarization and LG results in the beam carrying zero units of total angular momentum along the propagation direction, the absolute lowest order contribution to the scattering must be the dipole response. This corresponds to the m=1 state in the expansions in eqns. (7.1a) and (7.1b).

In order to understand how control of OAM can affect the scattered EM fields, a metal particle of radius a is positioned on the z-axis at the waist of an incident p=0, l=1 RHP LG beam. Under these conditions, the particle shares a common φ-axis with the incident LG beam, as has been treated similarly elsewhere[12]. This physical situation is seen in FIG. 7.1.

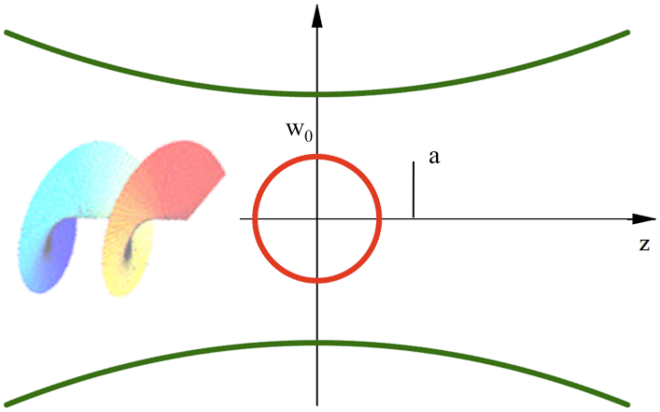

FIG. 7.1. Schematic of a LG laser beam of w$_0$ (green) incident on a metallic, absorptive nano-particle (red) of radius a. The particle and LG beam share a common z and φ-axes in spherical coordinates.

The polarization state of the incident field is then evaluated in the plane θ=π/2 in spherical coordinates since the LG beam is described as a TEM mode. Based on the incident LG field, the scattered field becomes

$$\vec{E}_{sc} = \sum_{m=2}^{\infty}\left[\alpha_+(m)h_m^{(1)}(k_d r)\vec{X}_{m,2} + \frac{\beta_+(m)}{k_d}\vec{\nabla}\times h_m^{(1)}(k_d r)\vec{X}_{m,2}\right] \tag{7.5a}$$

$$\vec{H}_{sc} = \frac{-ik_d}{\omega\mu_d}\sum_{m=2}^{\infty}\left[\beta_+(m)h_m^{(1)}(k_d r)\vec{X}_{m,2} + \frac{\alpha_+(m)}{k_d}\vec{\nabla}\times h_m^{(1)}(k_d r)\vec{X}_{m,2}\right]. \tag{7.5b}$$

from which the scattered field coefficients $\alpha_+(m)$ and $\beta_+(m)$ can be found using the appropriate boundary conditions. The fields internal to the sphere are,

$$\vec{E}_{in} = \sum_{m=2}^{\infty}\left[\gamma_+(m)j_m(k_p r)\vec{X}_{m,\,2} + \frac{\delta_+(m)}{k_p}\vec{\nabla}\times j_m(k_p r)\vec{X}_{m,\,2}\right] \tag{7.6a}$$

$$\vec{H}_{in} = \frac{-ik_p}{\omega\mu_p}\sum_{m=2}^{\infty}\left[\delta_+(m)j_m(k_p r)\vec{X}_{m,\,2} + \frac{\gamma_+(m)}{k_p}\vec{\nabla}\times j_m(k_p r)\vec{X}_{m,\,2}\right]. \tag{7.6b}$$

The subscript p on k and μ in eqn. (7.6b) indicate the wavevector and magnetic permeability of the illuminated particle.

In both sets of equations for the scattered and internal fields, the subscript + indicates that the incident field is right circularly polarized based on the convention in eqns. (7.3a) and (7.3b). It is important to point out that because the projection of the incident field onto the vector spherical harmonics begins with m=2, the projection of the scattered and internal fields onto the spherical harmonic basis set must begin with the same m-value. This is a direct consequence of the conservation of angular momentum.

The incident, scattered and internal fields obey the boundary conditions,[2]

$$E_{01}^{\theta}+E_{sc}^{\theta}=E_{in}^{\theta}, \qquad (7.7a) \qquad E_{01}^{\phi}+E_{sc}^{\phi}=E_{in}^{\phi}, \qquad (7.7b)$$

$$H_{01}^{\theta}+H_{sc}^{\theta}=H_{in}^{\theta}, \qquad (7.7c) \qquad H_{01}^{\phi}+H_{sc}^{\phi}=H_{in}^{\phi}, \qquad (7.7d)$$

Solving the boundary conditions at r = a, the scattered and internal field coefficients become,

$$\alpha_{+}(m) = -i^{m}\frac{2E_0\sqrt{2}}{k_d w_0}\sqrt{\frac{2m+1}{m(m+1)}\frac{(m-2)!}{(m+2)!}}$$

$$\times\left[\frac{\frac{k_p}{\omega\mu_p}\exp\left[-\left(\frac{\rho}{k_d w_0}\right)^2\right]\rho^2 j_m(\rho)\frac{1}{\rho_1}\frac{d}{d(\rho_1)}\left\{\rho_1 j_m(\rho_1)\right\}+\frac{k_d}{\omega\mu_d}\frac{1}{\rho}\frac{d}{d(\rho)}\left\{\exp\left[-\left(\frac{\rho}{k_d w_0}\right)^2\right](\rho)^3 j_m(\rho)\right\}}{\frac{k_p}{\omega\mu_p}h_m^{(1)}(\rho)\frac{1}{\rho_1}\frac{d}{d(\rho_1)}\left\{\rho_1 j_m(\rho_1)\right\}-\frac{k_d}{\omega\mu_d}j_m(\rho_1)\frac{1}{\rho}\frac{d}{d(\rho)}\left\{\rho h_m^{(1)}(\rho)\right\}}\right], \quad (7.8a)$$

$$\beta_{+}(m) = -i^{m}\frac{2E_0\sqrt{2}}{k_d w_0}\sqrt{\frac{2m+1}{m(m+1)}\frac{(m-2)!}{(m+2)!}}$$

$$\times\left[\frac{\frac{k_d}{\omega\mu_d}\exp\left[-\left(\frac{\rho}{k_d w_0}\right)^2\right]\rho^2 j_m(\rho)\frac{1}{\rho_1}\frac{d}{d(\rho_1)}\left\{\rho_1 j_m(\rho_1)\right\}+\frac{k_p}{\omega\mu_p}\frac{1}{\rho}\frac{d}{d(\rho)}\left\{\exp\left[-\left(\frac{\rho}{k_d w_0}\right)^2\right](\rho)^3 j_m(\rho)\right\}}{\frac{k_d}{\omega\mu_d}h_m^{(1)}(\rho)\frac{1}{\rho_1}\frac{d}{d(\rho_1)}\left\{\rho_1 j_m(\rho_1)\right\}-\frac{k_p}{\omega\mu_p}j_m(\rho_1)\frac{1}{\rho}\frac{d}{d(\rho)}\left\{\rho h_m^{(1)}(\rho)\right\}}\right], \quad (7.8b)$$

$$\gamma_{+}(m) = -i^{m}\frac{2E_0\sqrt{2}}{k_d w_0}\frac{k_d}{\omega\mu_d}\sqrt{\frac{2m+1}{m(m+1)}\frac{(m-2)!}{(m+2)!}}$$

$$\times\left[\frac{\frac{1}{\rho}\frac{d}{d(\rho)}\left\{\exp\left[-\left(\frac{\rho}{k_d w_0}\right)^2\right]\rho^4 j_m(\rho)h_m^{(1)}(\rho)\right\}}{\frac{k_p}{\omega\mu_p}h_m^{(1)}(\rho)\frac{1}{\rho_1}\frac{d}{d(\rho_1)}\left\{\rho_1 j_m(\rho_1)\right\}-\frac{k_d}{\omega\mu_d}j_m(\rho_1)\frac{1}{\rho}\frac{d}{d(\rho)}\left\{\rho h_m^{(1)}(\rho)\right\}}\right], \quad (7.8c)$$

$$\delta_{+}(m) = -i^{m}\frac{2E_0\sqrt{2}}{k_d w_0}\frac{k_d}{\omega\mu_d}\sqrt{\frac{2m+1}{m(m+1)}\frac{(m-2)!}{(m+2)!}}$$

$$\times\left[\frac{\frac{1}{\rho}\frac{d}{d(\rho)}\left\{\exp\left[-\left(\frac{\rho}{k_d w_0}\right)^2\right]\rho^4 j_m(\rho)h_m^{(1)}(\rho)\right\}}{\frac{k_d}{\omega\mu_d}h_m^{(1)}(\rho)\frac{1}{\rho_1}\frac{d}{d(\rho_1)}\left\{\rho_1 j_m(\rho_1)\right\}-\frac{k_p}{\omega\mu_p}j_m(\rho_1)\frac{1}{\rho}\frac{d}{d(\rho)}\left\{\rho h_m^{(1)}(\rho)\right\}}\right]. \quad (7.8d)$$

where $\rho = k_d a$ and $\rho_1 = k_p a$

Scattering in the Small Particle Limit ($k_d a << 1$)

For the case in which $k_d a << 1$, the coefficients α and β can be simplified using the asymptotic forms of the spherical Bessel and Hankel functions. The Gaussian roll-off of the laser profile can also be ignored since $k_d a << k w_0$ in this limit. Using the first possible m-value in the expansion to match the fact that the n-values begin with n=2, the angular distribution of the scattered power per unit solid angle becomes,

$$\frac{dP}{d\Omega} = \frac{E_0^2 a^2}{w_0^2}\left(\frac{k_d}{\omega\mu_d}\right)^2 \frac{5}{1458}\rho^{12}\left[\frac{13}{10}\left(1-\cos^4\theta\right)-\sin^2\theta\cos\theta\right]. \qquad (7.9)$$

The angular dependence of this scattering of a RHP p=0, l=1 LG scaled to the value of the pre-factor in eqn. (7.9) is compared to that caused by an incident RHP plane wave scaled to its pre-factor is shown in FIG. 7.2.[1]

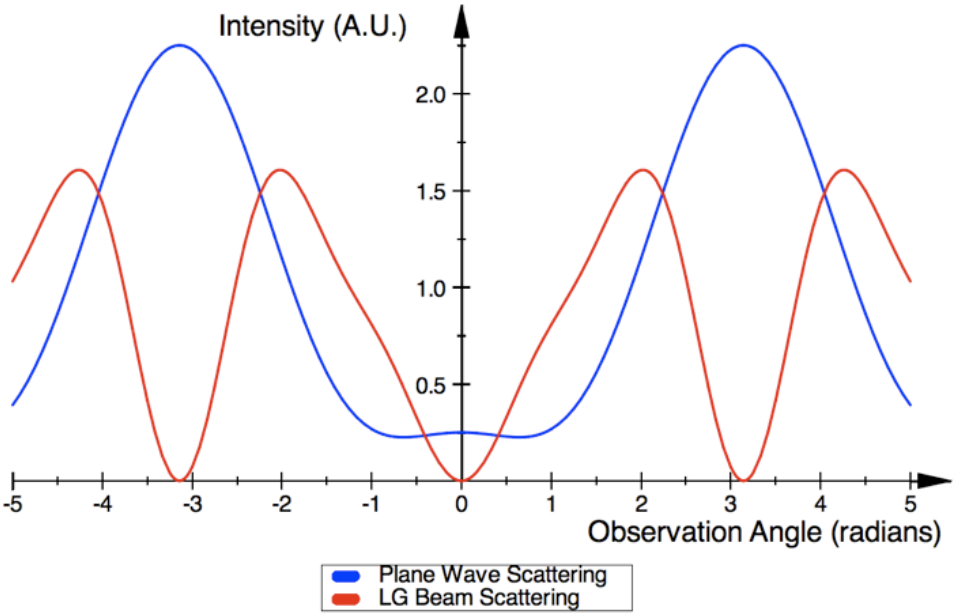

FIG. 7.2. Comparison of angular dependence of scattered power per unit solid angle induced by RHP plane wave (blue) and RHP p=0, l=1 LG beam (red). The scattering from the LG beam goes to zero intensity at θ=0 and θ=π.

FIG. 7.2 shows that angularly distributed power scattered off the particle by a RHP plane wave contains no observation angle at which the intensity zero. In contrast, there are two such directions for a RHP p=0, l=1 LG beam. In both the forward and backward directions relative to the propagation direction of the incident field there is no scattered light.

Based on eqn. (7.9), one can also say that the total scattering intensity due to the incident LG beam from a metallic particle is extremely small. For $k_d a$=0.1, the intensity of the scattered power is weighted by a factor less than 10^{-12}. As $k_d a$ becomes smaller, so does the scattering intensity. This means that the incident LG beams interacts with an extremely small effective scattering cross-section. In comparison to the scattering of circularly polarized plane waves, these small particles seems transparent to the incident LG beam.

Transparency to incident electromagnetic waves is a topic of central focus in plasmonics and, by extension, metamaterials.[13-15] Researchers are developing new nano-structures showing bulk properties not found in nature to pass light with little to no disruption of the parameters of its fields. Transparency due to the conservation of angular momentum has yet to be analyzed in the broader optical science community, but could play a role in protocols for optical switching and signal processing.

It has been pointed out in the literature that amplitude of the electric field of a LG beam is very small at its center.[16] Since the particle of interest is being placed at the center of the LG beam, one may regard the magnitude of the scattered field as tied to the fact that the incident field intensity is very small at such a point. Upon reflection different, and more interesting, effects may be dominating the magnitude of the observed scattering.

First, in the limit that the particle is very small compared to the wavelength of light the dipole response of the particle dominates the scattering cross-section. The scattering from higher order multipole moments is strongly attenuated in this size limit. As seen in the lowest order contribution to eqns. (7.8a) through (7.8d), the angular momentum density of the incident circularly polarized LG beam is conserved in both the scattered and internal fields. Since this conservation demands that higher order multipole moments are excited in the scattering process, a circularly polarized LG beam does not scatter from the dipole moment of the particle. The LG beam only excites moments of the particle that very weakly contribute to scattering of a particle in this size limit. Therefore, the excitation of these higher order multipole moments of the particle leads to a very small overall scattering intensity.

Second, the field inside the particle is defined by volume modes which have been described by the vector spherical harmonics in eqns. (7.7a) and (7.7b). In the limit that the wavelength of the incident light is much longer than the radius of the sphere the spherical Bessel functions in the expansions take their asymptotic form, as described above. In this power law limit, the curl term dominates eqns. (7.7a) and (7.7b). From that conclusion, the spatial variation of the electric field is approximated as

$$\vec{E}_{in} \propto \sum_{m=2}^{\infty} \vec{\nabla} \times j_m\left(k_p r\right) \vec{X}_{m,\,2} \sim \sum_{m=2}^{\infty} \left(k_p r\right)^{m-1}. \qquad (7.10)$$

Again, the expansion of the internal fields onto the vector spherical harmonics conserves the incident angular momentum. The presence of orbital angular momentum in the incident field causes this expansion to begin with the value m=2. This spatial variation of the internal electric field is a direct consequence of the presence of both orbital and polarization forms of electromagnetic angular momentum in the incident field. An incident circularly polarized plane wave elicits a uniform internal electric field to lowest order due to the dipole response of the particle in the long wavelength limit, the m=1 case. In this sense, the orbital angular momentum density of the incident beam amends the response of the metallic sphere. Conserving angular momentum necessitates that the lowest order contribution to the internal EM fields comes from a higher order volume mode. This higher order volume mode is defined by functionally different spatial variation, which confines more of the internal field to the metal-dielectric interface.

In response to an incident p=0, l=1 LG beam, the lowest order contribution to the internal EM fields has the value m=2. From eqn. (7.10), electric field internal to the particle due to this term will increase linearly from zero at the center of the sphere to its maximum at the interface between the metal and dielectric. Physically, this corresponds to confining more of the amplitude of the internal field close to this interface than the m=1 state, or dipole moment of the particle, which displays a spatially homogeneous internal electric field.

Of more interest to the discussion of angular momentum-induced transparency, the dipole moment volume mode matches the field profile of an incident $TEM_{00.}$ That is, on length scales small compared to the incident wavelength, the transverse profile of an incident TEM_{00} mode matches that of the homogeneous dipole volume mode. Mode-matching plays an important role in the coupling of propagating EM fields to wide variety of optical devices ranging from waveguides to optical fibers to photonic crystals.[17-19]

The matching of the transverse profile of the incident beam to the radial variation of the volume modes strongly couples the two modes. Given that the internal and scattered fields are excited coherently, the excitation of internal fields due specific multipole moments also excites scattered fields from these same moments. This mode-matching leads to stronger coupling between these fields than would otherwise occur simply due to angular momentum conservation considerations. However, the mode-matching changes in the case of incident LG beams and higher order volume modes.

In the case of an incident circularly polarized LG beam treated above, the linear radial variation of the higher order volume mode matches the linear transverse radial variation of the incident LG electric field. Increasing the l-value of the incident beam increases the orbital angular momentum in the incident field as well as the power law dependence of the transverse mode on the radial coordinate, r. Applying the same treatment carried above for an incident p=0, l=2 RHP LG beam results in an expansion onto the vector spherical harmonics that begins with the value m=3. Conservation of angular momentum causes a quadratic radial dependence in the lowest possible excited surface plasmon mode. The radial variation of this higher order volume mode again matches the transverse radial variation of the incident p=0, l=2 LG mode.

If one were to continue to increase the l-value of the incident LG mode, one would find that the radial variation of the electric field continues to match the transverse radial variation of the incident LG electric field. This remains the case as long as the particle is fixed at the center of the transverse mode. However, in the case of a small particle the higher order multipole moments make a very small contribution to the overall charge density. Due to these small contributions, there is very little potential for coupling from mode-matching between the transverse profile of the LG beam and that of the higher order volume modes. Therefore, the enhancement to the scattered fields due to the mode-matching of the dipole volume mode to the transverse profile of an incident TEM_{00} beam is also lost in the case of an incident LG beam. The loss of this enhancement further reduces the magnitude of the scattering by the LG fields and further induces transparency in the particle.

Spectral and Coherent Control of the Surface Plasmon Response with OAM

The previous section shows that the volume modes of a sub-micron sphere must preserve the angular momentum density of the incident fields. This conservation leads the excitation of higher order volume electromagnetic modes of the sphere. However, the conservation of angular momentum also plays a role in modulating the excitation of the localized surface modes of the sphere. When the real part of the electric susceptibility of the metal sphere takes on certain values ($\varepsilon < -1$) and the index of refraction of the surrounding material is larger than that of the vacuum, electromagnetic modes are excited along the interface between the metal and dielectric. These are known as surface-plasmon modes.

There is a distinct angular momentum associated with each of the surface-plasmon modes excited on a spherical particle. The angular momentum associated with each of the surface-plasmon modes manifests itself as its distinct resonant frequency. At each frequency resonant associated with a distinct angular momentum state, the electric susceptibility satisfies the relation,

$$\varepsilon(\omega_m) = -\left(\frac{m+1}{m}\right). \qquad (7.11)$$

where m signifies the angular momentum state of the spherical surface-plasmon modes.

Fractional vortex beams have been theorized and fabricated in the lab.[20] These beams contain a non-integer OAM density and are thought of as a linear superposition of the integer OAM beams. Using a fractional vortex beams as linear superposition of OAM states and the conservation of angular momentum, one can excite different angular moment states of a plasmonic nano-sphere as lowest order contributions to the scattered field. Since each of the angular momentum states is associated with a different resonant frequency, fractional vortex beams tailor the scattering spectra produced by the plasmonic nano-sphere.

A simple model of a fractional vortex beams treats them as a sum of plane waves that each possess a l-dependent vortex structure produced by azimuthal phase variation. The electric of this simple fractional vortex beam is,

$$\vec{E}(l)_{inc} = \sum_{l=l_{\min}}^{l_{\max}} \vec{E}_0(l) g(l) e^{il\varphi} e^{ikz}. \qquad (7.12)$$

The factor g(l) is a distribution that determines the weighted amplitude of each component of the incident vortex beam.

To test how OAM controls plasmonic spectra, this electric field is incident on metallic nano-particle of radius a with an electric susceptibility, ε_p, embedded in a dielectric material with a purely real electric susceptibility, ε_d, as shown in FIG. 7.1. From eqn. (7.7b) and using the Drude model to explain the frequency dependent relative susceptibility ($\varepsilon=\varepsilon_p/\varepsilon_d$), the electric multipole scattering coefficient becomes,[21, 22]

$$\beta^{(m)}(\omega) = \sum_m E_0 g(m) \sqrt{\frac{4\pi(2m+1)}{m(m+1)}} \frac{(ka)^{2m+1}}{\left[(2m+1)!\right]^2} \left\{ \frac{\omega_m^2}{\omega^2-\omega_m^2+\gamma^2} + \frac{i\gamma}{\omega-\omega_m} \frac{\omega_m^2}{\omega^2-\omega_m^2+\gamma^2} \right\} \qquad (7.13)$$

where the limit that ka<<1 has simultaneously been invoked. The total scattering cross-section for Rayleigh scattering is,

$$Q_{sc} = \frac{1}{(ka)^2} \sum_m (2m+1) \left[\left|\alpha^{(m)}(\omega)\right|^2 + \left|\beta^{(m)}(\omega)\right|^2 \right] \qquad (7.14)$$

allowing one to calculate the surface-mode scattering spectrum for different fractional vortex modes.

FIG. 7.3 shows the spectrum scattered by a broadband fractional vortex beam from a gold nano-sphere with population in the l=3, 4, 5, and 6 states [g(3)=0.234, g(4)=0.26, g(5)=0.26, and g(6)=0.234] for three different values of ka. Since each multipole moment has a distinct resonance frequency, a broadband light source is used to excite all modes resonant with the incident OAM states simultaneously. The frequency axis has been scaled to gold's plasma frequency (ω_p=2183 THz) as well as gold's electron dissipation rate due to scattering (γ=6.46 THz).[23]

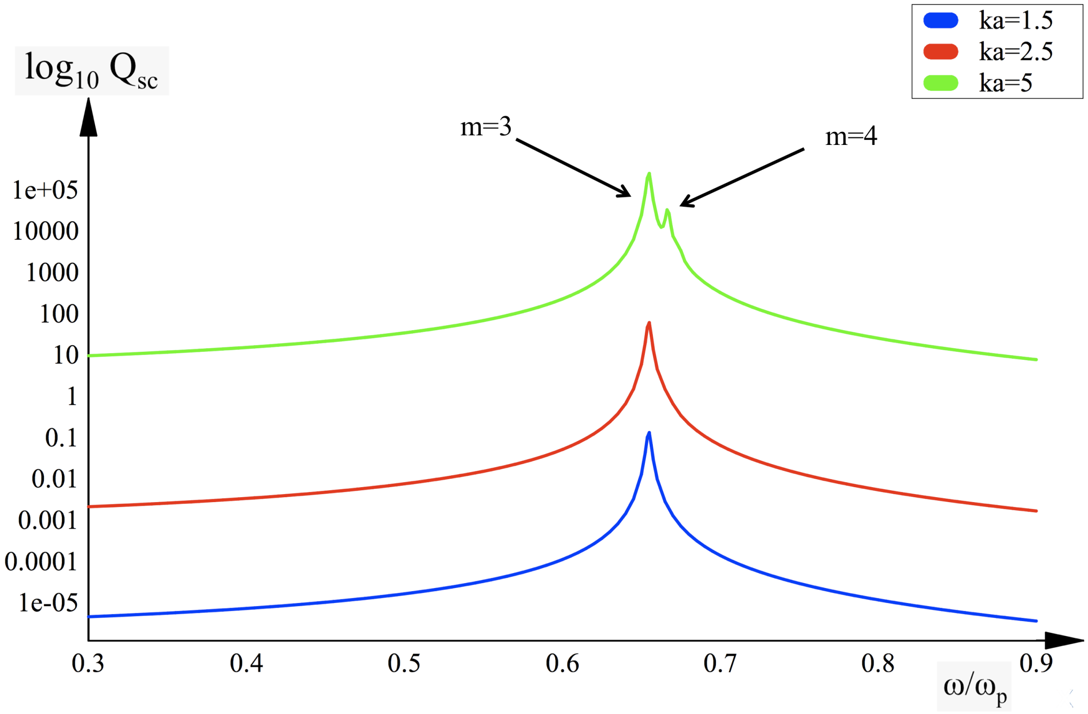

FIG. 7.3 Scattering of broadband fractional vortex beam with l=3,4,5, and 6 states. Only m=3 scattering state is visible due to attenuation of higher order modes in the Rayleigh limit.

Despite population in 4 distinct OAM states, only the scattering from the m=3 angular momentum state appears in the spectrum. The modes with higher angular momentum states than m=3 are attenuated strongly enough by the nature of Rayleigh scattering in the small particle limit that they do not appear in the spectrum.

FIG 7.4 shows the scattering from the same gold nano-particle in the case of a different broadband fractional vortex beam with population in the l=1, 2, and 3 states [g(1)=0.01, g(2)=0.04 and g(3)=0.95].

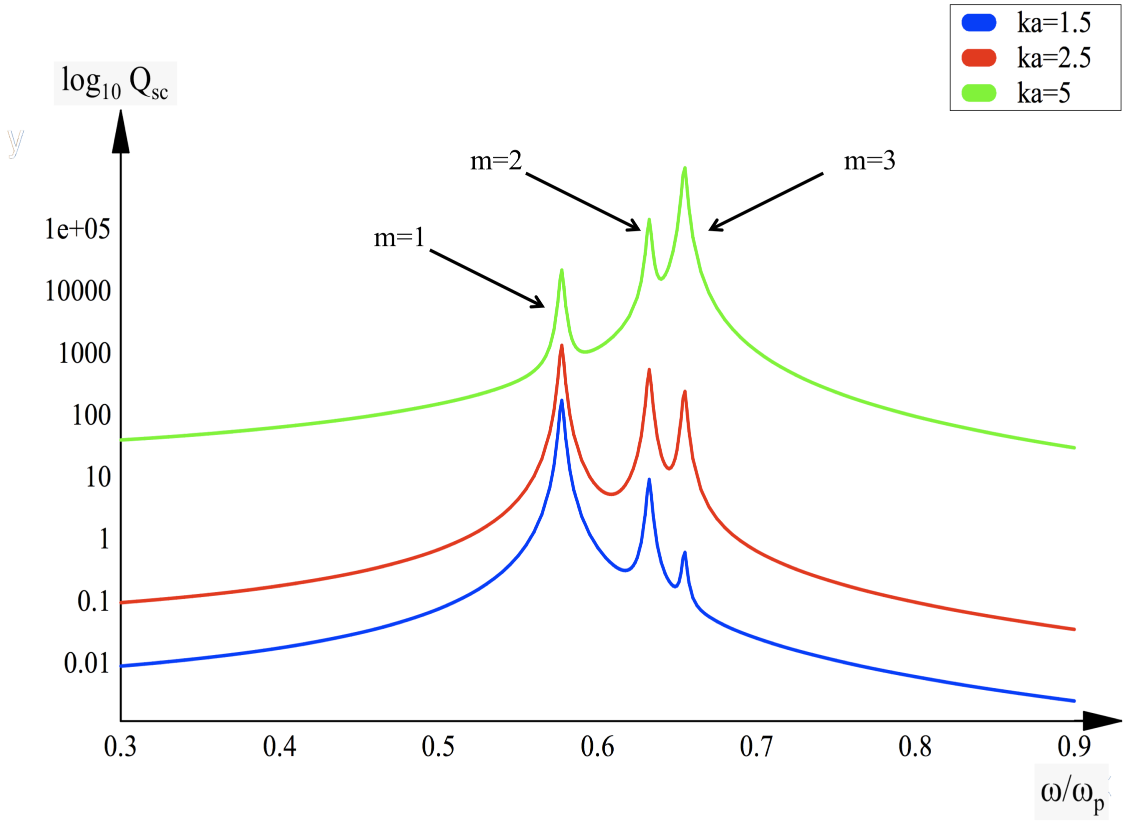

FIG. 7.4 Scattering of broadband fractional vortex beam with l=1, 2, and 3 states. Higher order multipole moments begin to appear as the size of the particle is increased.

In this case, the m=1 state dominates the spectra, but higher order peaks begin to appear as the particle radius increases. As the particle size increases, the Rayleigh limit of dipole-dominated scattering becomes less correct. This allows higher order mulitpole contributions to become larger and appear in surface-plasmon scattering spectra.

In a similar fashion to the proposal to change to resonant quantum mechanical light scattering with LG beams presented in Chapter 3, interference between strongly and weakly allowed transitions provides the mechanism for the control of these scattering spectra. In this case the very strong m=1 state in FIG. 7.4 interferes with higher order multipole moments as a mechanism towards optical control. In mathematical terms, interfering the scattering of different angular momentum states multiplies the small contribution of the higher order modes by that of the dominant dipole to produce enhanced features from those higher order moments.

Coherent electromagnetic scattering provides the ability to do just that. The interference effect associated with two forms of coherent electromagnetic scattering have been extensively studied: Radio Backscattering (RBS) and Forward Scattering (FS).[2, 5, 21] The cross-section for RBS is,

$$Q_{RBS} = \frac{1}{(ka)^2}\left|\sum_m (2m+1)(-1)^m\left[\alpha^{(m)}(\omega)+\beta^{(m)}(\omega)\right]\right|^2. \qquad (7.15)$$

while that of FS is,

$$Q_{FS} = \frac{1}{(ka)^2}\left|\sum_m (2m+1)\left[\alpha^{(m)}(\omega)+\beta^{(m)}(\omega)\right]\right|^2. \qquad (7.16)$$

From inspecting eqns. (7.15) and (7.16) relative to eqn. (7.14) ones sees that while traditional Rayleigh scattering is a sum of squared multipole coefficients, RBS and FS come from the coherent squares of the sum of those multipole coefficients. This means that cross terms between different angular momentum states occur in RBS and FS and interference between these states plays a major role in modulating the scattering spectra.

FIG. 7.5 shows the RBS and FS of the same broadband fractional vortex beam as FIG. 7.4 for the case of a gold particle and ka=5.

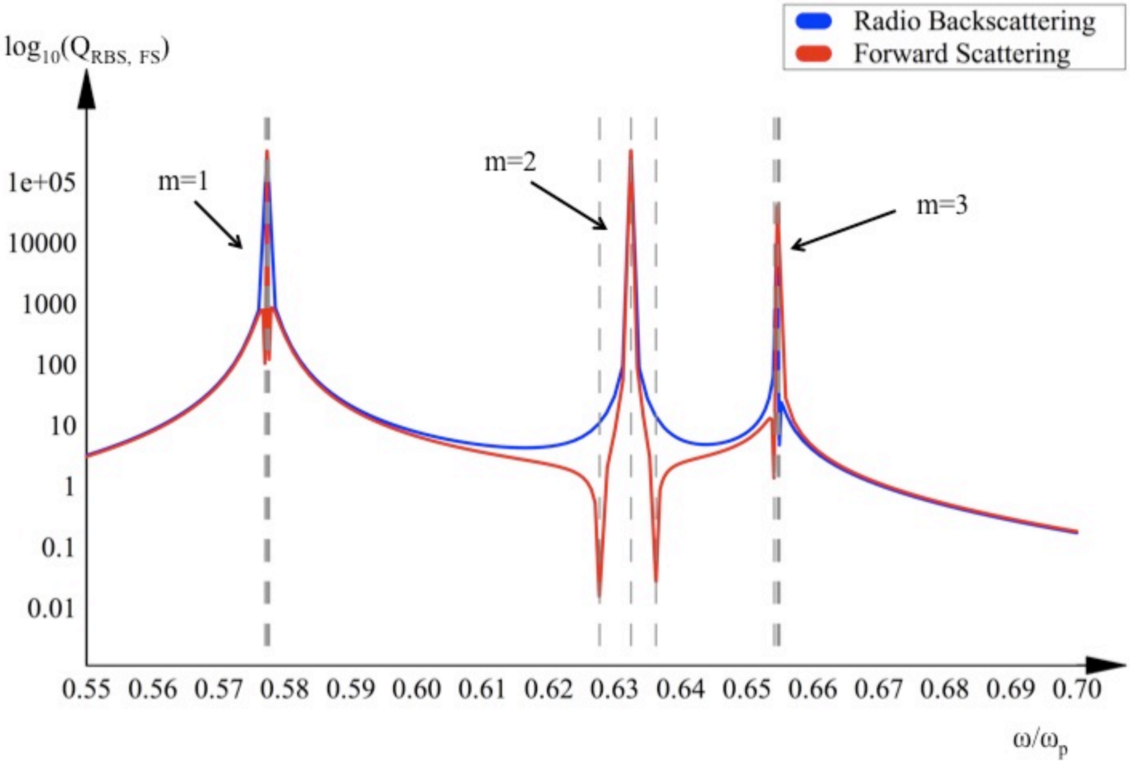

FIG. 7.5 Coherent Radio Backscattering (red) and Forward Scattering (blue) of a broadband fractional vortex beam containing population in the l=1, 2, and 3 OAM [g(1)=0.01, g(2)=0.04 and g(3)=0.95] states from a gold particle. Higher order multipole contributions are enhanced due to interference with the dominant dipole contribution.

Two features of FIG. 7.5 are worth noting here. First, in the Rayleigh or normal scattering limit, frequencies at the exact surface plasmon mode resonances are not real, but virtual.[2] This is because the denominator of the scattering cross-section equals zero at these frequencies. The dashed gray lines in FIG. 7.5 indicate those frequencies at which the denominator of the coherent scattering cross-section equals zero and explodes to an indeterminable value. Since different angular momentum states with differing resonant frequencies interfere to produce coherent scattering, several frequencies occur at which the denominators of eqns. (7.15) and (7.16) go to zero.

Second, m=3 peak in the spectra of FIG. 7.5 display asymmetric lineshapes for each form of coherent scattering. Fano resonances play an important role in the scattering and extinction spectra of plasmonic structures and metamaterials constructed from metallic nano-structures.[5] The lineshapes in FIG. 7.5 could mean that a Fano resonance is playing a role in the scattering, though a closer inspection of the explicit form of the scattering cross-section is necessary to reach that conclusion.

By controlling the distribution of weights in the different OAM state populations, one can modulate the positions of minima in the spectra, as well as tailor other spectral features. FIG. 7.6 compares the RBS spectra of three different fractional vortex beams all showing OAM populations in the l=1, 2, and 3 states, but possessing different weight distributions: #1) g(1)=0.01, g(2)=0.04, g(3)=0.95; #2) g(1)=0.25, g(2)=0.25, g(3)=0.5: #3) g(1)=0.5, g(2)=0.25, g(3)=0.25.

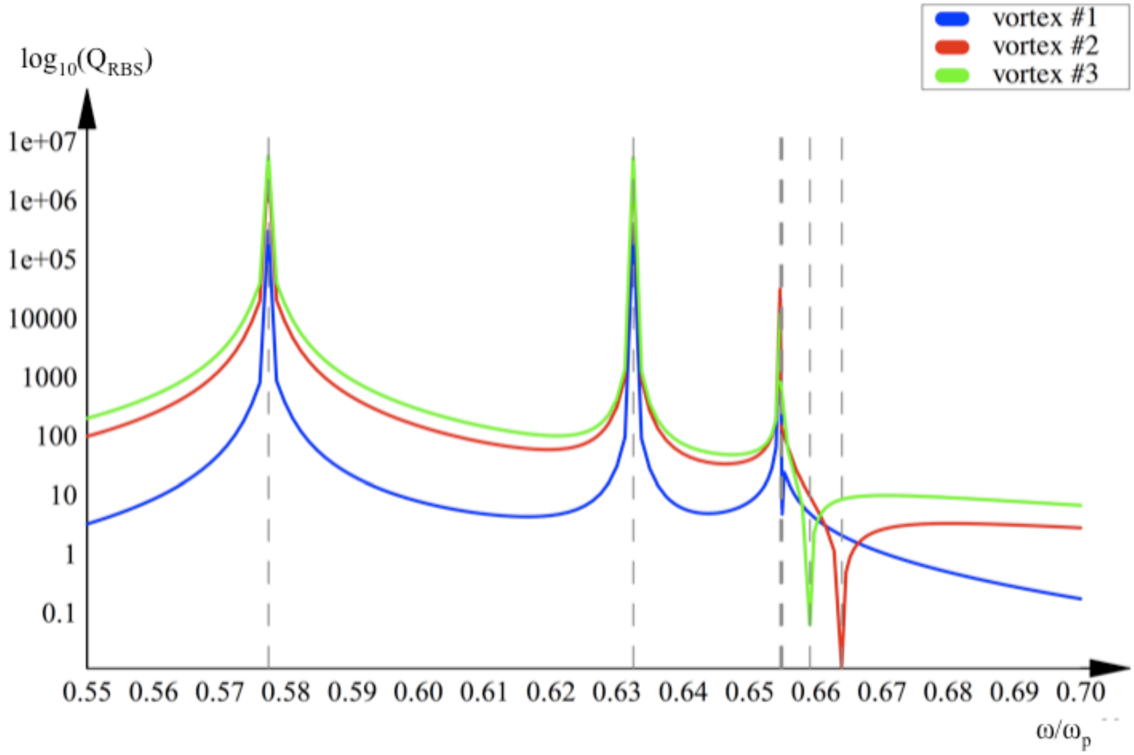

FIG 7.6. Comparison of the RBS scattering spectra for three different broadband fractional vortex beams that share population in the same OAM states, but differ in the weight of those states in the incident beam. Weights of each beam are found in the text. The beams are incident on a gold particle with ka=5.

One sees that while the lineshapes of the m=1 and m=2 peaks are hardly changed, substantially changes in the m=3 appear. Interestingly, the lineshape of the m=3 peak shows an asymmetry indicative of a Fano process. The size of this asymmetry to the higher frequency side of the peak is largest in the vortex #2 case and shifts as a function of the weight distributions the three OAM state populations. Also, in this spectral region the baseline of the entire spectrum becomes larger, passing values of 100 in some places.

Similarly to FIG. 7.6, FIG. 7.7 shows the FS spectra for the same three fractional vortex beams. However, significantly different features and variations are observed in the case of FS relative to RBS.

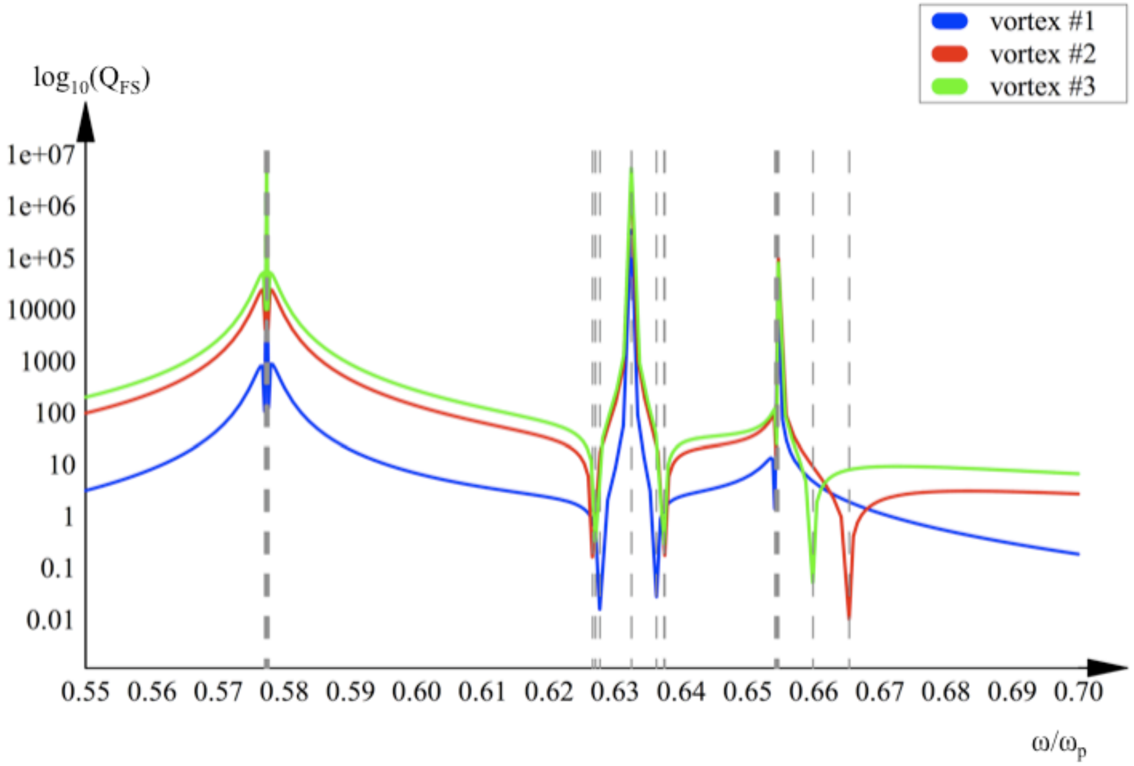

FIG. 7.7 Forward Scattering of three different broadband fractional vortex beams that share population in the same OAM states, but differ in the weight of those states in the incident beam. Weights of each beam are found in the text. The beams are incident on a gold particle.

While the m=2 peak in the RBS spectra is hardly affected by changes in the weighting of three contributions to these fractional vortex beams, the m=2 peak of the FS spectra show some changes. As the contribution from the l=1 OAM state increases in the incident beam, the minima flanking each side of the peak shift away in a symmetric fashion. However, neither the m=1 or m=2 peaks show much asymmetry.

The m=3 peak shows an asymmetric lineshape again, although the Fano component is 90 degrees out of phase with respect to that of the RBS spectra. This is a characteristic feature of the Fano effect in RBS and FS coherent scattering from nano-spheres.[5] Comparing eqns. (7.15) and (7.16), one finds that RBS is a coherent difference between angular momentum states while FS is a coherent sum of these same states. The difference in adding and subtracting the contributions produces the phase difference in the asymmetry coming from the interference of the terms.

The lack of substantial changes in the lineshapes of the m=1 and m=2 peaks in both forms of coherent scattering as a function of the weighting function on the OAM is also an indication of a Fano process taking place.[15] Gallinet and Martin propose that the Fano lineshape present in extinction, scattering and absorption spectra of plasmonic systems arises from the interference of dark and bright electromagnetic states in these structures. The spectrum of the bright state becomes modulated by the presence and activation of a dark state that is not resonant at the same frequency.

In the case of the angular momentum states of the nano-sphere, only the m=3 peak shows substantial changes in its lineshape in coherent scattering. This implies that the m=1 and m=2 states of the scattered field act as ‘dark’ states when the resonance condition of the m=3 peak is met. However, identification of the m=1 and m=2 states as ‘dark’ is counter-intuitive given the broadband nature of the incident field. Coherent excitation of the three peaks assumes the spectrum of the incident field broad enough to cover the entire spectral region in FIGs. 7.3 through 7.6.

Other researchers propose that fields scattered from differing multipole states produce Fano effects in the limit that the non-radiative damping of the material is small.[21, 22, 24] However, this treatment has made no such assumption. This treatment accounts for damping from both radiative and non-radiative relaxation.

The changes in coherent scattering spectra provide researchers the ability to tune attribute surface plasmon spectra to a specific application where needed. This tunability will aid in using plasmonic nano-structures for photonic applications ranging from optical communication to molecular sensing and characterization.

Conclusions

In this chapter, the analytical forms for the scattered EM fields from an arbitrarily sized metallic particle due an incident RHP p=0, l=1 LG beam were derived. In the small particle limit, the incident angular momentum density is transferred to the scattered and internal fields. For the incident LG beam, the angular dependence of the scattered power per unit solid angle goes to zero in both the forward and backward directions. This is useful for optical techniques that necessitate the use of circularly polarized light, but suffer from poor signal to noise ratios due to background scattering. This is true of certain forms of surface-enhanced Raman optical activity spectroscopy.[3]

Two distinct physical mechanisms account for a vanishingly small scattered intensity in the limit that the particle is much smaller than the incident wavelength. First, the strict conservation of the incident angular momentum density excites higher order moments of the scattering center whose contribution to the charge density of the particle are very small in this size limit. This small contribution dramatically limits the scattering from these higher order moments.

Second, mode-matching between the transverse profile of the incident LG and radial profile of higher order volume modes of the particle selectively excite higher order states of the scattered field. However, since these higher order volume modes necessitate contributions from higher order moment of the charge density of the particle, their excitation is very small in the small particle limit. The field profile matches volume modes that do not exist in particles in this size limit. The inability of the dipole moment of the particle to interact with the incident beam due to conservation of angular momentum and mode-matching considerations provides a method to induce transparency in matter via these physical mechanisms.

This chapter also shows that the orbital angular momentum of the incident LG results in the excitation of higher order volume modes in metallic spheres. These higher order volume modes confine more of the internal electric field amplitude to regions closer to the metal-dielectric interface than volume modes excited by plane waves. The surface confinement of these modes is a direct consequence of the conservation of angular momentum. This confinement may further enhance the signals produced in surface-enhanced molecular vibrational spectroscopies allowing more precise and thorough characterization and assignment of low concentration molecular assays.

Also the scattering spectra of the surface plasmon modes show changes in the surface plasmon response of metallic nano-spheres due to the OAM of light. The scattering fractional vortex beams possessing non-integer OAM densities from plasmonic nano-sphere highlight how to manipulate these changes. The non-integer OAM of these fractional vortex beams means that several angular momentum states can contribute as the scattered fields as different lowest orders.

By using coherent electromagnetic scattering, the otherwise insignificant contribution of higher order angular momentum states is enhanced through interference effects. Tailoring the weights of different angular momentum states in the scattered field also tailors the scattering spectra. Changes in the weighting of different OAM states in the incident fractional vortex beam changes the positions and magnitude of spectral minima around the surface plasmon resonant frequencies as well as the overall scattering baseline of the spectrum. While the predictions derived here used a spherical geometry, these results will impact technologies that use plasmonic nano-structures whose localized surface modes possess a well-defined angular momentum density.[25-27]

References

1. J. D. Jackson, *Classical electrodynamics*. (Wiley, New York, 1999).
2. C. F. Bohren and D. R. Huffman, *Absorption and scattering of light by small particles*. (Wiley, New York, 1983).
3. S. Abdali and E. W. Blanch, Chemical Society Reviews **37** (5), 980-992 (2008).
4. M. L. Brongersma, J. W. Hartman and H. A. Atwater, Physical Review B **62** (24), 16356-16359 (2000).
5. B. Luk'yanchuk, N. I. Zheludev, S. A. Maier, N. J. Halas, P. Nordlander, H. Giessen and C. T. Chong, Nature Materials **9** (9), 707-715 (2010).
6. S. A. Maier, M. L. Brongersma, P. G. Kik, S. Meltzer, A. A. G. Requicha and H. A. Atwater, Advanced Materials **13** (19), 1501 (2001).
7. S. A. Maier, P. G. Kik, H. A. Atwater, S. Meltzer, E. Harel, B. E. Koel and A. A. G. Requicha, Nature Materials **2** (4), 229-232 (2003).

8. M. E. Stewart, C. R. Anderton, L. B. Thompson, J. Maria, S. K. Gray, J. A. Rogers and R. G. Nuzzo, Chemical Reviews **108** (2), 494-521 (2008).
9. C. H. Wu, A. B. Khanikaev, R. Adato, N. Arju, A. A. Yanik, H. Altug and G. Shvets, Nature Materials **11** (1), 69-75 (2012).
10. M. Born and E. Wolf, *Principles of optics: electromagnetic theory of propagation, interference, and diffraction of light*. (Pergamon Press, 1959).
11. G. Valeria, V. Giovanni, F. Enrico, V. Michel, C. Dan and P. Dmitri, New Journal of Physics **11** (1), 013046 (2009).
12. A. S. van de Nes and P. TˆrˆK, Opt. Express **15** (20), 13360-13374 (2007).
13. J. Elser and V. A. Podolskiy, Phys. Rev. Lett. **100** (6) (2008).
14. Y. Huang, C. J. Min and G. Veronis, Applied Physics Letters **99** (14) (2011).
15. B. Gallinet and O. J. F. Martin, ACS Nano **5** (11), 8999-9008 (2011).
16. V. Klimov, D. Bloch, M. Ducloy and J. R. Rios Leite, Opt. Express **17** (12), 9718-9723 (2009).
17. C. G. Durfee, A. R. Rundquist, S. Backus, C. Herne, M. M. Murnane and H. C. Kapteyn, Phys. Rev. Lett. **83** (11), 2187-2190 (1999).
18. M. Cai, O. Painter and K. J. Vahala, Phys. Rev. Lett. **85** (1), 74-77 (2000).
19. A. R. Cowan and J. F. Young, Physical Review B **65** (8) (2002).
20. J. B. Gotte, K. O'Holleran, D. Preece, F. Flossmann, S. Franke-Arnold, S. M. Barnett and M. J. Padgett, Optics Express **16** (2), 993-1006 (2008).
21. B. S. Luk'yanchuk, M. I. Tribelsky, V. Ternovsky, Z. B. Wang, M. H. Hong, L. P. Shi and T. C. Chong, Journal of Optics A: Pure and Applied Optics **9** (9), S294 (2007).
22. M. I. Tribelsky and B. S. Luk'yanchuk, Phys. Rev. Lett. **97** (26), 263902 (2006).
23. M. A. Ordal, R. J. Bell, J. R. W. Alexander, L. L. Long and M. R. Querry, Appl. Opt. **24** (24), 4493-4499 (1985).
24. M. I. Tribelsky, S. Flach, A. E. Miroshnichenko, A. V. Gorbach and Y. S. Kivshar, Phys. Rev. Lett. **100** (4) (2008).
25. S. Y. Lee, I. M. Lee, J. Park, C. Y. Hwang and B. Lee, Appl. Optics **50** (31), G104-G112 (2011).
26. A. Drezet, C. Genet and T. W. Ebbesen, Phys. Rev. Lett. **101** (4) (2008).
27. S. Carretero-Palacios, O. Mahboub, F. J. Garcia-Vidal, L. Martin-Moreno, S. G. Rodrigo, C. Genet and T. W. Ebbesen, Optics Express **19** (11), 10429-10442 (2011).

Chapter 8:
Conclusions and Future Work

Introduction

This dissertation examines research that falls into three categories: 1) theoretical extension and experimental tests of the Laguerre-Gauss (LG)-mediated vibronic coupling model in resonantly enhanced inelastic light scattering from molecules, 2) experimental investigations of the temperature-dependent excited state dynamics and reactivity of iron(III) tetraphenylporphyrin chloride and 3) theoretical development of classical electromagnetic scattering of beams carrying OAM. In each of these research contexts, I reach important conclusions filling gaps in the literature as well as forming new questions for future work. Below, I present these conclusions and the future work they inform as distinct sections tied to the categories delineated above.

Resonance Raman Scattering of LG from Molecules

There are several important conclusions I reach from the theoretical development and experimental tests of the interaction of LG beams with molecules based on the interaction Hamiltonian of the Alexandrescu et al.[1] First, this interaction Hamiltonian extends to large polyatomic molecules. Their physical model depends on the ability to write the position of any atom in a molecule as a normal coordinate. This is straightforward in the case of the H_2^+ ion since this molecule only has one normal coordinate. However, in the case of large polyatomic molecules, there are many normal coordinates. In that case, the position of any particular atom is written as a linear combination of normal coordinates. The amended interaction Hamiltonian now contains linear combinations of normal coordinates embedded in vibronic transitions matrix elements rather than a quantum of a single normal coordinate.

Second, the coupling of the radial variation of the LG beam to the quantized vibrations of the molecule amends the selection rules for vibronic transitions. Changes in vibronic selection rules in this manner mirror the breakdown of the adiabatic approximation and vibronic coupling.[2] In light-molecule interactions vibronic coupling loosens restrictions on allowed transitions by lowering the symmetry of the molecule.[3] Physically, this corresponds to the simultaneous excitation of both nuclear motion and an electronic transition, invalidating the Condon approximation. In this 'light', the coupling of the radial variation of the LG to the quantized vibrations of the molecule represents an EM-mediated vibronic coupling, also invalidating the Condon approximation.

Third, based on the functional form of the multipolar interaction Hamiltonian, this EM-mediated vibronic occurs throughout the intensity profile of the LG beam. Since the radial variation of the beam is not relegated to the center of the beam in the same way as the beam's vortex, the effect of EM-mediated vibronic coupling in molecular spectroscopy is much larger. A larger effect is easier to detect in an experimental test.

Fourth, when this extended interaction Hamiltonian is applied to the resonantly enhanced inelastic light scattering from a molecule's totally symmetric vibrations, two interesting effects arise. On one hand, LG beams amend population reaching overtone excitations in both small, diatomic and large, polyatomic molecules. For large molecules whose excited electronic state is minimally displaced with respect to the ground state, this mechanism introduces new peaks to the 'baseline' spectrum.

One the other hand, additional scattering pathways introduced by the LG beam interfere with already existing pathways present in the scattering process. This interference modulates the intensity of resonance Raman peaks present in the 'baseline' spectrum and depends of the laser spot size, the detuning of the laser frequency from the electronic resonance and the frequency of the vibration of interest.

Fifth, experimental tests using spontaneous resonance Raman scattering spectroscopy show no indication of the effects predicted from the EM-mediated vibronic coupling model. Condensed phase samples of diatomic iodine (I_2) and iron(III) tetraphenylporphyrin chloride [$Fe^{(III)}$TPPCl] show indistinguishable spectra when excited with TEM_{00} and LG beams. Assuming the validity the derivation of the EM-mediate vibronic coupling model, these results provide a ceiling on the magnitude of the predicted effects based on the signal-to-ratio (SNR) of the measurement. For the measurements undertaken, this ceiling is a factor of 1/10000 to 1/1000 times smaller than the ‘baseline’ spectrum.

These conclusions inform specific avenues of future work. Most importantly, the spot of the incident beam dominates the interference effects predicted in resonance Raman scattering in the visible region of the EM spectrum. Since the radial profile of the incident LG beam is defined in the paraxial approximation as a solution to the paraxial Helmholtz equation, this approximation restricts the smallest focus possible to several hundred nanometers. In these cases the ratio of the characteristic length scale of the material system of interest to the spot size still approaches values smaller than 1/10000. With ratios that small, visible light-molecule interactions may not physically be able to display effects associated with the EM-mediated vibronic coupling model. However, at shorter wavelengths restriction becomes less severe.

Research into the role of OAM and vortex beams in x-ray-molecule interactions shows new behavior providing new information on the structure of molecular solids.[4] van Veenedaal and McNulty extend the same interaction Hamiltonian proposed by Alexandrescu et al. to show the radial variation of an x-ray LG beam couples to the higher order multipole moments of a centrally ligated metal atom. These higher order moments amend the calculated magnetic orbital dichroism. However, these authors explicitly ignore the effects associated with the interference between these newly excited higher order moments and the dipole moment of the atom. In direct connection to the interference effects I predict in this dissertation, the strongly allowed dipole transitions in a metal atom enhances the LG-mediated interference effects from the introduction of higher order moments.

In addition, many first order x-ray-matter interactions are best understood as scattering processes.[5, 6] After the excitation of core electrons in an atom, either other core or valence electrons relax into the core vacancy. In many instances, this relaxation occurs in conjunction with the ejection of an Auger electron. For large, complex metal atoms in materials central in many important technologies many Auger relaxation pathways interfere with one another to produce the observed physics. By modulating the x-ray absorption process with OAM one introduces new pathways into this relaxation, opening the possibility for the coherent control of x-ray-matter processes.

Fe$^{(III)}$TPPCl Excited State Dynamics and Reactivity

Temperature dependent ultrafast transient and resonant Raman spectroscopies provide important conclusions concerning the excited state dynamics and reactivity of Fe$^{(III)}$TPPCl. First, the excited state dynamics of Fe$^{(III)}$TPPCl starkly contrast with those of iron-centered heme proteins.[7-10] After depopulating the initially excited state in several hundred fs, the electronic population of the excited Fe$^{(III)}$TPPCl molecule relaxes through a sequence of electronic states.

This sequential electronic relaxation is independent of the excitation wavelength. Excitation on both the Soret (400 nm) and first vibronic overtone of the Q (520 nm) resonances lead to the same sequential relaxation. The lifetime of the longest-lived of these states is solvent dependent and ranges from 14 ps to 16 ps as a function of the polarity of the solvent. At 88 K, the lifetime of this state is lengthened to over 1 ns, indicating that the decay of population from this state is dominated by an electronic relaxation.

Second, at sub-100 K temperatures and in the presence of toluene, Fe$^{(III)}$TPPCl participates in photochemistry not observed at room temperature. Power dependent resonance Raman scattering diagnoses this photochemistry when the sample is illuminated on the Soret resonance of the ground state at 413 nm. When the sample is dissolved in CH_2Cl_2 or illuminated at either 488 nm or 514 nm no evidence of photochemistry is observed. Low temperature transient absorption measurements excited with 400 nm also show evidence of a long-lived (~ 1 s) state whose difference spectrum differs from those observed in the room temperature transient dynamics.

A model qualitatively accounts for the relative populations of the ground and product state present in the experiment. This model proposes formation three photochemical products from absorption of 413 nm light by a long-lived (~1 ns) excited state of Fe$^{(III)}$TPPCl. Observation of nonlinear laser intensity dependent solvent scattering indicates the formation of excited state complex between toluene and photo-excited Fe$^{(III)}$TPP molecules. The low temperature TA measurements confirm the existence and floor values of the lifetime of this state.

Since changes in the resonance Raman scattering of FeTPP are well characterized, we assign the identity of the product states.[11-13] One product is likely a five-coordinated Fe$^{(III)}$TPP bound to a toluene molecule in the axial position to the Fe atom. The other products display structure-sensitive vibrations consistent with assignment as two forms of six-coordinate Fe$^{(III)}$TPP. One of these products contains a central Fe atom in its low-spin state populated via a spin-crossover transition from the initially excited high-spin state due to distortions of the porphyrin ring caused by toluene ligation.[14, 15]

The conclusions from these studies inform future studies of the excited state dynamics and suitability of photochemistry of metalloporphyrins in two distinct technologies. First, while Fe-centered porphyrins do not naturally form light harvesting structures, other metalloporphyrins do. In particular, Mg-centered porphyrin-like structures form as a center in the light-harvesting units of many plant systems. As in the case of Fe$^{(III)}$TPPCl, only a few studies of the ultrafast dynamics of simpler synthetic forms of natural analogs of these metalloporphyrins exist.[16] Showing that the dynamics of Fe$^{(III)}$TPPCl are poorly modeled by those of biological hemes with which it shares structural similarities, it may be the case that similar studies of the ultrafast transient dynamics of other metalloporphyrins find similar contrasts with other biologically produced systems. These will provide insight into the suitability of synthetic metalloporphyrins in light harvesting and opto-electrochemical applications.

Second, the photochemistry of Fe$^{(III)}$TPPCl shows evidence of a coupling of its optically induced electronic transitions and the magnetic states of the central Fe atom. This is the first demonstration of coupling between the optical and magnetic properties of a Fe-centered porphyrin. From this result, one can imagine a pathway to functional magnetic materials based on photo-driven bond breaking and formation in the solid state. A high symmetry Fe-porphyrin chromophore is excited at a specific frequency to a state in which its axial ligand is either directly or indirectly dissociated and then captured by the surrounding environment. The resulting Fe-porphyrin radical or ion recruits a large molecule axial ligand that binds in a single, dominant conformation to the Fe atom. This single conformation distorts the symmetry of the porphyrin along the appropriate normal coordinates and to the appropriate extent to induce a spin crossover transition of the vast majority of the photoexcited Fe-porphyrin molecules. Excitation at different frequency releases the original ligand from the surroundings allowing it to recombine with the Fe-porphyrin and inducing a spin crossover back to the original spin state.

This technology will necessitate further study of the production of the low-spin state. This is especially true of the product formed in the ultrafast TA measurement. If coherent two-photon absorption accesses a state that dissociates the axial ligand and recruits a large molecular ligand to form the low-spin state, then one does not need to engineer the lifetime of the participating excited state that absorb the second photon. Such a mechanism would greatly aid in utilizing $Fe^{(II)}$TPP as the spin crossover structure. The crossover from high-spin to low-spin in $Fe^{(II)}$ could transition a material from magnetic to non-magnetic via photoexcitation, as has been demonstrated with other inorganic molecular materials.[17]

Classical EM Scattering of LG Beams

The theoretical development of the classical scattering of LG beams from spherical particles provides several important conclusions concerning their use in modulating the behavior of metallic nano-structures. This modulation may be useful in the context of plasmonic response and the development of novel metamaterials. These conclusions help inform future work on manipulating angular momentum density of collective modes of plasmonic crystals and metamaterials.

First, for a particle placed at the center of a circularly polarized LG beam, the incident angular momentum density is conserved in both the scattered fields and the fields internal to the particle. In the case of a p=0, l=1 LG beam, this conservation is evident from the lowest order term in the expansion of the scattered and internal fields over the vector spherical harmonics. In the small particle limit, this lowest order term corresponds to the electric quadrapole.

Second, in the small particle limit scattered field is vanishingly small. The minimal intensity of scattered field occurs due to the excitation of higher order multipole moments via two, distinct physical mechanisms. On the one hand, in the limit that the particle is much smaller than the wavelength of the incident light the dipole moment dominates its EM response and higher order moments are strongly attenuated. However, since the angular momentum of the incident beam is conserved in the scattered field, only moments higher than the dipole are excited by the incident LG beam. Therefore, the LG beam weakly interacts with the dipole-dominated particle and scatters very little of the incident power from it.

On the other, the transverse profile of the incident LG beam matches the radial variation of the higher order volume modes of the particle excited by the incident angular momentum density. This mode matching strongly couples the incident beam with these higher order volume modes. However, since the particle is small with respect to the wavelength of the incident beam, its dipole moment dominates its response. Given the coherent nature of exciting the internal and scattered fields, this mode-matching reduces the intensity of the scattered fields even further. These two complimentary physical mechanism lead to an angular momentum-induced transparency of the particle in the presence of an incident LG beam.

Third, the conservation of the angular momentum in the scattering process opens an avenue to the control of the frequency-dependent scattering spectra of plasmonic nano-spheres. Through the use of fractional vortex beams, which possess non-integer values of OAM, one can modulate the spectral content of incoherent plasmonic scattering. This modulation occurs due to the presence and weight of several lowest order multipole contributions to the scattered field. The conservation of angular momentum also allows selectively tailoring of attributes of coherent plasmonic scattering. This tailoring occurs due to the interference between strongly attenuated higher order multipole moments and the dominant dipole moment. Changes in the interference between these angular momentum states produces changes in the Fano lineshapes of peaks in the coherent scattering spectrum as well as changes to the magnitude and shape of the scattering baseline.

Each of these conclusions informs a different avenue of future work in classical EM scattering. In the case of angular momentum-induced transparency, proving changes in the scattering of particles small with respect to an optical wavelength is due to the conservation of angular momentum may be difficult. Since the light intensity at the center of a LG beam falls to zero and OAM is not defined outside of the paraxial approximation, another plasmonic system may be necessary to observe angular momentum induced transparency. A crystal constructed from a plasmonic material could provide such a system. Plasmonic crystals with controllable angular momentum densities have been designed, constructed and characterized.[18-20]

The spectral and coherent control of frequency-dependent plasmonic scattering spectra may prove useful in chemical sensing, optical information technology as well as nonlinear optics.[21-25] For chemical sensing, one could use fractional vortex beams to tailor these scattering spectra to optimize the signals in a surface-enhanced vibrational spectroscopy. In optical information technology control of frequency-dependent spectra allows for wavelength multiplexing and de-multiplexing of information embedded in the light fields as a function of the weighting distribution on the fractional vortex beam. For nonlinear optics, research shows that harmonic generation from spherical metallic particles is connected to the angular momentum excited in the hyper-scattering process. By controlling the angular momentum states participating in the scattering process, one could control the efficiency and number of harmonics generated from plasmonic structures with modes possessing well-defined angular momentum densities. This control is especially useful in solar energy technologies where near-infrared light needs to frequency-doubled efficiently to reach energies above the band gap of semiconductors used in solar photovoltaics.

References

1. A. Alexandrescu, D. Cojoc and E. Di Fabrizio, Phys. Rev. Lett. **96** (24) (2006).
2. G. Fischer, *Vibronic coupling: the interaction between the electronic and nuclear motions*. (Academic Press, London ; Orlando, Fla., 1984).
3. D. C. Harris and M. D. Bertolucci, *Symmetry and spectroscopy: an introduction to vibrational and electronic spectroscopy*. (Oxford University Press, New York, 1977).

4. M. van Veenendaal and I. McNulty, Phys. Rev. Lett. **98** (15) (2007).
5. L. Fonda, J. Phys.-Condes. Matter **4** (43), 8269-8302 (1992).
6. P. Auger, Journal De Physique Et Le Radium **6**, 205-U212 (1925).
7. J. C. Postlewaite, J. B. Miers and D. D. Dlott, J. Am. Chem. Soc. **111** (4), 1248-1255 (1989).
8. A. Yabushita and T. Kobayashi, J. Phys. Chem. B **114** (35), 11654-11658 (2010).
9. W. Wang, X. Ye, A. A. Demidov, F. Rosca, T. Sjodin, W. X. Cao, M. Sheeran and P. M. Champion, J. Phys. Chem. B **104** (46), 10789-10801 (2000).
10. M. Negrerie, S. Cianetti, M. H. Vos, J. L. Martin and S. G. Kruglik, J. Phys. Chem. B **110** (25), 12766-12781 (2006).
11. H. Oshio, T. Ama, T. Watanabe, J. Kincaid and K. Nakamoto, Spectrochimica Acta Part A: Molecular Spectroscopy **40** (9), 863-870 (1984).
12. G. Chottard, P. Battioni, J. P. Battioni, M. Lange and D. Mansuy, Inorg. Chem. **20** (6), 1718-1722 (1981).
13. J. M. Burke, J. R. Kincaid, S. Peters, R. R. Gagne, J. P. Collman and T. G. Spiro, J. Am. Chem. Soc. **100** (19), 6083-6088 (1978).
14. N. Sasaki and T. Kambara, J. Chem. Phys. **74** (6), 3472-3481 (1981).
15. G. D'Avino, A. Painelli and K. Boukheddaden, Phys. Rev. B **84** (10) (2011).
16. B. Dietzek, R. Maksimenka, W. Kiefer, G. Hermann, J. Popp and M. Schmitt, Chemical Physics Letters **415** (1-3), 94-99 (2005).
17. O. Sato, T. Iyoda, A. Fujishima and K. Hashimoto, Science **272** (5262), 704-705 (1996).
18. A. Drezet, C. Genet and T. W. Ebbesen, Phys. Rev. Lett. **101** (4) (2008).
19. S. Carretero-Palacios, O. Mahboub, F. J. Garcia-Vidal, L. Martin-Moreno, S. G. Rodrigo, C. Genet and T. W. Ebbesen, Opt. Express **19** (11), 10429-10442 (2011).
20. S. Y. Lee, I. M. Lee, J. Park, C. Y. Hwang and B. Lee, Appl. Optics **50** (31), G104-G112 (2011).
21. J. P. Dewitz, W. Hubner and K. H. Bennemann, Zeitschrift Fur Physik D-Atoms Molecules and Clusters **37** (1), 75-84 (1996).
22. M. E. Stewart, C. R. Anderton, L. B. Thompson, J. Maria, S. K. Gray, J. A. Rogers and R. G. Nuzzo, Chemical Reviews **108** (2), 494-521 (2008).
23. S. A. Maier, M. L. Brongersma, P. G. Kik, S. Meltzer, A. A. G. Requicha and H. A. Atwater, Advanced Materials **13** (19), 1501-+ (2001).
24. B. Luk'yanchuk, N. I. Zheludev, S. A. Maier, N. J. Halas, P. Nordlander, H. Giessen and C. T. Chong, Nat. Mater. **9** (9), 707-715 (2010).
25. S. Abdali, Journal of Raman Spectroscopy **37** (12), 1341-1345 (2006).